Assessment of loading rate effects on elastic-plastic shell buckling capacity of monopiles subjected to bending moments

E.P.G. Teeuwen

15/09/2023

Delft University of Technology

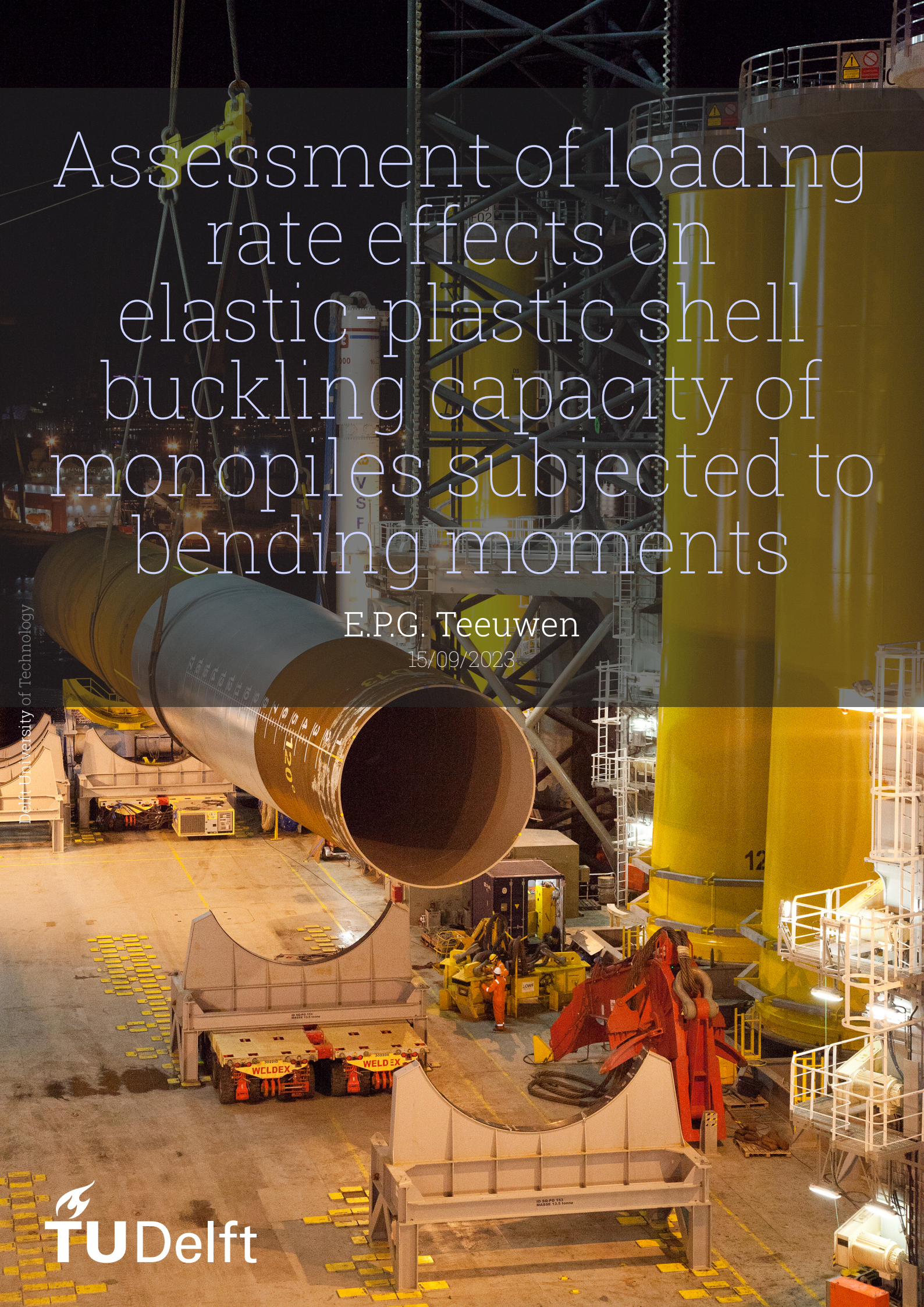

TU Delft

Assessment of loading rate effects on elastic-plastic shell buckling capacity of monopiles subjected to bending moments

by

E.P.G. Teeuwen

to obtain the degree of Master of Science

at the Delft University of Technology,

to be defended publicly on 22 September at TU Delft.

Student number:	4291913	
Project duration:	November 22, 2021 – September 22, 2023	
Thesis committee:	Dr. C.L. Walters,	TU Delft, supervisor
	Dr. A. Napoleone,	TU Delft,
	Wei Jun Wong,	TU Delft.

TU Delft

Abstract

It is becoming increasingly clear that the effects of climate change should be decreased or even mitigated. Green alternative sources of energy are being explored, and wind energy emerges as an important option that can be exploited on a large scale. Wind turbines are placed more and more often offshore due to larger and more stable wind resources. The most common foundations for these turbines are monopiles. The future outlook for these turbines and their foundations is that they will become bigger. An important design characteristic of monopiles is the natural frequency of the pile. In order to keep dynamic effects to a minimum, excitation frequencies should not coincide with the natural frequency. The primary source of excitation of monopiles are bending moments. Therefore, this thesis will take a closer look at the dynamic bending capability of monopiles.

There is a lack of knowledge on dynamic effects of bending moments on steel cylindrical shells (monopiles). While the dynamic axial buckling capacity of cylindrical shells has been researched extensively, there is little known on the dynamic bending buckling capacity of such shells. This thesis investigates the influence of loading rate on the dynamic buckling capacity of monopiles subjected to bending moments. For this, a finite element model is constructed which is validated by analytical models. Later on, the finite element model is used to conduct a parametric study to investigate the effect of loading rate on buckling capacity.

The scope of this study excludes factors such as soil dynamics, fluid structure interactions, residual stresses, and lateral forces. The focus is solely on the cylindrical shell of monopiles, excluding secondary steel from consideration. Initial geometric imperfections are considered as local perturbations necessary to initiate buckling, while other factors that may affect lateral forces or overall structural capacity are excluded.

This study will show that different parameters play part in the dynamic bending buckling behavior of cylindrical shells. The natural frequency of the cylinder, as well as the non-dimensional length together with the yield stress of the material play an important role in the dynamic buckling capacity. This research concludes that cylindrical shells with higher natural periods are more influenced by dynamic bending moments than cylinders with shorter periods. Next, shorter, stocky cylinders exhibit higher dynamic buckling capacities than slender cylinders. Also, imperfections are found to decrease the buckling capacity of cylindrical shells, but this effect diminishes for increasing loading rates.

Keywords: Offshore wind energy; Cylindrical shells; Dynamic buckling; Loading rate; Imperfections; FEM;

Preface

This thesis explores the fascinating topic of dynamic buckling in cylindrical shell structures, with a specific focus on monopiles used as foundations for offshore wind turbines. It is driven by the urgent need to address climate change and transition to sustainable energy sources. As wind turbines continue to increase in size and capacity, understanding the dynamic behaviour of their foundations becomes crucial.

I express my gratitude to my supervisor Carey Walters and PhD candidate Wei Jun Wong who have guided and encouraged me throughout this research. Their expertise has been invaluable in shaping this thesis. I also extend my appreciation to roommates, friends, and family for their unwavering support.

May this thesis encourage professionals in engineering to contribute to the design and analysis of offshore wind turbine foundations. Together, let us advance sustainable energy solutions for a greener future.

E.P.G. Teeuwen
The Hague, September 2023

Contents

List of Figures

List of Tables

1 Introduction

1.1. Research Background

In 1990, the United Nations' Intergovernmental Panel on Climate Change (IPCC), one of the leading scientific authorities on climate change, published its first parts of an assessment report on climate change (Intergovernmental Panel on Climate Change [IPCC], 1992). Since then, there have been treaties, gatherings and agreements such as the Earth summit in 1992, which discussed the first assessment of the IPCC, the Paris agreement in 2015 (COP21), and the most recent one: COP26 in 2021 (United Nations [UN], 1992) (UN, 2015) (UN, 2021). All of the above concluded that the effects of climate change should be decreased or mitigated. For example, the European Union stated in the 2030 Climate Target Plan their ambition to reduce greenhouse gas emissions to at least 55% below 1990 levels by 2030, and to be climate neutral by 2050 (European Commission, 2020). In order to do so, the energy industry must undergo a transition from fossil fuels towards green, sustainable solutions. Over the last decades, wind energy emerged as one of the leading technologies for large-scale sustainable power production (International Energy Agency [IEA], 2021). Both onshore and offshore wind solutions are market ready and are being scaled up. Since higher, more stable wind resources, more space, and less turbine size restrictions exist offshore, this proves to be an efficient way of producing green energy.

Currently, monopiles are used as foundation in offshore wind for 80% of the turbines (International Renewable Energy Agency [IRENA], 2021). Monopiles are long, hollow cylinders, embedded in the seabed. These shell structures are made of steel and provide support for the tower of the wind turbine. The primary loads on a monopile consist of environmental loads, such as wind and waves. The monopile must be able to resist these forces. Especially the thrust force from the rotor due to wind loads exerts a large bending moment on the structure. The first side-side and the first fore-aft mode shapes result in large bending moments in the monopile at the mud line. Figure 1.1a shows the blade-passing frequencies for large three-bladed turbines and the wind spectrum. In order to avoid resonance in the support structure, these frequencies should be avoided. Therefore, monopiles are most often constructed with natural frequencies in the soft-stiff region. This is about 0.25 Hz for large wind turbines. The mode shapes of a monopile including the tower are shown in Figure 1.1b.

At the moment, the majority of the offshore installed turbines have a capacity of around 7 MW. The dimensions of the monopiles that are used to support these turbines are around 100 m in length, a bottom diameter of 8 m and thicknesses of up to 100 mm. These piles often weigh more than 1500 tons (Mulazzani, 2021). Turbine manufacturers are already bringing 14 MW turbines to the market, which results in the need for larger foundations. The expectation is that monopiles necessary to support these larger turbines will have bottom diameters of up to 14 m with thicknesses of around 140 mm and a total weight of 3000 tons (Mulazzani, 2021).

In conclusion, the size of wind turbines will increase over the coming years. This is also corroborated by the International Renewable Energy Agency (2019). Although wind farms are moving further

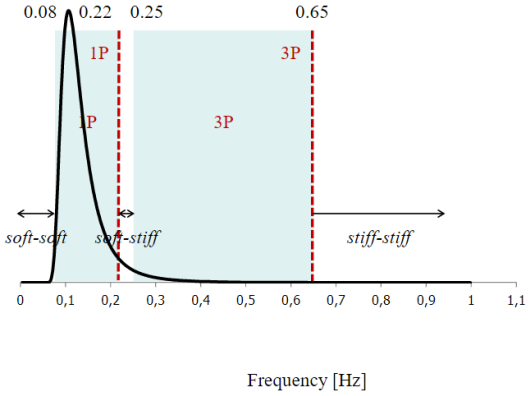

(a) Wind spectrum and blade frequency regions (Lourens, 2021)

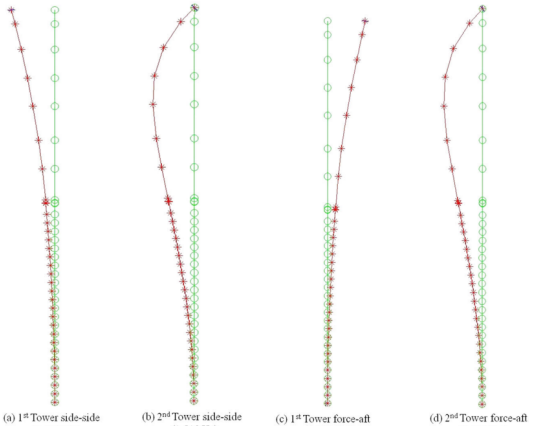

(b) 1st and 2nd mode shapes of a 5 MW turbine, side-side movement on the left and fore-aft on the right (Kim et al., 2015)

Figure 1.1: Frequency regions and mode shapes of wind turbines

offshore to deeper waters, monopiles are predicted to remain cost-competitive even in water depths over 35 meters (IRENA, 2016). These developments will result in larger stresses to be countered by the foundations. Although current norms and standards describe extensive measures to ensure safety for structures, including monopiles, one of the topics that is not described is that of dynamic buckling.

1.2. Thesis objective

A lot of research has been done into buckling of cylindrical shells. Buckling of axially compressed shells is studied sufficiently to estimate static and dynamic monopile buckling loads. Many qualitative or quantitative studies are written about imperfections, geometric ratios, material properties, and sections with varying thickness or cone angles. However, knowledge on cylindrical shells loaded in dynamic bending is not sufficient to make such estimates. As the largest forces on wind turbines are the bending moments, the loading rates may be highest for this type of load. Therefore, this thesis will focus on assessing the influence of loading rate on dynamic buckling of cylindrical shells subject to bending moments.

1.2.1. Research questions

The objective of this thesis can be summarised by the following main research question.

"What is the influence of loading rate on the dynamic buckling capacity of monopiles subjected to bending moments?"

The main research question will be divided into the following subquestions for a simplified approach.

1. *Which parameters influence the dynamic buckling capacity of cylindrical shells?*
   In order to be able to see the influence of loading rate on buckling capacity of cylindrical shells, it should first be known what to look for and where to look for it. The parameters that influence the dynamic buckling capacity, next to the loading rate, can then be used to evaluate the effect of differing loading rate.

2. *What is the dynamic buckling capacity of a cylindrical shell subjected to bending, resembling the characteristics of a monopile?*
   Separate analyses per characteristic need to be done in order to see what the influence of loading rate is on each individual characteristic.

1.2.2. Further elaboration of the scope

As discussed in section 2.8, large parts of monopiles are either submerged in the sea or even below the mudline. This severely complicates any buckling analysis as soil mechanics and Fluid Structure

Interaction (FSI) should be taken into account. Soil mechanics and FSI are both extensive fields of study, and it is therefore decided that these are excluded from the scope of this thesis in order to confine the workload.

This research will focus on dynamic buckling of monopiles and will solely consider initial geometric imperfections as local perturbations necessary to initiate buckling. Residual (welding) stresses and lateral forces will not be considered. The largest lateral forces on a monopile are likely to be caused by hydrodynamic pressure variations or soil conditions. Both fields have already been excluded from the scope of this thesis due to a limited available workload.

At last, only the cylindrical shell of a monopile will be considered. This excludes secondary steel from the scope as its extra structural capacity is expected to be negligible in comparison to the structural capacity of the primary shell.

1.3. Thesis Outline

This section gives an overview of the thesis outline per chapter. Subsequently, the content per chapter will be described briefly.

A literature review is performed and the results are discussed in **chapter 2**. This shows that dynamic bending buckling requires more research. Also, it's an overview of the research that is applied in this thesis.
Chapter 3 is about the methodology of this research. It discusses the research method and desired results.
In **chapter 4**, the description of the analytical models that are used to validate the Finite Element Model (FEM) is given. The analytical model is also used to perform a parametric study to investigate the influence of certain parameters on the dynamic buckling load. This chapter also answers the first subquestion.
The finite element models are reviewed in **chapter 5**. Assumptions and modelling choices are explained. The validation process of the model is elaborated on as well.
The results of the simulations with the FE models for each separate characteristic of a monopile will be shown and discussed in **chapter 6**. The aim of this chapter is to give an answer to the second subquestion.
A conclusion will be drawn in**chapter 7** and the research choices will be discussed. At the end, recommendations for further research will be given.

2

Literature Review

Dynamic buckling is not described by standards like DNVGL-ST-0126: Support structures for wind turbines or DNV-OS-J101: Design of Offshore Wind Turbine Structures (DNVGL, 2016) (DNV, 2013a). These standards refer to more general standards focused on shell structures; DNV-RP-C202: Buckling Strength of Shells and NEN-EN-1993-1-6: Eurocode 3 - Strength and Stability of Shell Structures. However there is nothing about dynamic buckling in these two either (DNV, 2010) (NEN, 2007). Even though these standards do not take dynamic buckling into account, the matter is extensively researched (as opposed to dynamic bending buckling). The most relevant research to this thesis will be discussed.

2.1. Global vs. local buckling

For clarity, first the difference between local and global buckling of shell structures is discussed briefly. Xu et al. distinguished between both buckling modes by describing local buckling as buckling where the cross section of the shell might deform but its axis remains straight (2009). Global buckling resembles bending of a beam where cross sections may deform in a nonuniform way (Xu et al., 2009). Local buckling occurs in a structure where the buckling stress is reached, see Equation 2.1 (Axelrad, 1985).

$$\sigma_{crs} = \frac{Eh}{R\sqrt{3(1-\nu^2)}} \tag{2.1}$$

In this equation, σ_{crs} is the critical static buckling stress, E is the Young's modulus, ν is the Poisson's ratio, h is the thickness and R is the radius of the cylindrical shell. This means that local buckling does not depend on the length of the cylinder as opposed to global buckling. There can be local deformations in the shell structure without complete loss of stability.

Evkin et al. have shown that there are (small) local perturbations required for local buckling. These perturbations can present themselves as lateral force, prescribed deflections, or as an energy barrier (residual stresses present in the structure before loaded) (Evkin et al., 2019). For monopiles, wave loads could act as lateral forces; prescribed deflections occur in the form of material or fabrication imperfections; and residual stresses may be present in the structure because different sections are welded together.

Figure 2.1 shows possible buckling paths. The normalised load parameter $\overline{N}$ is on the vertical axis of this figure, which is calculated using Equation 2.2.

$$\overline{N} = \frac{N}{N_{crs}}, \quad N_{crs} = \frac{2\pi h^2 E}{\sqrt{3(1-\nu^2)}} \tag{2.2}$$

In this equation, $\overline{N}$ is the static normalised buckling load, N is the axial force, and N_{crs} is the critical buckling force. The graphs shows that for a perfect shell, without any of the three aforementioned local perturbations, local buckling will not occur until the locad parameter is above $\overline{N}$. This is a perfect scenario and exists only theoretically. For imperfect shells, with local perturbations, buckling might occur.

For larger initial imperfections (the imperfect shell curves start with initial deflection) either general, global buckling or local buckling may develop. The difference is depicted in the graph; when general (global) buckling happens at a load of $\overline{N}^{+}$, there is no stable path anymore that the structure can follow. When local buckling occurred, there is a large increase in deformation while the load capacity of the structure decreases. However, at $\overline{N}^{-}$, the structure regains its load capacity and can, in some cases, bear more load than at the moment of the initial local buckle.

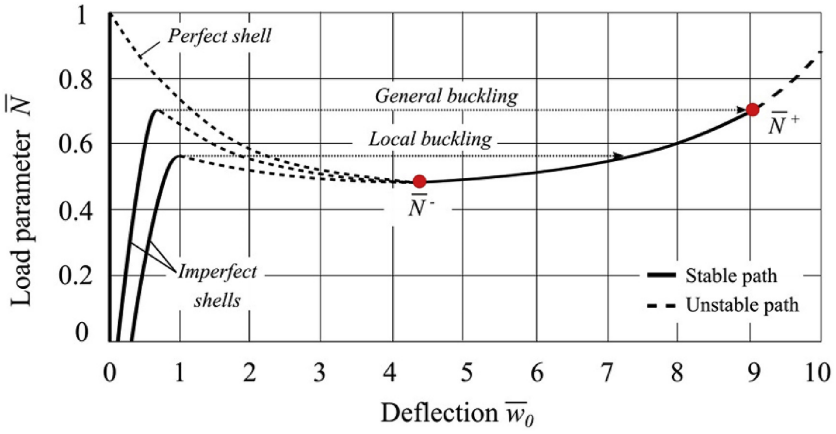

Figure 2.1: Equilibrium paths for perfect and imperfect static normalised buckling load $\overline{N}$ (Evkin et al., 2019)

Local dynamic buckling depends on a lot of different properties of the structure. These are discussed briefly in the next section.

2.2. Dynamic load

Dynamic loads in buckling have a large influence on the buckling capacity of structures. In order to make a comparison between static and dynamic buckling, the dynamic load factor (K_d) is introduced in Equation 2.3, with N_{CRD} being the critical dynamic buckling load and N_{CRS} the critical static buckling load (Sofiyev, 2005).

$$K_d = \frac{N_{CRD}}{N_{CRS}} \tag{2.3}$$

Both the shape of the load in time and the duration of the load can have an effect on the dynamic buckling capacity of structures. The influence of the duration of the load is often described using the dynamic load factor K_d, as an infinite load duration resembles static loading. In general, K_d decreases rapidly for larger load duration. Fan et al. conclude that larger loading speeds correlate to larger dynamic load capacities (Fan et al., 2016). For duration periods larger than natural periods of structures, the dynamic load factor can be below unity (Zaczynska et al., 2020). This can be explained by considering stress wave propagation in the shell. When one end of the shell is subjected to a step impact load, a longitudinal wave starts propagating with a wave speed c, see Equation 2.4.

$$c = \sqrt{\frac{E}{\rho(1-\nu^2)}} \tag{2.4}$$

The wave speed is dependent on the material properties, the Young's modulus E, the density ρ and the Poisson's ratio ν. The stress wave reflects when it reaches the other end of the cylinder. Before the wave is reflected, the axial force in the shell is N. If the load duration exceeds the natural period of the shell, the maximum axial force in the shell is 2N when reflection has occurred (Xu et al., 2005). Therefore, it is possible for the critical dynamic buckling load to be smaller than the critical static load and thus for the dynamic load factor to be lower than unity. However, it should be mentioned that both papers considered impulsive loads, which essentially have the shape of a step function (in time). Fan et al. conclude that larger loading speeds correlate to larger dynamic load capacities (Fan et al., 2016).

The load speed influences the buckling mode of cylindrical shells as well. In case of short load duration, below the natural frequency, the shell exhibits a diamond shape pattern, whereas for longer load duration the wave reflects and the cylinder resembles elephant-foot buckling (Zaczynska et al., 2020) (Zhou et al., 1991). Elephant-foot buckling presents itself as an axisymmetrical buckle at one end of the cylinder. It should be noted that longer load duration is relative to the natural period of the cylinder, which is dependent on length among other geometrical and material properties (Warburton, 1969).

2.3. Geometric ratios

The geometry of the cylinder in compression also has a major influence on the buckling capacity of the structure, both static and dynamic. According to Timoshenko and Gere, the critical static buckling stress is a function of the geometric parameters thickness h and radius R, and the material properties Young's modulus E and the Poisson's ratio ν (Timoshenko & Gere, 1961), see Equation 2.5.

$$\sigma_{crs} = \frac{h}{R} * \frac{E}{\sqrt{3(1-\nu^2)}} \tag{2.5}$$

This is corroborated by Sofiyev, in the same paper where he discusses an analytical method to find the dynamic buckling capacity (Sofiyev, 2005). Sofiyev, in accordance with Xu et al., states that the critical dynamic buckling load depends on the same parameters as the critical static load, next to the density ρ of the material and the loading rate (Xu et al., 2009). By including the density of the material, the inertia of the shell is included in the analysis.

Equation 2.1 can be used to calculate the critical buckling force and moment of a cylindrical shell. The critical axial force N_{crs} is given in Equation 2.2, the classical critical bending moment M_{crs} is given in Equation 2.6 (J. M. Rotter et al., 2014). These critical buckling equations are only valid for linear buckling, which means that they do not take material or geometrical non-linearities into account.

$$M_{crs} = \sigma_{crs} * \pi R^2 h = \frac{\pi R h^2 E}{\sqrt{3(1-\nu^2)}} \tag{2.6}$$

Sofiyev discusses an analytical method to find the axial dynamic buckling load for cylindrical shells, focused on composite materials. However, the analytical solution can be generalised for homogeneous materials. Besides composite materials, solutions are also given for stainless steel SUS304 and a titanium alloy Ti-6Al-4V. Monopiles are mostly made of engineering steels like S355, S460 and S690. In Figure 2.2, an overview the engineering stress-strain curves of these materials is given. Figure 2.2c shows resemblances to both stress-strain curves of SUS304 in Figure 2.2a and Ti-6Al-4V in Figure 2.2b.

In Figure 2.3, the relation between the critical dynamic buckling load N_{crd} and the dynamic load factor K_d, and the ratio R/h is given for stainless steel SUS304 and a titanium alloy Ti-6Al-4V. From this graph, it can be concluded that for large R/h ratios (and thus relatively thin shells) the critical dynamic load decreases, even though the dynamic load factor increases. In other words, thicker shells have higher buckling capacities, but the dynamic buckling capacity is relatively lower.

The critical buckling load depends on the ratio between certain parameters (such as the radius over thickness ratio, R/h), which can be scaled. Because of this, research into smaller structures is also applicable to larger structures. Some geometric quantities like the size of imperfections are less likely to scale in the same way as radius and thickness; therefore these are non-dimensionalised as well (Wang & Sadowski, 2020). This will be explained in more detail in section 2.5.

2.4. Material properties

Equation 2.5 shows that the critical buckling load is dependent on the material properties Young's modulus E and the Poisson's ratio ν. For S-type engineering steels, which are used in monopile design, the values of E and ν are approximated as $E = 210GPa$ and $\nu = 0.3$ (DNV, 2013b). Equation 2.5 is an equation to determine the linear buckling stress. Therefore it does not take plasticity or other non-linearities into account.

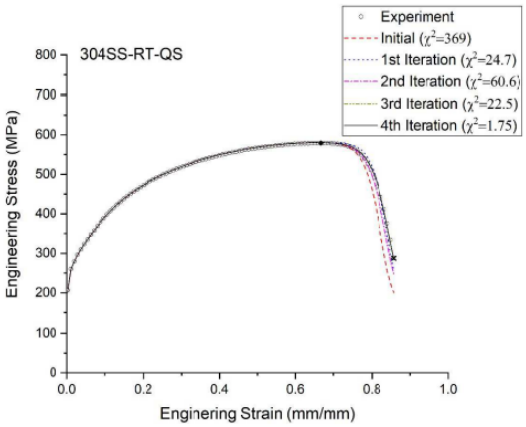

(a) Stress-strain curve of SUS304 (Kweon et al., 2020)

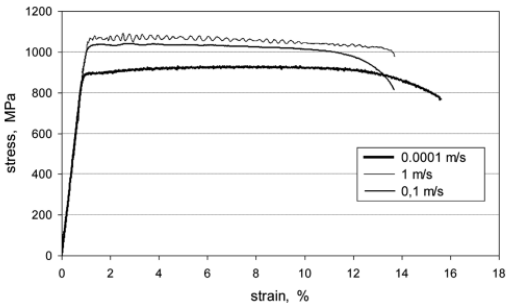

(b) Stress-strain curve of Ti-6Al-4V (Wojtaszek et al., 2013)

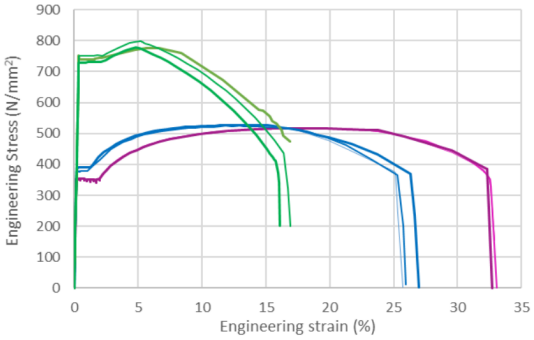

(c) Stress-strain curve of engineering steels S275, S355 and S690 (Ho et al., 2021)

Figure 2.2: Stress-strain curve comparison of materials used by Sofiyev and frequently used materials in monopiles (Sofiyev, 2005)

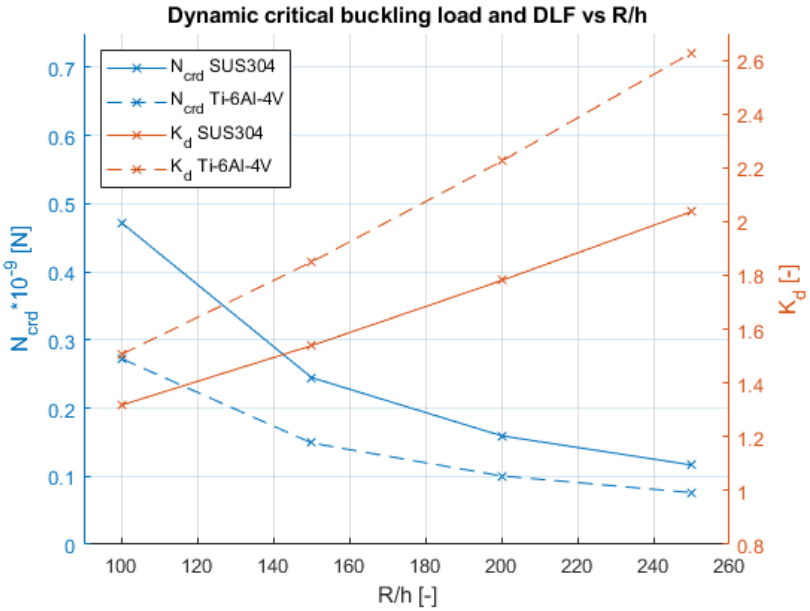

Figure 2.3: R/h vs. dynamic critical load and K_d for SUS304 and Ti-6Al-4V at same loading speed for L=10 with R/L=0.3 (Sofiyev, 2005)

2.4.1. Plasticity

Plasticity is non-linear behaviour of materials when the yield stress in the specimen is reached. For stresses in metals below the yield stress σ_y, the stress is proportional (by the Young's modulus) to the

strain, and materials exhibit elastic behaviour. When the yield stress is reached, the material exhibits plastic behaviour and materials deform permanently. This is often depicted in stress-strain diagrams, as shown by the blue line in Figure 2.4 (DNV, 2013b).

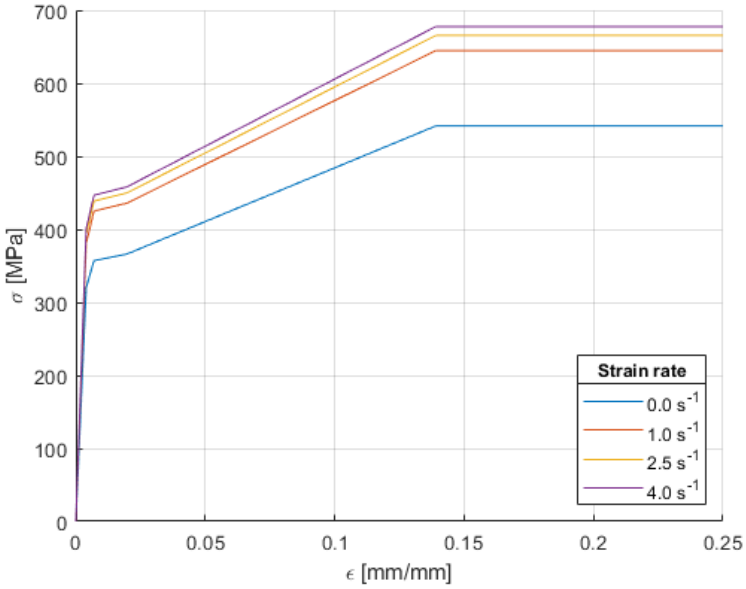

Figure 2.4: Stress-strain curves of S355 steel depending on strain rate (DNV, 2013b)

Whether shell structures fail before they exhibit plastic behaviour depends on the slenderness of the shell (L. Chen et al., 2012). The Eurocodes define the capacity curve, which describes the relationship between relative slenderness λ and the relative buckling strength χ, see Figure 2.5 (NEN, 2007). For cylinders under global bending, the relative slenderness λ and the relative buckling strength χ are defined in Equation 2.7 and Equation 2.8; in these equations M_p is the full plastic buckling moment, see Equation 2.9. M_{crs} is the linear elastic (global) critical buckling moment and M_k is the characteristic buckling load, which is the critical bending buckling load when geometric and material non-linearities, and imperfections are taken into account (L. Chen et al., 2012).

$$\lambda = \sqrt{\frac{M_p}{M_{crs}}} \tag{2.7}$$

$$\chi = \frac{M_k}{M_p} \tag{2.8}$$

$$M_p = \frac{4}{3}\sigma_y \left[\left(r + \frac{h}{2}\right)^3 - \left(r - \frac{h}{2}\right)^3\right] \tag{2.9}$$

2.4.2. Strain rate effect

For high load speeds and thus potentially high strain rates, the strength (yield stress) may increase, and the ductility of the material may decrease. Strain rate can be estimated using Equation 2.10. In this equation, ε is strain, $\dot{\varepsilon}$ is strain rate, v is velocity and L is the length of the specimen. According to DNV-RP-C208, for strain rates greater than $0.1s^{-1}$, this effect may be considered. A model that is often used to simulate this effect is the Cowper-Symonds model, see Equation 2.11 (DNV, 2013b). The stress-strain curves as a result of the Cowper-Symonds model for different strain rates are shown in

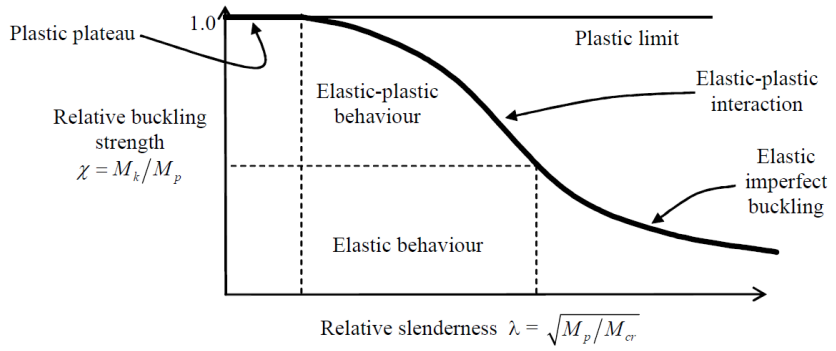

Figure 2.5: EN 1993-1-6 capacity curve for shell buckling (L. Chen et al., 2012)

Figure 2.4.

$$\frac{d}{dt}\varepsilon = \dot{\varepsilon} \approx \frac{d}{dt}\frac{\Delta L}{L} = \frac{v}{L} \tag{2.10}$$

$$\sigma_{dynamic} = \sigma_{static} * \left(1 + \left(\frac{\dot{\varepsilon}}{C}\right)^{\frac{1}{p}}\right) \tag{2.11}$$

2.5. Imperfections

Buckling of shell structures is extremely sensitive to imperfections regarding the buckling load capacity as was shown in Figure 2.1. As a result, experimentally obtained buckling stresses can be as low as 20% of the total critical stress for thin shell structures (Ellinas et al., 1984). Therefore, it is extremely important to implement imperfections in a correct manner. Research also states that for an increase in size of initial geometric imperfections, the dynamic load factor slightly increases; shells with larger imperfections are more sensitive to static loads than to dynamic loads (Zaczynska et al., 2020). For analyses using Finite Element (FE) software, multiple papers use the same method of implementing geometric imperfections. This method makes use of the first buckling mode which imposes this as small imperfections on the original 'perfect' cylindrical shell (Iwicki et al., 2014) (Zaczynska et al., 2020). Li and Kim use the same equation to impose their imperfections by Equation 2.12, which incidentally is the same expression as Timoshenko and Gere give for the deflection of a buckled cylindrical shell (Li & Kim, 2022).

$$w(x,\theta) = w_{max} sin\left(\frac{m\pi x}{L}\right) sin\,(n\theta) \tag{2.12}$$

In this equation, w_{max} is the maximum imperfection amplitude, L the length of the shell, m and n the number of half-waves in the longitudinal and circumferential direction, and x and θ cylindrical coordinates (Timoshenko & Gere, 1961). m and n are always integers and n is always an even integer. Li and Kim have performed a parametric study on the effects of imperfection shapes by varying the number of waves in longitudinal and circumferential direction. They conclude that the sensitivity of the wave number in either direction to the ultimate buckling load is very low for stocky cylindrical shells. The effect of higher wave numbers in either direction for slender cylinders is significant. Imperfection shapes with larger wave numbers correspond to lower ultimate strength of the cylinder (Li & Kim, 2022).

This method is used in both static and dynamic buckling analyses with three different classes of fabrication quality (Iwicki et al., 2014) (Zaczynska et al., 2020). Eurocode 3 gives three different fabrication tolerance quality classes for different sorts of tolerances. These tolerances include out-of-roundness, eccentricity, dimple, and interface flatness tolerances. According to these norms, these tolerances may be treated separately (NEN, 2007).

Wang and Sadowski have also researched the influence of imperfections on the (static) buckling load of cylindrical shells (Wang & Sadowski, 2020). They looked into elastic imperfect shells subjected to axial compression and bending, and the combination thereof. They published two graphs (Figure 2.6)

presenting the variation of elastic nonlinear buckling strength of cylindrical shells under either axial compression or uniform bending. Note that in these graphs, the letter t is used for thickness instead of h, as is used in this thesis. δ is the imperfection amplitude.

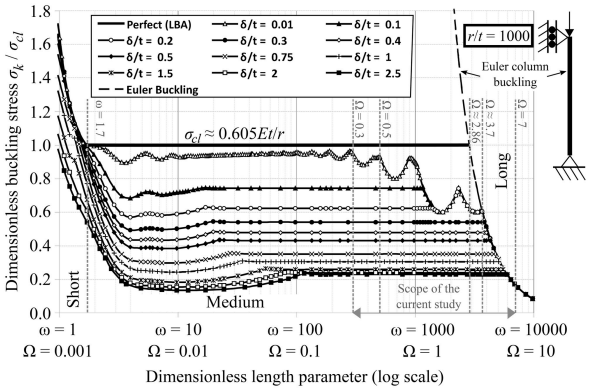

(a) Axial buckling (J. Rotter & Al-Lawati, 2016)

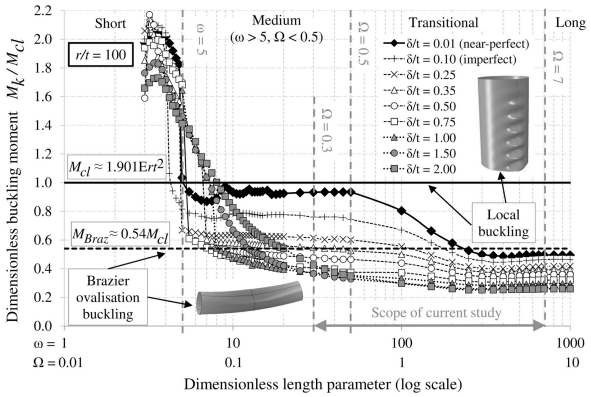

(b) Bending buckling (Wang & Sadowski, 2020) using data from (Fajuyitan & Sadowski, 2018) and (Fajuyitan et al., 2018)

Figure 2.6: Variation of axial (a) and bending (b) buckling load depending on imperfection-to-thickness ratio δ/t

In Figure 2.6a and Figure 2.6b, cylinders are classified based on their length, as this indicates the sensitivity to imperfections and the failure mode. The classification is done using two non-dimensional parameters ω and Ω, see Equation 2.13 and Equation 2.14.

$$\omega = \frac{L}{\sqrt{r * h}} \tag{2.13}$$

$$\Omega = \omega * \frac{h}{r} \tag{2.14}$$

Liang and Li recently posed a new strategy to find the worst buckling shape for buckling in cylindrical panels. This optimisation strategy assumes the worst shape to consist of multiple closely-spaced buckling modes, each with different weights (Liang & Li, 2022). The minimum limit load for shell structures could be found by making use of their strategy. Although the worst imperfection shape seldom occurs in practice, it might be desirable to consider this for safe, efficient design purposes.

2.6. Conical sections

An analytical solution for the static axial buckling load of isotropic conical shells is given in Equation 2.15, in which α is the cone angle (Kouchakzadeh & Shakouri, 2014). They also researched the influence of two joined conical sections with varying thicknesses. It is concluded that the critical static buckling load of two joined truncated cones equals the minimum critical load of each of the sections alone.

$$N_{crs,conical} = \frac{2Eh^2\pi * cos^2\alpha}{\sqrt{3(1-\nu^2)}} \tag{2.15}$$

Jabareen and Sheinman discuss the dynamic buckling of conical isotropic shells in combination with an imperfection sensitivity analysis (Jabareen & Sheinman, 2007). They show that for conical shells, dynamic loading decreases the critical buckling load of cylindrical shells. From the imperfection analysis, they conclude that the larger the imperfections, the higher the sensitivity for both static and dynamic buckling load. For large length-to-radius ratios, the sensitivity to imperfections decreases. This agrees with what was discussed in section 2.5. Regarding the cone angle of the conical section, Jabareen and Sheinman conclude that for larger cone angles, the sensitivity to imperfections decreases in both the static and dynamic case.

2.7. (Stepwise) variable thickness

As discussed in section 2.3, thickness plays a major role in the buckling capacity of shells. Different studies have been done on the influence of the variation of thickness. Fan et al. researched the axial dynamic buckling of cylindrical shells with gradual thickness variation (Fan et al., 2016). Sofiyev and Aksogan did research into conical shells with gradual thickness variation. They concluded that for dynamic buckling of conical cylinders the effect of thickness variation is larger than for static buckling (Sofiyev & Aksogan, 2004). For stepwise thickness variation, the larger the variation in thickness, the larger the reduction in critical static buckling load according to Chen et al. (2012). This can be attributed to higher stress concentrations around sudden changes in cross-sections. More severe changes in cross-sections result in larger stress concentrations and thus lower critical buckling capacity. The static buckling load for a cylinder with a stepwise variable thickness is given in Equation 2.16 (Z. Chen et al., 2012). In this equation, h_{upper} and h_{lower} indicate the shell thickness above and below the stepwise change respectively.

$$P = \left[1 - \left(\frac{h_{upper} - h_{lower}}{h_{upper} + h_{lower}}\right)^2\right] * \frac{1}{\sqrt{3(1-\nu^2)}} \frac{E}{R} * \left(\frac{h_{upper} + h_{lower}}{2}\right)^2 \tag{2.16}$$

2.8. Submerged sections

Monopiles are used as foundations for offshore wind turbines. They are embedded in the seabed for a significant part of their length, and most of their length above seabed is submerged in water. This influences the dynamic buckling strength due to the added mass effect. When a submerged structure deforms, the surrounding water has to move as well. This water should be accounted for as extra inertia. Therefore, submerged cylinders will have larger dynamic load factors due to larger dynamic buckling strength (Sun et al., 2022).

Monopiles are installed as hollow cylinders, with small cutouts to accommodate the passage of electricity cables, and thus there is water both inside and outside of the monopile. This results in even hydrostatic pressure profiles on both sides of the cylinder. Research on submerged cylinders with one 'dry' side is therefore not relevant because external pressure results in different pressure profiles and an extra loading mechanism monopiles do not experience.

FSI has a complicated nature due to the interactivity between solid deformations and fluid flows. It is often modelled by an added mass coefficient to take the extra inertia into account (Sun et al., 2022). By modelling the surrounding fluid as added mass, it is evident that the critical dynamic load is increased. The significance of the FSI is hard to predict but could be substantial. However, lots of time would have to be spent to accurately incorporate these effects in a model. Therefore, as mentioned in 1.2.2, FSI will be disregarded in this thesis due to time constraints.

3

Methodology

In this chapter, the methodology is described briefly.

3.1. Research method

Different methods can be used in order to answer the research questions described in chapter 1. The chosen method for this research is to make use of FE models and validate those models using analytical solutions. The software that will be used is Ansys Workbench (ANSYS, 2021).

FE models are chosen as the main method because they are suited for parametric studies and cheaper than setting up an experiment. The accuracy of FEA depends on the quality of the model and should be analysed. This will be done by validating the model with analytical solutions. Mesh convergence studies will be done to ensure a fine enough mesh that will model reality. Analytical solutions are chosen to validate the FE models because this less time-consuming than conducting multiple experiments for each characteristic of monopiles.

3.2. Analytical models

An existing analytical model for the calculation of the critical dynamic buckling load for axial forces is used to validate the FE model later on, and to investigate the influence of parameters on the critical load (Sofiyev, 2005).

First, the analytical model is recreated so different geometries can be put in to validate the FE model later on. The recreated model is validated using results from the same paper. Then, a parametric study is done for different parameters. The chosen parameters are based on current and future monopile dimensions. The different sorts of steel used in monopiles only differs in yield strength, not in density, Young's modulus, or Poisson's ratio. Also, the model from Sofiyev is an elastic model (2005). This means that the influence of plastic material properties cannot be investigated using this model. This leaves geometric parameters R and h, and the loading rate.

The goal of the parametric study is to identify the influence of different parameters on the axial dynamic buckling capacity. There are differences between the influence of parameters in static axial and bending analyses. However, there are also similar trends to be recognised since Equation 2.2 and Equation 2.6 are very similar in nature. It is interesting to see if the dynamic axial and bending buckling loads exhibit comparable similarities. Therefore, the desired result of the parametric study is to have an overview of the influence of different parameters on the dynamic axial buckling load. At last, this is used in combination with existing research on dynamic buckling to answer subquestion 1.

3.3. FE model

Non-linear finite element models are created using Ansys Workbench (ANSYS, 2021). The non-linearities that are taken into account include large deformations and plasticity. Imperfections are modelled as well. Recommended practice is followed for geometry modelling including imperfections, material modelling, and for selection and size of elements (DNV, 2013b).

First, a simple static finite element model is built to simulate bending buckling. Published data of the dimensionless buckling moment of imperfect shells under uniform bending is used to validate this model (Wang & Sadowski, 2020). Next, dynamic axial buckling is modelled and validated using the analytical model described in chapter 4. Based on these two models, a final model is created to simulate dynamic bending buckling.

The FE model is used to simulate load cases with varying loading rates on different geometrical and material properties. As mentioned in section 3.2, a parametric study is done to evaluate the influence of different parameters on the critical buckling load. This study and existing research on shell buckling is used to determine appropriate model parameters. Besides the parameters as given by the analytical model in chapter 4, also the length is considered to be of importance since Wang and Sadowski demonstrated that the length influences the buckling mode (2020).

The desired results of the FE model are trends of how the loading rate influences the dynamic load factor for different (non-dimensional) monopile dimensions. It should be possible to draw conclusions regarding the dynamic bending buckling capacity of monopiles. Furthermore, the buckling modes will be compared for different geometries and loading rates. In turn, these will be compared with buckling modes of static load cases to see the influence of loading rate on the buckling mode.

The results of the FEA will be used to answer subquestion 2 and the main research question of how the loading rate influences dynamic buckling of monopiles subjected to bending moments.

4

Analytical Models

In this chapter, the analytical models that are used to validate the FE model are discussed. Non-dimensional parameters are also discussed in order to be able to accurately compare different geometries.

4.1. Axial dynamic buckling

To validate the axial dynamic buckling, a model of Sofiyev is used (2005). The analytical derivation for the Equations of Motion (EoM) resembles derivations from earlier papers of the same author (Aksogan & Sofiyev, 2002) (Sofiyev & Aksogan, 2004). In his paper, Sofiyev provides an analytical solution for the stability behaviour of cylindrical shells made of composite materials, more specifically a mixture of ceramics and metals. The assumption is made that the composite material varies from top to bottom in the surface. The effective material properties P are calculated using volume fractions, see Equation 4.1.

$$P_t V_c + P_b V_m = P \tag{4.1}$$

$$V_c + V_m = 1 \tag{4.2}$$

In these equations, P_t and P_b are the properties of the top and bottom materials, V_c and V_m are the ceramic and metallic volume fractions which are related by Equation 4.2. By setting the V_c to zero, the model can be used for metals only. This is also validated in the paper.

The solution method will be discussed briefly.

First of all, the EoM for cylindrical shells are given in Equation 4.3, Equation 4.4 and Equation 4.5.

$$\frac{\partial T_x}{\partial x} + \frac{\partial T_{xy}}{\partial y} = \rho h \frac{\partial^2 u}{\partial t^2} \tag{4.3}$$

$$\frac{\partial T_{yx}}{\partial x} + \frac{\partial T_y}{\partial y} = \rho h \frac{\partial^2 v}{\partial t^2} \tag{4.4}$$

$$\frac{\partial^2 M_x}{\partial x^2} + 2\frac{\partial^2 M_{xy}}{\partial x \partial y} + \frac{\partial^2 M_y}{\partial y^2} + \frac{T_y}{R} + T_x^0 \frac{\partial^2 w}{\partial x^2} + 2T_{xy}^0 \frac{\partial^2 w}{\partial x \partial y} + T_y^0 \frac{\partial^2 w}{\partial y^2} = \rho h \frac{\partial^2 w}{\partial t^2} \tag{4.5}$$

A local curvilinear coordinate system is used, which is located on the mid-plane of the shell, see Figure 4.1. By using such a coordinate system, Sofiyev approaches the cylinder as a plate. $T(t)$ is the axial load. In these equations, T_x, T_y, T_{xy} are the internal force resultants per unit length of the cross-section of the shell, M_x, M_y, M_{xy} are the

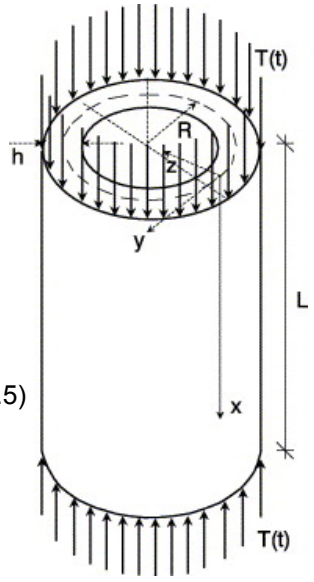

Figure 4.1: Coordinate systems used by (Sofiyev, 2005)

internal moment resultants per unit length, T_{xy}^0 and T_y^0 are the membrane circumferential force and shear force for the condition with zero initial moments, u, v, w are the incremental displacement components on the reference surface in the directions of the x, y, and z axes respectively, and ρ is the mass density.

By making use of the strain compatibility equation, Airy stress function ($\overline{\Phi} = \frac{\Phi}{h}$), and Love's shell theory, a system of two differential equations is created (Sofiyev, 2005). The shell is assumed to have hinged supports, and therefore, the form of the solutions is assumed to be in the form of Equation 4.6 and Equation 4.7. ξ and ζ are time dependent amplitudes, m and n are the half wave number in the axial direction and the wave number in circumferential direction respectively. As mentioned, w is the incremental displacement component in the z-direction and Φ is introduced as Airy stress function.

$$w = \xi(t) sin\left(\frac{m\pi x}{L}\right) cos\left(\frac{ny}{R}\right) \tag{4.6}$$

$$\Phi = \zeta(t) sin\left(\frac{m\pi x}{L}\right) cos\left(\frac{ny}{R}\right) \tag{4.7}$$

By making use of the Galerkin's method over the complete range of the cylindrical shell $0 \leq x \leq L$ and $0 \leq y \leq 2\pi R$, a differential equation of the form of Equation 4.8 is found (Shames & Dym, 2013). In this equation, λ is a linear function of time, dependent on the geometrical and material properties of the shell, and τ is dimensionless time parameter where $t = \tau t_{cr}, 0 \leq \tau \leq 1$. Equation 4.8 can be solved using the method of Sachenkov and Baktieva (Aksogan & Sofiyev, 2002). This method results in solutions for the amplitude of the radial displacement ξ, see Equation 4.9 and Equation 4.10. The variable p is a dimensionless parameter used later on to minimise a Hamiltonian energy function. A_1 and A_2 fall out during the rest of the solution process.

$$\frac{d^2\xi}{d\tau^2} + \lambda(\tau) t_{cr}^2 \xi = 0 \tag{4.8}$$

$$\xi(\tau) = A_1 e^{p\tau} \tau^2 \left(\frac{p+3}{p+2} - \tau\right) \tag{4.9}$$

$$\xi(\tau) = A_2 e^{p\tau} \tau \left(\frac{p+2}{p+1} - \tau\right) \tag{4.10}$$

Equation 4.9 and Equation 4.10 are substituted in Equation 4.8, and a Lagrange-Hamilton energy function is obtained, dependent on the geometrical and material properties, load speed (via the critical time t_{cr}), and axial and circumferential wave numbers. For high load speeds, cylinders experience an axisymmetric loss of stability: the circumferential wave number n equals zero. This assumption is used in order to solve the energy function. By minimising this function, the dynamic critical axial load is found. The energy function is minimised by minimising the amplitude of the radial displacement ξ, which is done by varying the values of p.

Maple and MATLAB are used to implement this method.

4.2. Parametric study

In this section, the model described in section 4.1 is used to determine the influence of different parameters on the dynamic load factor. It is assumed that the dynamic buckling load for both axial and bending cases is dependent on basically the same parameters since this is also the case for static buckling loads, see Equation 2.2 and Equation 2.6. However, length also plays a role in bending buckling according to (Wang & Sadowski, 2020).

4.2.1. Geometric ratios L, R, h

As discussed in chapter 1, existing monopiles have diameters up to 8m with a thickness of up to 100mm. Future monopiles are expected to have these dimensions increased to a diameter of around 14m and a

thickness of 140mm. This means that the R/h ratio is around 50 for large future monopiles. Currently, the R/h values range from about 30 to 90, differing per section. These dimensions are reflected by the parameters used in the parametric study.

Figure 4.2 shows the relation between the thickness and the dynamic load factor at different load speeds. The diameter is set to $R = 4.0m$. For smaller thicknesses (and thus larger R/h ratios), the dynamic load factor increases for the same load speed. This means that the dynamic buckling capacity increases more than the static buckling capacity for increasing thicknesses.

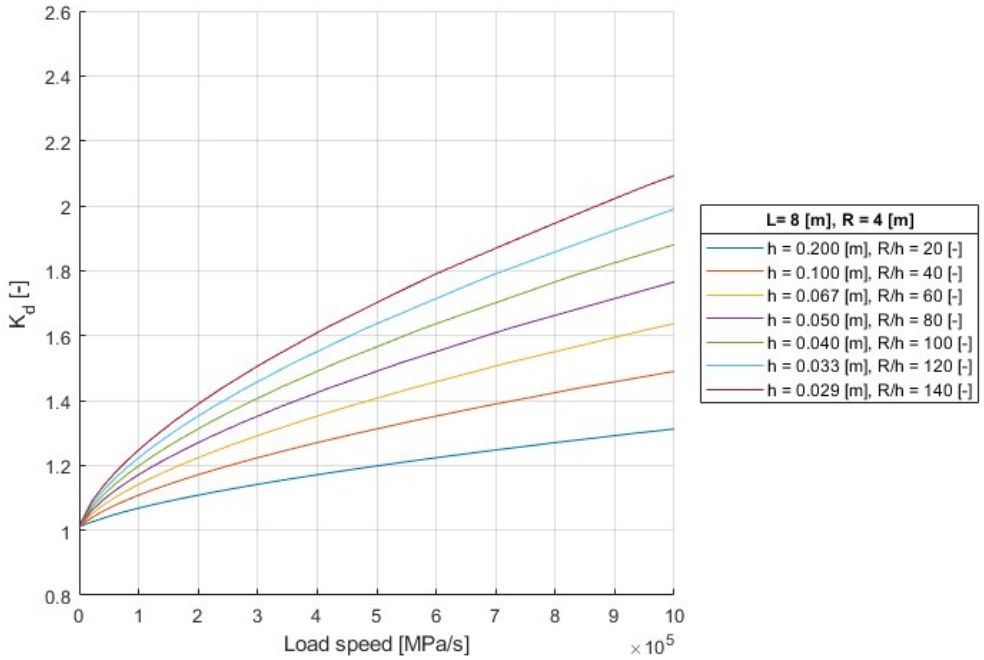

Figure 4.2: Influence of the thickness h on the dynamic load factor K_d

Figure 4.3 shows the influence of the radius on the dynamic load factor. The thickness is set to a value of $h = 0.05m$. The figure shows that for larger diameters (and thus larger R/h ratios), the dynamic load factor increases. This means that for larger diameters the dynamic buckling capacity increases more than the static buckling capacity.

Figure 4.2 and Figure 4.3 showed that larger R/h ratios correspond to larger values of K_d. Figure 4.4 shows the influence of varying values for the radius and the thickness with a constant R/h ratio. Larger cylinders have higher dynamic load factors. This means that for larger cylinders the dynamic buckling capacity increases relatively more than the static capacity.

It can be concluded from Figure 4.2 and Figure 4.3 that the dynamic axial buckling capacity increases more than the static capacity for cylindrical shells with larger R/h ratios due to either larger diameters or smaller thicknesses.

4.2.2. Non-dimensional parameter

The loading rate has unit of $[Ns^{-1}$ for axial loading and $[Nms^{-1}$ for bending moments. This section expands on making the loading rate non-dimensional. This is done by dividing the loading rate by the critical static capacity of a cylinder, which gives the relative loading rate. For the loading rate to be completely dimensionless, it is also divided by the natural frequency f_n of the structure. This is shown in Equation 4.11

$$\overline{F} = \frac{\dot{F}}{N_{crs} * f_n} \tag{4.11}$$

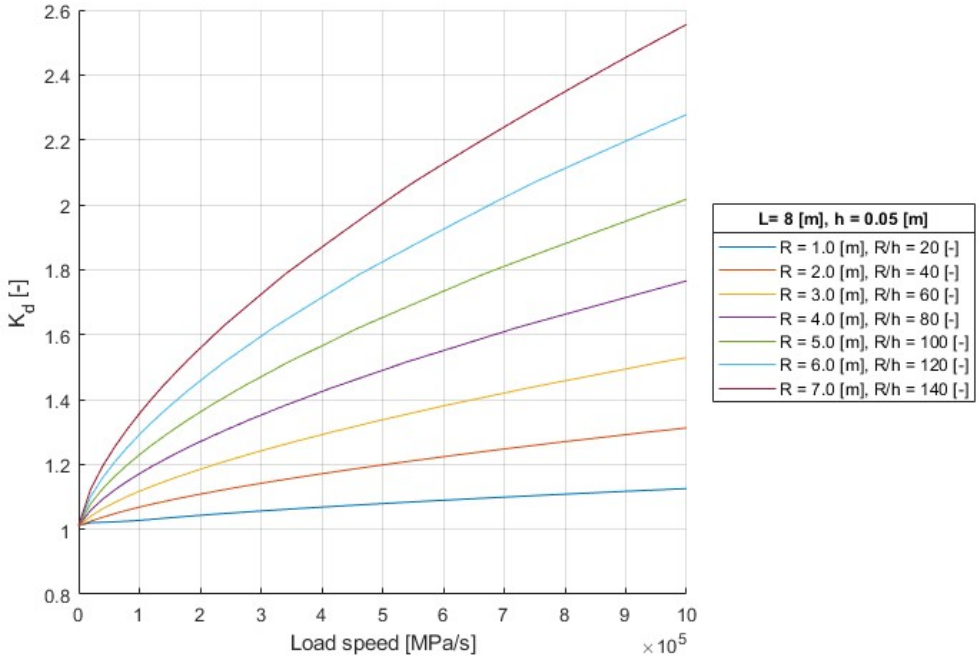

Figure 4.3: Influence of the radius R on the dynamic load factor K_d

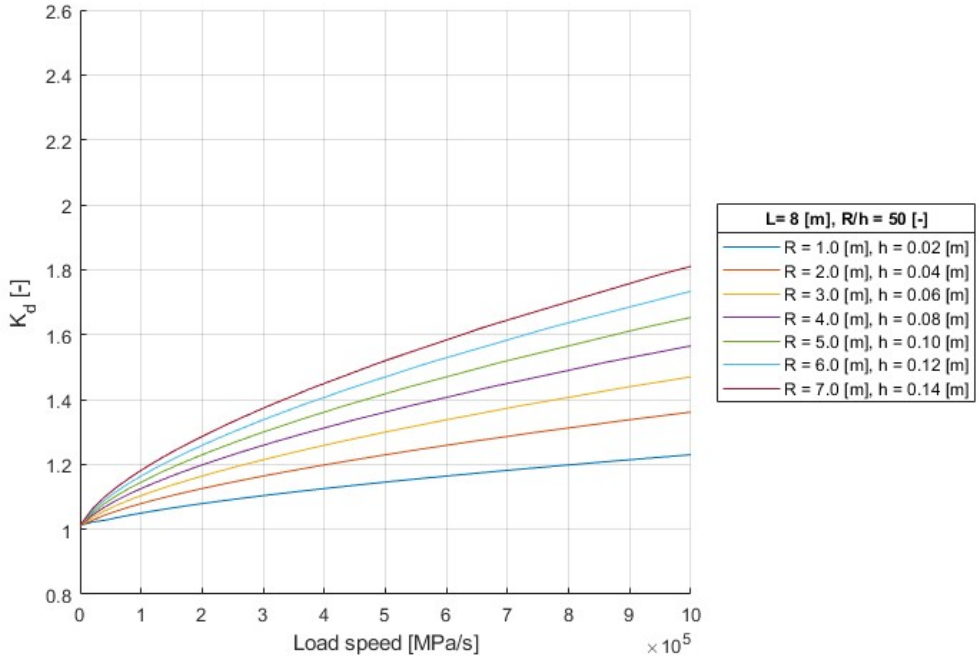

Figure 4.4: Influence of varying radius R and thickness h, with constant R/h ratio, on the dynamic load factor K_d

The natural frequency of a simple mass-damper system is calculated by Equation 4.12, where m is the mass of the system and k is the spring stiffness of the system. The natural frequency of a cylindrical shell is based on the same principle, but mathematically more complex. Therefore, FEA is used to identify the natural frequencies of cylinders with L/R and R/h values as described in Table 5.6. The FE model will be expanded on in chapter 5. The natural frequencies are shown in Table 4.1.

$$f_n = \sqrt{\frac{k}{m}} \tag{4.12}$$

Table 4.1: Natural frequencies

#	L	R	h	L/R	R/h	f_n
1	8	2.67	0.0889	3	30	51.99
2	8	2.00	0.0667	4	30	45.55
3	8	1.60	0.0533	5	30	39.95
4	8	1.33	0.0444	6	30	35.22
5	8	2.67	0.0533	3	50	51.89
6	8	2.00	0.0400	4	50	45.48
7	8	1.60	0.0320	5	50	39.90
8	8	1.33	0.0267	6	50	35.18
9	8	2.67	0.0381	3	70	51.85
10	8	2.00	0.0286	4	70	45.44
11	8	1.60	0.0229	5	70	39.87
12	8	1.33	0.0190	6	70	35.16
13	8	2.67	0.0296	3	90	51.82
14	8	2.00	0.0222	4	90	45.42
15	8	1.60	0.0178	5	90	39.86
16	8	1.33	0.0148	6	90	35.15

It is clear from Table 4.1 that for cylindrical shells, the radius of the cylinder has more influence on the natural frequency than the thickness of the shell. Furthermore, looking back at Equation 4.12, f_n is also dependent on the mass and the stiffness of the cylinder. For solid structures, this translates to mass and Young's modulus. By using the natural frequency to non-dimensionalise the loading rate, one takes material into account as well.

In , the dynamic load factor versus the dimensionless loading rate of the above mentioned geometries are shown. From this graph, it seems that larger L/R ratios correspond to larger a K_d and larger R/h ratios correspond also to larger a K_d. The graphs as mentioned in subsection 4.2.1 show the same trend for larger R/h ratios. However, larger L/R ratios correspond to smaller a K_d.

4.3. Loading rate calculation

Since the FEA model runs in displacement-mode, the loading rate cannot be set automatically in Ansys. However, the loading rate can be calculated analytically as will be shown in this section for both axial and bending loading. Both calculations are done in a similar manner, where the Young's modulus E plays an important role in the calculation. However, this is only valid for elastic deformation. The load rate after the onset of plasticity is calculated the same way, only the tangent modulus E_t should be used instead of the Young's modulus E. The moment in time at which the deformation of the cylinders enters the plastic regime is calculated using the formula for the plastic bending moment, Equation 2.9, and the loading rate $\dot{M}$.

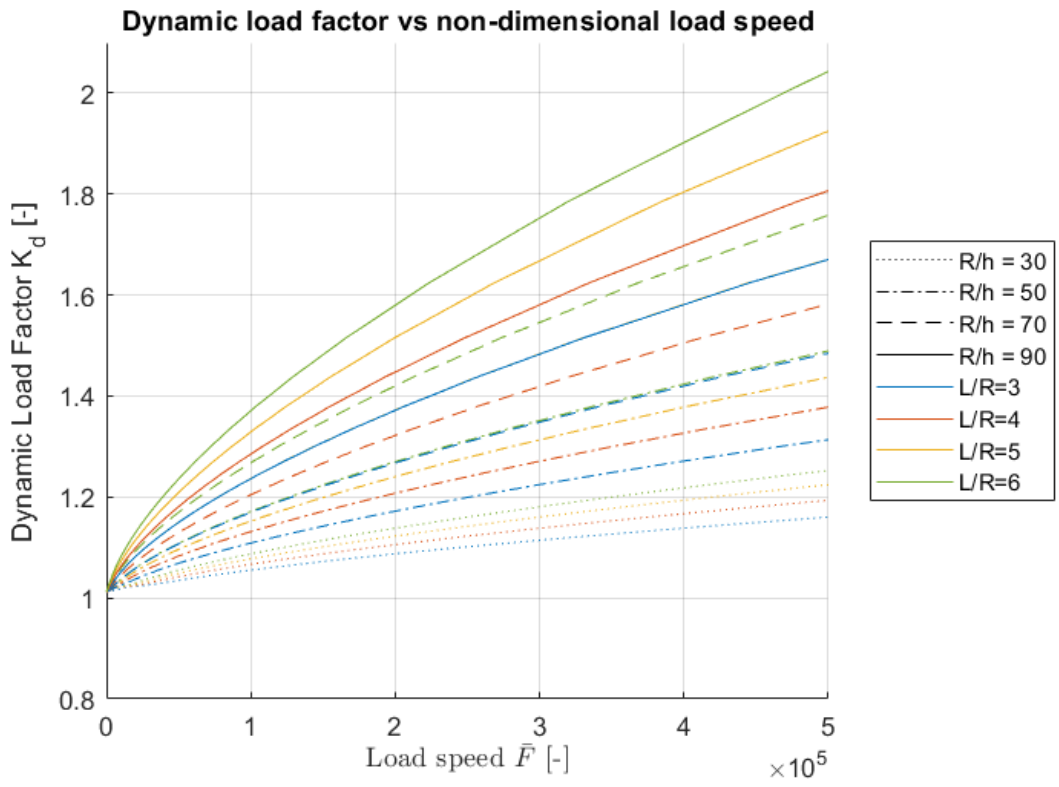

Figure 4.5: Non dimensional parameter $\bar{F}$ vs dynamic load factor K_d

4.3.1. Axial loading rate calculation

The calculation of the axial loading rate is discussed first. For this calculation, Equation 4.13 to Equation 4.15 are used. F is the axial force, and A is the cross-sectional area.

$$\sigma = \frac{F}{A} \tag{4.13}$$

$$\sigma = E\varepsilon \tag{4.14}$$

$$\varepsilon \approx \frac{\Delta L}{L} \tag{4.15}$$

$$\sigma = \frac{F}{A} = E\varepsilon \approx E\frac{\Delta L}{L} \tag{4.16}$$

The loading rate is determined analytically using the equation for axial stress (Equation 4.13) and Hooke's law (Equation 4.14). The force F is related to the strain ε, the Young's modulus E, and the cross-sectional area A, see Equation 4.16. This equation is rewritten as Equation 4.17.

$$F = EA\frac{\Delta L}{L} \tag{4.17}$$

Since the loading rate is to be determined, the derivative in time is taken from both sides of Equation 4.17. On the right side, only the displacement is taken as time-dependent. Equation 4.18 is the resulting relation between the loading rate, and the material and geometrical properties and the speed with which the displacement in the simulation should run.

$$\frac{d}{dt}(F) = \dot{F} = \frac{EA}{L}\frac{d}{dt}(\Delta L) = \frac{EA}{L}\dot{x} \tag{4.18}$$

4.3.2. Bending loading rate calculation

The calculation for the bending loading rate is done in a similar manner, Equation 4.19 is the equation for the bending stress instead of Equation 4.13 for the axial stress. Besides Hooke's law, equations

for the bending strain (Equation 4.20) and the radius of curvature(Equation 4.21) are used to relate the moment M to the strain ε, the Young's modulus E, the distance to the neutral surface, and the moment of inertia I. In these equations, y is the distance from the neutral surface to the measuring point (thus, in case of shell structures the radius), I is the moment of inertia of the cross-sectional area about the neutral axis, ζ is the radius of curvature, s is the length of the curve (in this case the length L of the cylinder) and α is the angle.

$$\sigma = \frac{My}{I} \tag{4.19}$$

$$\varepsilon \approx -\frac{y}{\zeta} \tag{4.20}$$

$$\zeta = \frac{s}{\alpha} = \frac{L}{\alpha} \tag{4.21}$$

$$\sigma = \frac{My}{I} = -\frac{Ey}{\zeta} \approx -\frac{Ey}{L}\alpha \tag{4.22}$$

By combining the above equations, a relation is found between the moment M, and the material and geometrical properties and the angle, see Equation 4.22. This can be rewritten to Equation 4.23.

$$M = -\frac{EI}{L}\alpha \tag{4.23}$$

Again, the derivative of the equation is taken to determine the loading rate. On the right side, only the angle α is time-dependent. Equation 4.24 shows the resulting equation for the bending loading rate. The unit of the angle α is radians.

$$\dot{M} = \frac{d}{dt}(M) = -\frac{EI}{L}\frac{d}{dt}(\alpha) = -\frac{EI}{L}\dot{\alpha} \tag{4.24}$$

5

Finite Element Model

5.1. Modelling choices

In this section, the steps and choices are discussed to build the FE model. The validation process is explained as well.

5.1.1. Analysis type

The simulations are done using Ansys Workbench 2021 R2 (ANSYS, 2021). First of all, the geometry is created in SpaceClaim. The parameters L, R, and h are parameterised using the scripting possibilities. The geometry is loaded into a static structural analysis in which the cylinder is loaded with a force of 1 Newton in order to create pre-stress. This is necessary to perform an eigenvalue buckling analysis to calculate the linear critical buckling stress, different mode shapes and their maximum deflections. After the eigenvalue buckling analysis, buckling modes are imposed on the geometry to simulate imperfections. This will be discussed in further detail in subsection 5.1.6. The final step is either an explicit or a transient analysis. The full procedure is shown in Figure 5.1

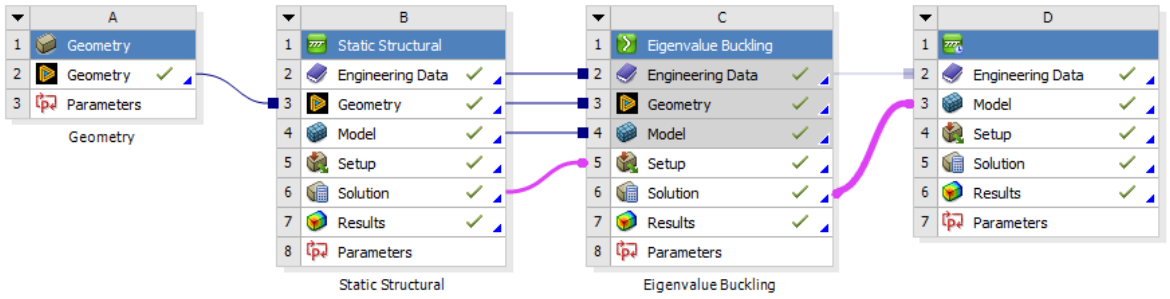

Figure 5.1: Overview of the FE model. System A: geometry, system B: pre-stress, system C: Eigenvalue buckling, system D: Implicit/Explicit analysis

A modal analysis is done in order to calculate the eigenfrequencies of the cylinder. It was discussed in chapter 2 that natural periods of cylinders could have an influence on the dynamic buckling strength. Therefore, the natural periods of the geometry are calculated as well.

The static buckling analysis is solved using an implicit solver (transient analysis) whereas the dynamic simulations are done using an explicit solver. This is due to the nature of the solvers with respect to the duration of the simulations. A transient analysis is better suited for longer duration and an explicit solver is a better fit for short duration.

There are three main ways to perform a buckling analysis using FE software: force-controlled loading, displacement-controlled loading and arc-length displacement controlled loading. Force controlled

loading can cause convergence issues due to the nature of the solver algorithm. Due to the manner in which for example the Newton-Raphson procedure works, at the critical load, there is a large displacement increment but no force increment. This causes divergence, as is shown in Figure 5.2. When running the analysis in displacement mode, a continuous displacement increment is imposed on the structure for which the force can be calculated. This often solves the convergence issues. The last method is the arc-length method which can also handle so called 'snap-back' for highly nonlinear systems. This is shown in Figure 5.3 on the right. This is not discussed further as this option is not available in transient or explicit analyses in Ansys, which is necessary for the dynamic conditions studied in this thesis.

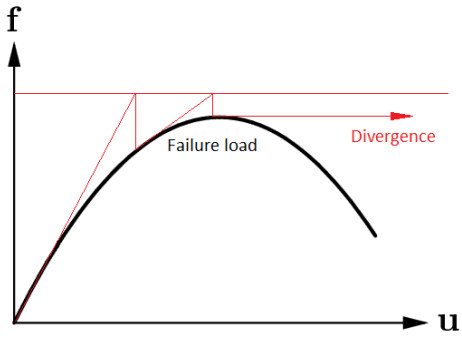

Figure 5.2: Visualisation of convergence problems using force-controlled loading (own figure)

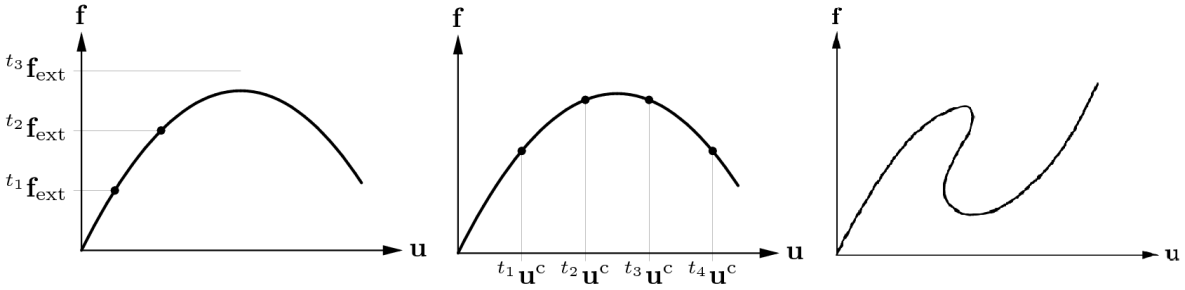

Figure 5.3: From left to right: force-control, displacement-control, snap-back (arc-length) (TNO DIANA BV, 2011)

5.1.2. Mesh

The uploaded geometry is discretised by splitting it up into small elements. The size and type of the elements influence the accuracy of the solution. The element order must be linear for explicit dynamics analyses. Therefore, this analysis makes use of the linear SHELL181 element type. This element is suited for shell structures with thin to moderate thicknesses with large strain and rotations in nonlinear analyses (ANSYS, Inc, 2011).

The size of the elements is determined by doing a convergence study. The analysis is run for different element sizes. At a certain element size, the solution converges and smaller element sizes do not give a more accurate solution.

The mesh is shown in Figure 5.4; square elements with edge lengths of 0.10m are selected after the convergence study. The convergence study was done for a cylinder with a radius of 1.33m, which is the smallest radius of curvature that is used in the simulations. There will be more elaboration on the dimensions that are used in section 5.3.

5.1.3. Boundary conditions

The boundary conditions are imposed on the model using remote points. Remote points create multi-point constraint equations to set the same boundary conditions to multiple nodes at once. This reduces the possibility of over-constrainted models (ANSYS, Inc, 2021). An example is shown in Figure 5.5. A remote point is created with infinitely stiff connections to the nodes at both ends of the cylinder. Then,

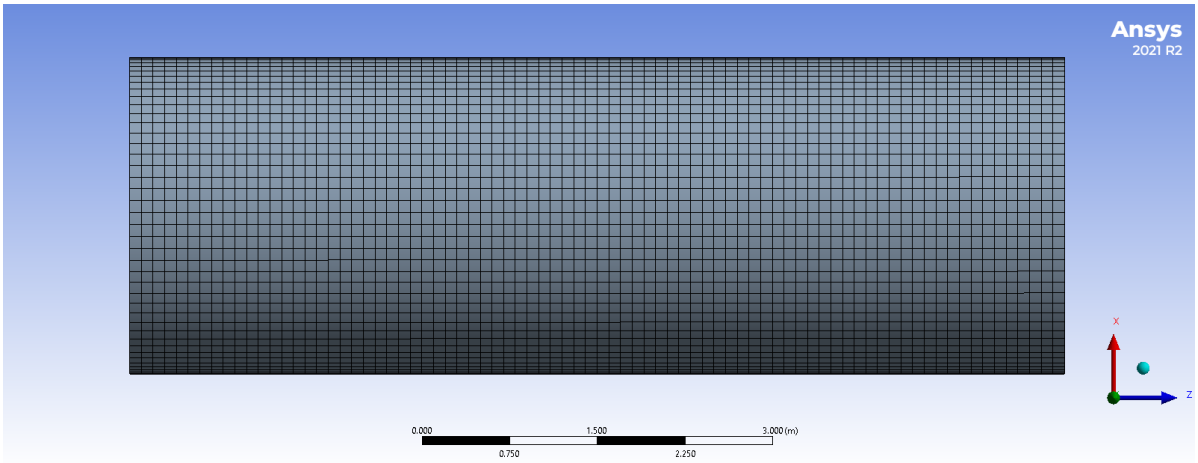

Figure 5.4: Cylinder with visible mesh

boundary conditions are imposed on this remote point. The behaviour of the remote point is set to rigid, which means the shape of the cylinder will not deform and thus the ends are simply supported. An equal rotation is applied to both ends to realise buckling.

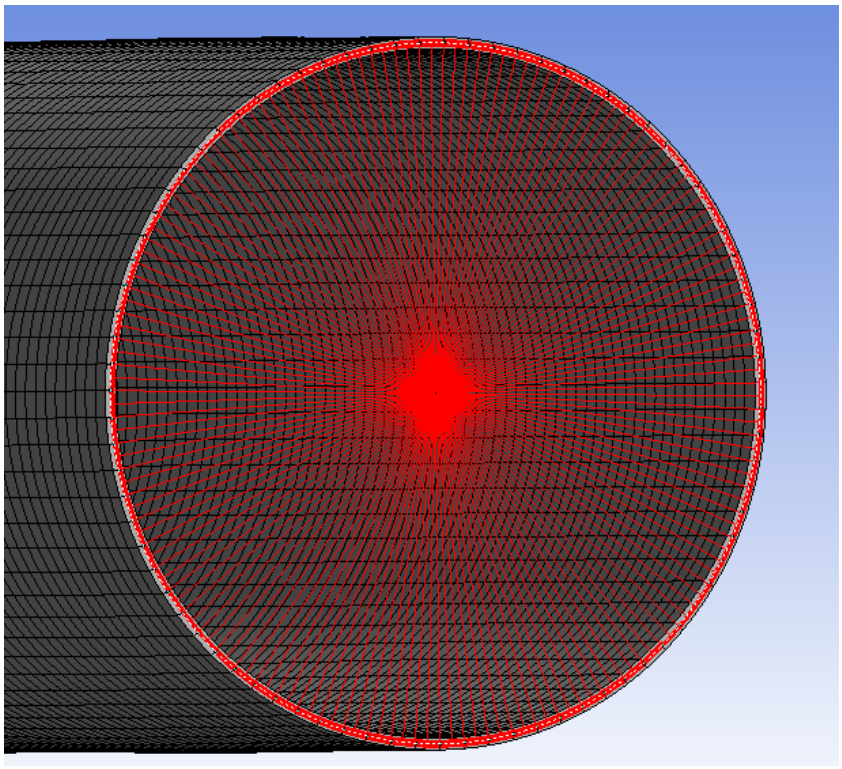

Figure 5.5: One end of the cylinder with a remote point used to impose boundary conditions

5.1.4. Loading profile

The loading profile that exerts the rotation on the ends of the cylinder is discussed in this section. The goal is to end up with a linear loading curve so a constant loading rate is obtained. The linear part should be reached without having infinite acceleration at the start of the profile, since this gives infinite reaction forces according to Newton's second law. Therefore, Equation 5.1 is used to smoothly ramp up to the right loading rate. The derivative (the acceleration of the loading rate) of Equation 5.1 is non-zero and non-infinite and thus the reaction forces will also be finite.

$$a = A_0 + (A_1 - A_0) * \xi^3 * \left(10 - 15\xi + 6\xi^2\right)$$
$$with \quad \xi = \frac{t - t_0}{t_1 - t_0} \tag{5.1}$$

Since the load profile for explicit analyses in Ansys can only be put in tabular data, Equation 5.1 is discretised. The profile is built up in such a way that when the slope of the curve equals the slope necessary to reach the desired amplitude at the desired end time, the linear part of the curve starts. This way, every load profile for every end time has exactly the same ramp up and can be compared properly to each other. The load curves are shown in Figure 5.6; the start of all curves is zoomed in on to show they follow the same path.

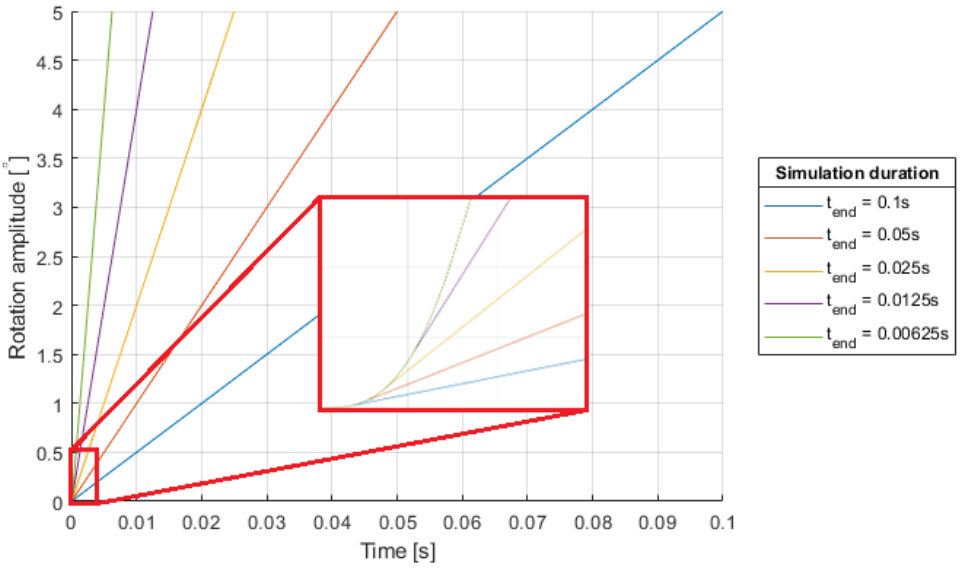

Figure 5.6: Load curves used for each simulation duration

The aim is to have a constant loading rate throughout the simulation, while following the same ramp up curve. Therefore, the loading curve should be linear as quickly as possible. Table 5.1 shows the fraction of the curve that is nonlinear. Due to the similar ramp up curve at the start, it is inevitable that for the steepest curve, the ramp up takes up most of the total loading curve. The choice for t_1 in Equation 5.1 is made based on a trade-off between a more linear curve and a steeper ramp up, causing stress-wave peaks in the moment reaction graph. After careful consideration, $t_1 = 1.5ms$ is chosen.

Table 5.1: Percentage of non-linear part (ramp up) of the total loading profile

$T_{end}[s]$	**0.1**	**0.05**	**0.025**	**0.0125**	**0.00625**
Ramp up [%]	0.04	0.10	0.28	0.82	2.40

5.1.5. Material model

Plasticity is taken into account, and so a material model should be chosen accordingly. Only isotropic hardening models are considered as these are well-suited for monotonic buckling analyses. Ansys offers either a bi-linear or a multi-linear model. The multi-linear model describes real stress-strain curves in more detail than the bi-linear curve.

However, as defined in chapter 4, Equation 4.23 is used to calculate the loading rate. The loading rate is dependent on the Young's modulus E, which is the slope of the stress-strain diagram. In a multi-linear model, the slope (E) differs for different stress levels and so the loading rate will vary as well during the simulation. Therefore, the assumption of a bi-linear material model is made.

A bi-linear model still has two slopes and therefore the loading rate still varies throughout the simulation. However, as Figure 5.7 shows, the maximum total strain during a buckling simulation almost immediately surpasses the elastic region. The maximum strain of the elastic region for S355 steel with material properties according to (DNV, 2013b), equals $1.65 * 10^{-3} m/m$, as shown in Equation 5.2.

$$\varepsilon = \frac{\sigma_y}{E} = \frac{346.9MPa}{210GPa} = 1.65 * 10^{-3} m/m \tag{5.2}$$

The elastic deformation is negligible in comparison to the plastic deformation and thus the assumption of purely plastic buckling is made. This means that the loading rate $\dot{M}$ can be calculated using the tangent modulus E_t to reasonable accuracy.

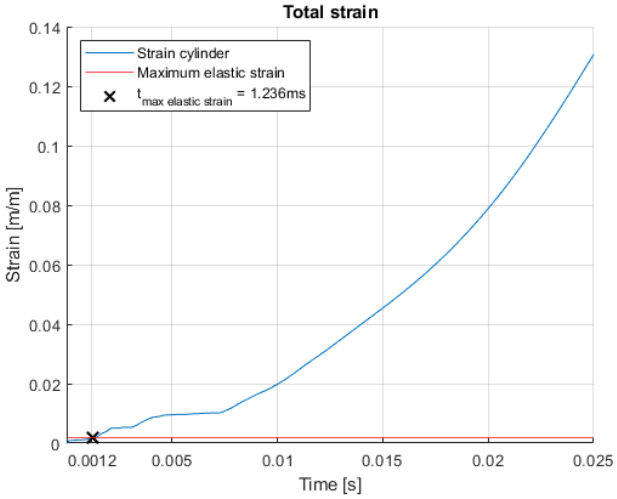

Figure 5.7: Maximum total strain of a S355 cylinder (L = 8m, R = 1.33m, h = 0.0444m) subjected to 10°rotation in t = 0.025s

The tangent modulus E_t used in the material models is taken as $E/100$ according to (DNV, 2013b). This value is not taken as zero because this would result in infinitely large strains and thus numerical instability of the model.

Strain rate effects, as discussed in chapter 2, are not taken into account to decouple the inertial effects. This could mean that the FE model slightly underestimates critical buckling strength.

5.1.6. Imperfections

In section 2.5, multiple methods to deal with imperfections are discussed. This research makes use of the same method as (Iwicki et al., 2014) and (Zaczynska et al., 2020). The first shell buckling mode shape is imposed on the geometry in order to mimic imperfections. The buckling shape from an axially loaded model is used because it produces a uniform imperfection pattern. The eigenvalue buckling analysis gives the imperfection shape and a maximum deflection. This is shown in Figure 5.8.

This deflection is scaled in order for the maximum value to match the recommended values for dimple tolerance as given in EN 1993-1-6 (NEN, 2007). The procedure is discussed briefly. For real cylinders, the depth of the dimples (Δw_{0x}) is measured using a gauge length l_{gx}, see Equation 5.3.

$$l_{gx} = 4\sqrt{rh} \tag{5.3}$$

Next, this depth is assessed by calculating the dimple tolerance parameter U_{0x} using Equation 5.4. The fabrication class can then be determined with the recommended value of the dimple tolerance parameter, $U_{0,max}$, Equation 5.5, and Table 5.2.

$$U_{0x} = \frac{\Delta w_{0x}}{l_{gx}} \tag{5.4}$$

$$U_{0x} \leq U_{0,max} \tag{5.5}$$

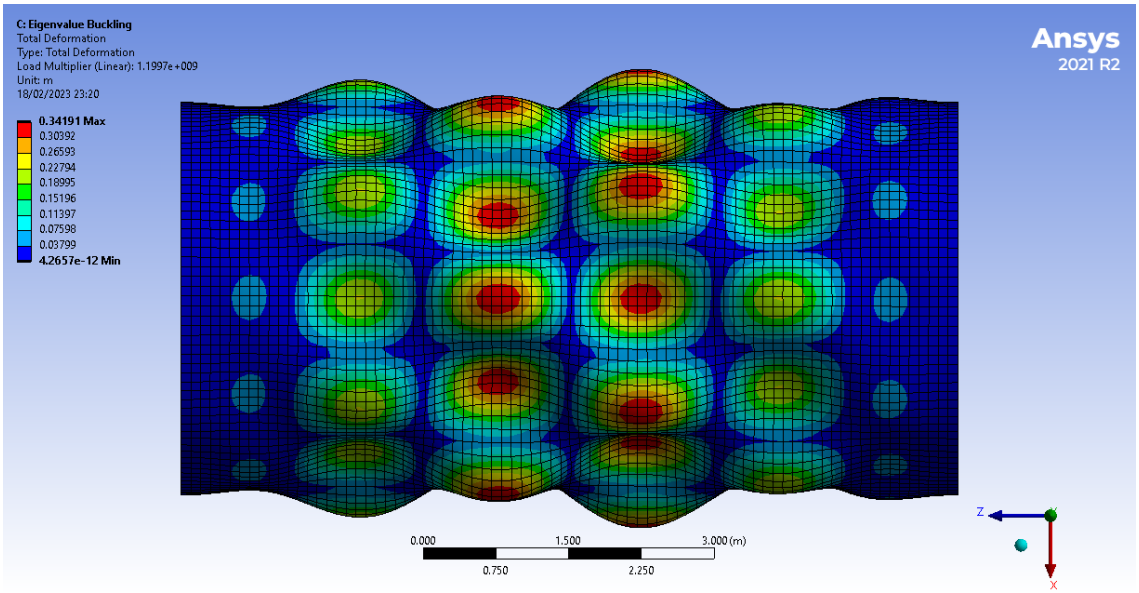

Figure 5.8: First shell mode shape as given by Ansys eigenvalue buckling analysis

The first mode shape is imposed on the geometry of the cylinder. This mode shape is obtained by performing a eigenvalue buckling analysis in Ansys which results in a deformed shell as depicted in Figure 5.8. The buckling mode shape does not represent actual displacements; they only visualise the deformation shape. Therefore, the deformed geometry from the eigenvalue analysis has to be scaled to represent appropriate imperfections. To impose the maximum size imperfections for each quality class, a scalingsfactor γ is used. In Equation 5.6, the depth of the dimples Δw_{0x} is scaled in order to satisfy the recommended values for $U_{0,max}$.

$$\gamma * \frac{\Delta w_{0x}}{l_{gx}} \leq U_{0,max} \tag{5.6}$$

Table 5.2: Recommended values for the dimple tolerance parameter $U_{0,max}$ (NEN, 2007)

Fabrication tolerance quality class	**Description**	**Recommended value of $U_{0,max}$**
Class A	Excellent	0.006
Class B	High	0.010
Class C	Normal	0.016

5.2. Validation

The validation of the model is done in steps. First, a static axial model will be validated by building it up step by step. Next, a static bending model and a dynamic axial model will be validated in order to make sure that the model works for dynamic bending. The FE model will be validated against analytical equations.

Building the model starts of with a Linear Analysis (LA), without any geometric or material non-linearities. Next, a Linear Bifurcation Analysis (LBA) is performed to get to the classical buckling equations as defined by Equation 2.2 and Equation 2.6. Then, geometrical non-linearities are added to the model (GNA) after which material non-linearity is added (GMNA). At last, imperfections are added to the geometry which will be validated Figure 2.6a and Figure 2.6b (Wang & Sadowski, 2020). In the following sections, this process will be followed for both static axial and bending analyses and results are validated. The cylinder used for model validation has a length $L = 8m$, radius $R = 2m$, thickness $h = 0.04m$, Young's modulus $E = 210GPa$, Poisson's ratio of $\nu = 0.3$ and (when applicable) a yield stress $\sigma_y = 346.9MPa$.

5.2.1. Static axial analysis

Linear Analysis

The LA is performed using a transient structural system without large deflections. The top of the model is displaced with $\delta = 0.2m$ while the bottom is simply supported. The force-displacement graph is shown in Figure 5.9a, the deformed cylinder is shown in Figure 5.9b. It is clear that there are no large deflections, which would likely express themselves in radial direction for shell structures.

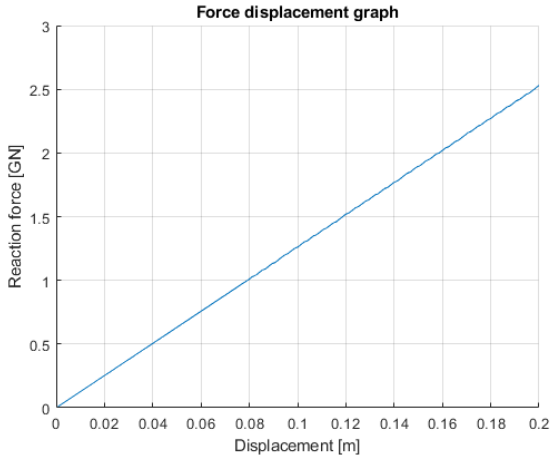

(a) Force displacement curve

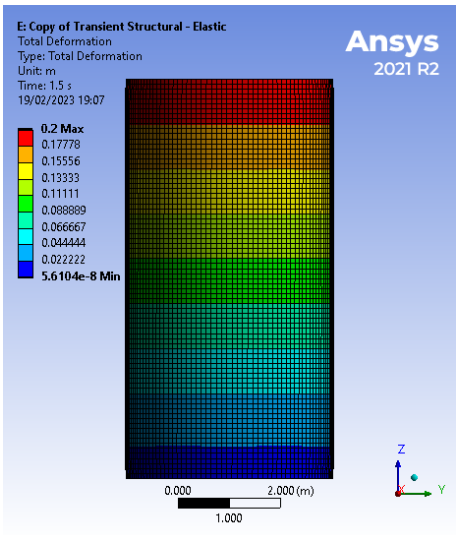

(b) Deformed shape

Figure 5.9: Linear analysis results from Ansys

The maximum force as given by the FE simulation is $F_{LA,FE} = 2.53GN$. The maximum force is also calculated analytically in Equation 4.17 to be $F_{LA,an} = 2.49GN$.

$$F = EA\frac{\Delta L}{L} = 2.49GN \tag{4.17}$$

Linear Bifurcation Analysis

The LBA is performed using an eigenvalue buckling analysis in Ansys. This analysis calculates the classical buckling force for each buckling mode. The first buckling mode will later be used to impose imperfections on the cylinder. The reaction force as calculated by Ansys is $F_{LBA,FE} = 1.20GN$, while Equation 2.2 gives $F_{LBA,an} = 1.22GN$.

Geometrical Nonlinear Analysis

The GNA is performed in Ansys using a transient structural system. Large deflections are included to take geometrical non-linearity into account, while a purely elastic material is used. The force-displacement graph is shown in Figure 5.10a.

The maximum resulting force is $F_{GNA} = 1.09GN$ is a bit smaller than F_{LBA} which is to be expected since geometrical non-linearities are taken into account in this analysis. Figure 5.11 shows the displacement curves of both LA and GNA. There is a clear buckling moment defined by the snap around $\Delta L = 0.87m$. The first part of the GNA is exactly the same as the LA, as expected. After the snap, the cylinder fails through radial deformation as shown in Figure 5.10b.

Geometrical and Material Nonlinear Analysis

A transient structural analysis is used for the GMNA, including large deflections and plasticity. The force displacement graph is shown in Figure 5.12a.

The cylinder buckles at the onset of plasticity at $F_{GMNA,FE} = 174MN$. Equation 5.7 shows that the same force is required to reach the yield stress. The buckling moment can be seen clearly just as for

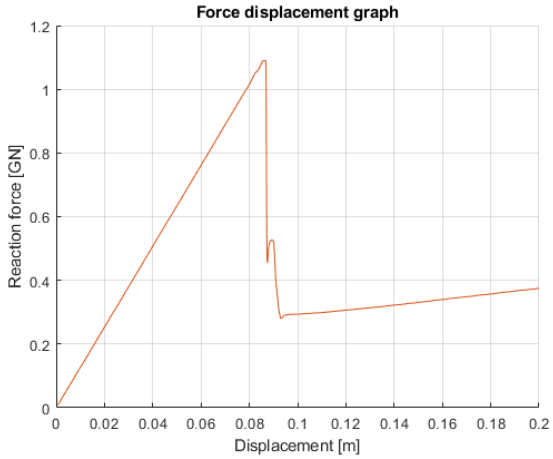

(a) Force displacement curve

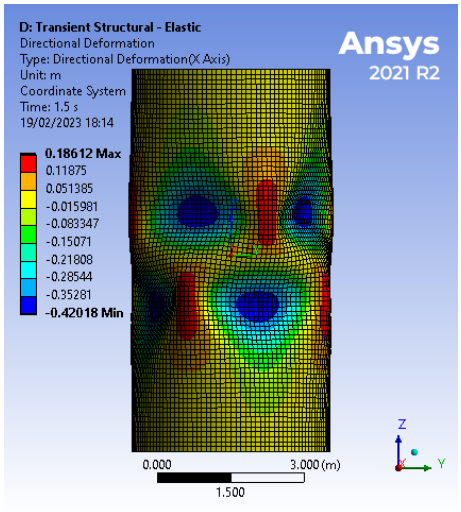

(b) Deformed shape (radial deformation)

Figure 5.10: Geometrically non-linear analysis results from Ansys

the GNA, although the post-buckling deformation is less extreme. This is to be expected since plasticity results in yielding of the material rather than a sudden extreme deformation.

$$N_p = A\sigma_y = 2\pi Rh\sigma_y = 174MN \tag{5.7}$$

Conclusion
Table 5.3 shows an overview of the results of the FE simulations and the analytical solutions. As is shown, the differences between both results for all analysis types are minimal. Therefore, it can be concluded that the static model under axial load works and is validated.

Table 5.3: Overview of the FE and analytical results for the static axial model

Analysis	FE	Analytical	Difference
LA	2.53 GN	2.49 GN	1.68%
LBA	1.20 GN	1.22 GN	1.41%
GNA	1.09 GN	-	-
GMNA	174 MN	174 MN*	0.21%

* Although Equation 5.7 is not an analytical GMNA solution, it is considered interesting to compare the plastic force to the GMNA to correlate plastic effects.

5.2.2. Static bending analysis

Linear Analysis
The LA is performed using a transient structural system without large deflections. Both ends of the model are displaced by rotating 5°. The moment-displacement graph is shown in Figure 5.13a; the deformed shape is shown in Figure 5.13b. Again, it is clear that there are no large deflections that would express themselves in the radial direction.

The maximum moment as given by the FE simulation is $M_{LA,FE} = 4.41GNm$. The maximum moment is also calculated analytically in Equation 4.23 to be $M_{LA,an} = 4.26GNm$.

$$M = \frac{EI}{L}\alpha = 4.26GNm \tag{4.23}$$

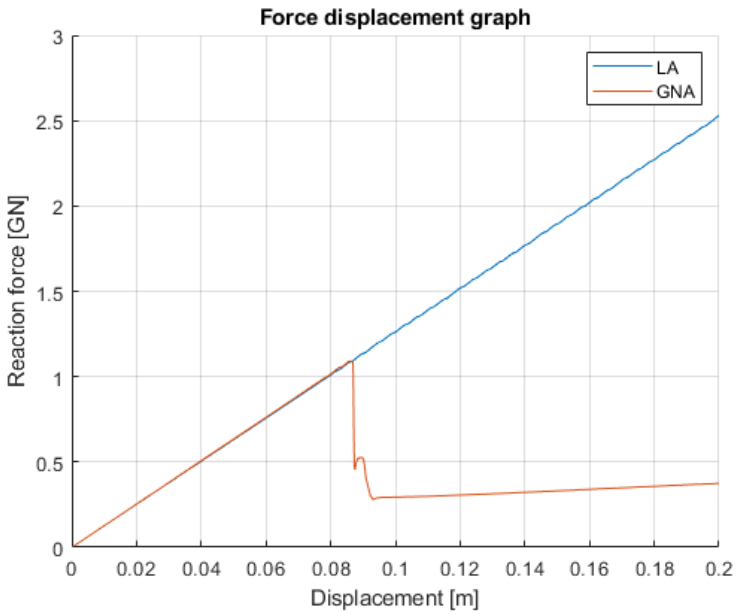

Figure 5.11: Linear and geometrically non-linear analysis - force displacement curve

Geometrical Nonlinear Analysis

The GNA is performed in Ansys using a transient structural system. Large deflections are included to take geometrical non-linearity into account, while an purely elastic material is used. The force-displacement graph is shown in Figure 5.14a.

The maximum resulting moment is $M_{GNA} = 1.22GNm$. Figure 5.15 shows the displacement curves of both LA and GNA. There is a clear buckling moment defined by the snap around $\alpha = 3°$. The first part of the GNA is exactly the same as the LA, as expected. After the snap, the cylinder fails through radial deformation as shown in Figure 5.14b.

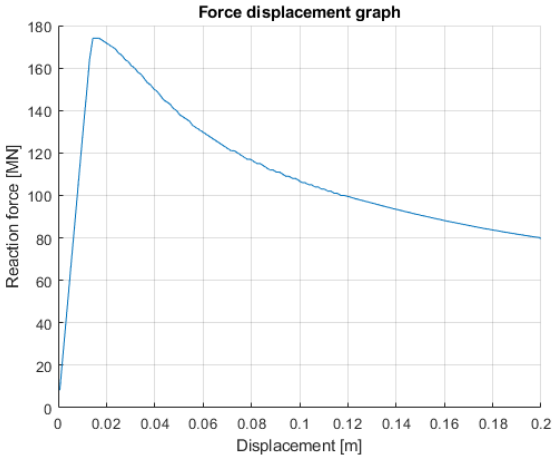

(a) Force displacement curve

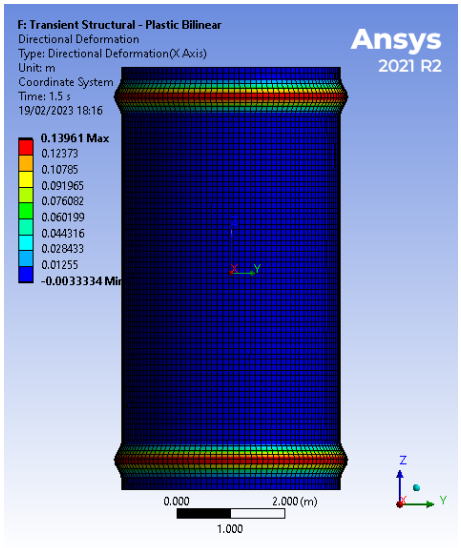

(b) Deformed shape (radial deformation)

Figure 5.12: Geometrically and material non-linear analysis results from Ansys

Geometrical and Material Nonlinear Analysis
A transient structural analysis is used for the GMNA, including large deflections and plasticity. The moment displacement graph is shown in Figure 5.12a.

The cylinder buckles at the onset of plasticity at $M_{GMNA,FE} = 214MN$. $M_p = 222MNm$ (Equation 2.9), which shows that roughly the same force is required to reach the yield stress. The buckling moment can be seen clearly just as for the GNA, although the post-buckling deformation is less extreme. This is to be expected since plasticity results in yielding of the material rather than a sudden extreme deformation.

Conclusion
Table 5.4 shows an overview of the results of the FE simulations and the analytical solutions. As is shown, the differences between both results for all analysis types are minimal. Also, the buckling modes of all analyses are as expected. Therefore, it can be concluded that the static model under bending load works and is validated.

Table 5.4: Overview of the FE and analytical results for the static bending model

Analysis	FE	Analytical	Difference
LA	4.41 GNm	4.26 GNm	3.52%
GNA	1.22 GNm	-	-
GMNA	214 MNm	222 MNm*	3.60%

* Although Equation 2.9 is not an analytical GMNA solution, it is considered interesting to compare the plastic moment to the GMNA to correlate plastic effects.

5.2.3. Dynamic axial analysis
The dynamic axial model is validated by comparing the results to the analytical model as described in chapter 4. The geometry is loaded with loading rates $250GN/s, 375GN/s,$ and $500GN/s$. Since the analytical model doesn't take material non-linearity into account, the cylinder is modelled purely elastically. The resulting K_d ratios can be seen in Figure 5.17. The results are also shown in Table 5.5 including the differences between the FE results and the analytical results. The models agree reasonably well with each other and show the same trend. However, it seems that the FE model underestimates the dynamic effects.

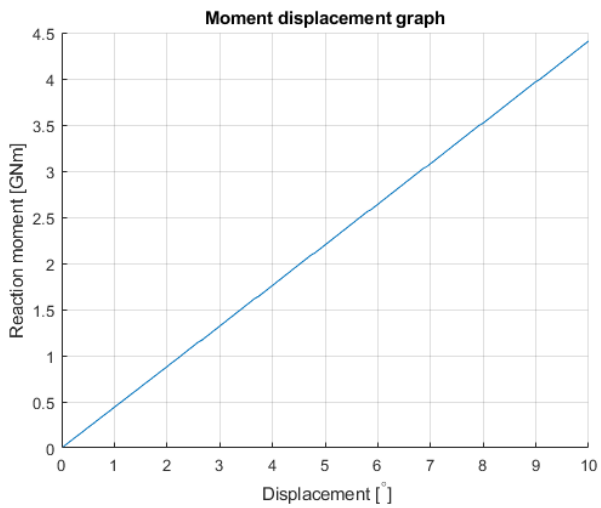

(a) LA - force displacement curve

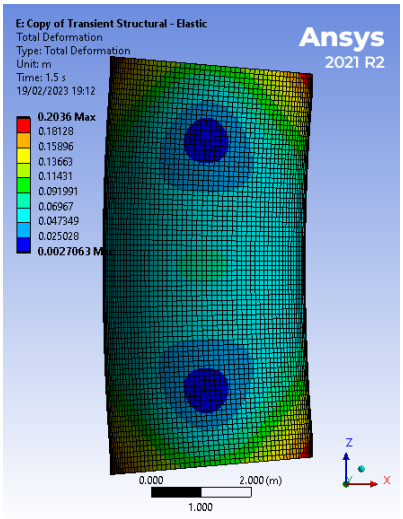

(b) Deformed shape

Figure 5.13: Linear analysis results from Ansys

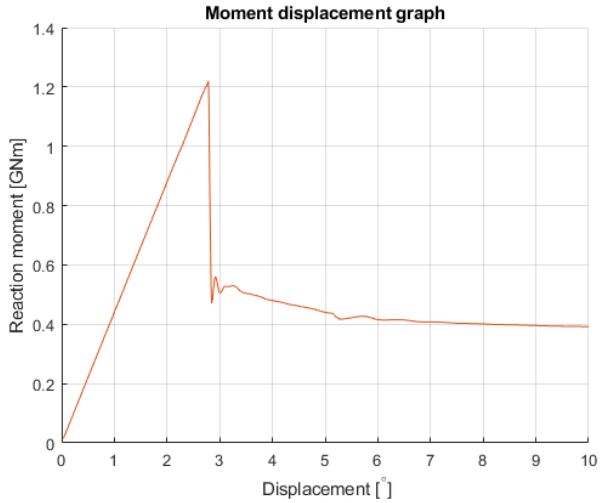

(a) Force displacement curve

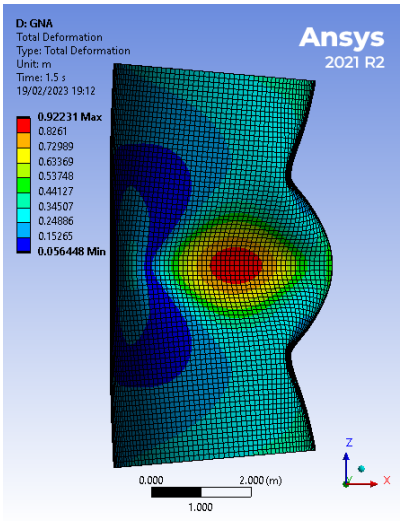

(b) Deformed shape

Figure 5.14: Geometrically nonlinear analysis results from Ansys

5.3. Parameters

In order to investigate the influence of different parameters on the dynamic bending buckling load, a parametric study is performed. The parameters of this study are chosen based on the measurements of current monopiles.

From the equations for the critical axial and bending buckling loads for shell structures, Equation 2.2 and Equation 2.6, it is clear that both are dependent on the material properties E and ν, and the geometrical properties R and h. The analytical model discussed in section 4.1 revealed that the dynamic axial critical buckling load is influenced by the loading rate and density of the material, besides the static parameters. By including the loading rate and density, inertia is taken into account. Wang and Sadowski showed that there are different length regimes which determine the buckling mode (2020). For slender cylinders with low cross sections with low values of moment of inertia, ovalisation buckling tends to be the preferred failure mode.

The material used in this study is chosen to be S355 steel since this is often used in the construction

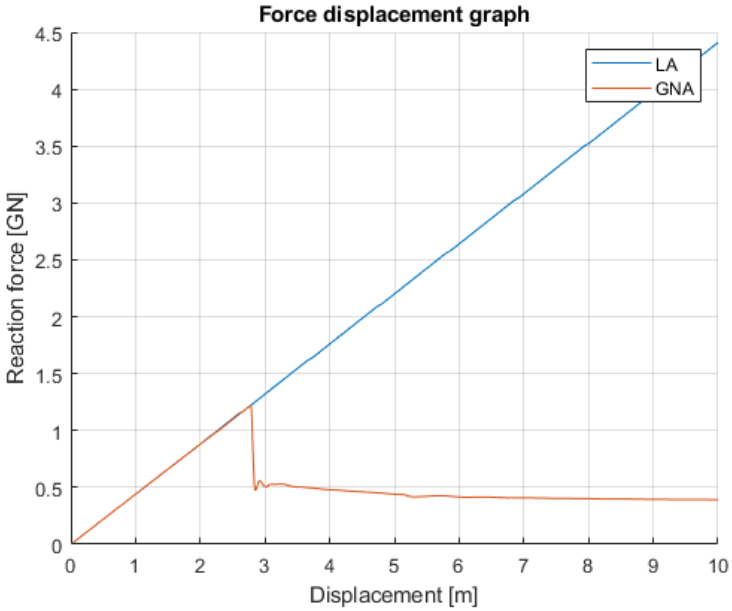

Figure 5.15: Linear and geometrically nonlinear analysis - moment displacement curve

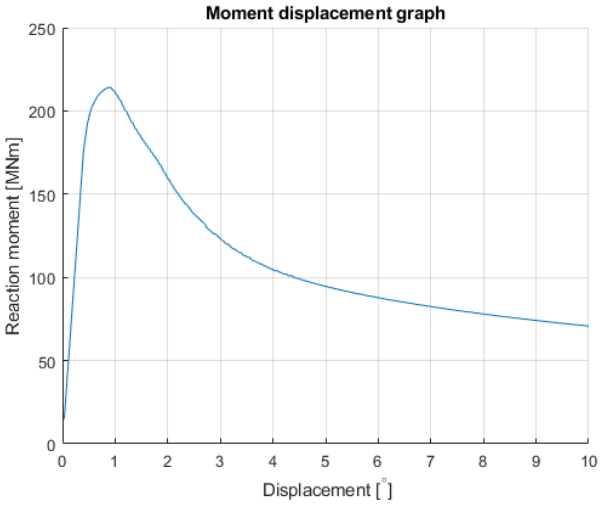

(a) Moment displacement curve

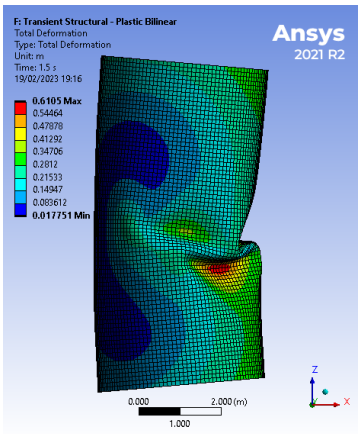

(b) Deformed shape

Figure 5.16: Geometrical and material nonlinear analysis results from Ansys

of monopiles. The material model is a bi-linear model as discussed in subsection 5.1.5; the yield stress, Poisson's ratio, and Young's modulus are $\sigma_y = 346.9MPa, \nu = 0.3, E = 210GPa$, respectively (DNV, 2013b).

The following parameters are varied in this study:

- Geometrical properties R and h;
- Loading rate $\dot{M}$;
- Imperfection ratio δ_0/h

5.3.1. Geometrical properties

The geometrical properties are based on dimensions of current monopiles. The ratios L/R and R/h are chosen as the leading figures, with values chosen as shown in Table 5.6. With these values,

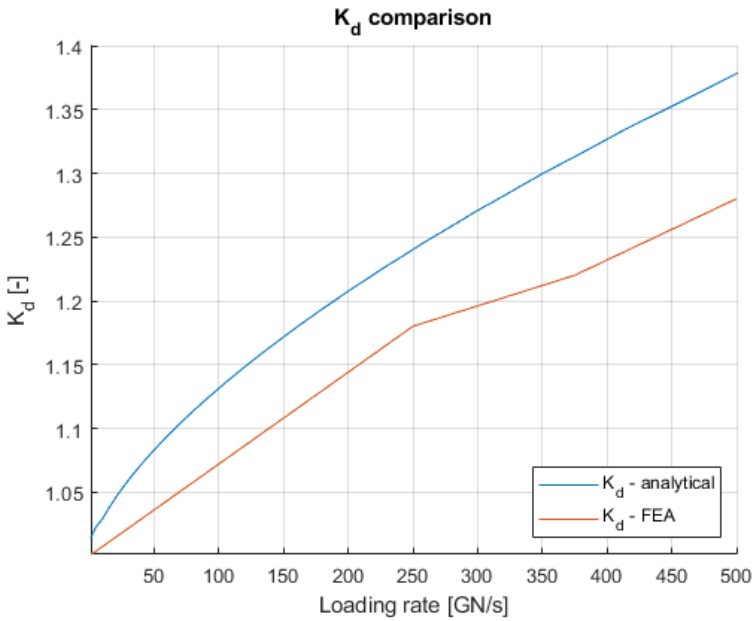

Figure 5.17: FE vs analytical model K_d comparison

Table 5.5: FE vs analytical model K_d comparison

$\dot{F}$ [GN/s]	$K_{d,FE}$ [-]	$K_{d,Analytical}$ [-]	Difference [%]
250	1.18	1.24	5.55
375	1.22	1.31	7.96
500	1.28	1.38	7.33

the geometries for the FEA fall in the non-dimensional length ranges of $\omega = [13.43; 56.92]$ and $\Omega = [0.32; 1.10]$ as defined by Equation 2.13 and Equation 2.14, respectively. An overview of these ranges is given in Figure 5.18. It can be seen that the geometries fall within the medium and transitional length ranges. This means that ovalisation buckling (at least for static cases) and local buckling (more likely for dynamic cases) can be expected.

The length of the cylinder is kept constant at $L = 8m$. By varying the ratios L/R and R/h, the different length regimes according to (Wang & Sadowski, 2020) are still investigated.

Table 5.6: Values for parametric study

	Values			
L/R	3	4	5	6
R/h	30	50	70	90

5.3.2. Loading rate

The loading rate is varied depending on the geometry of the cylinder and the simulation time. For the sake of automation of the simulations, five different simulation end times are chosen. As discussed in subsection 4.3.2, the loading rate depends on the geometric properties (inertia I and length L) of a cylinder and the rotation rate of the specimen.

Both ends of the cylinders are rotated by 5 degrees to induce buckling of the shell structures. The end times of the simulations are set in subsection 5.1.4 to be:

- 1.0 [s]
- 0.1 [s]
- 0.05 [s]
- 0.025 [s]

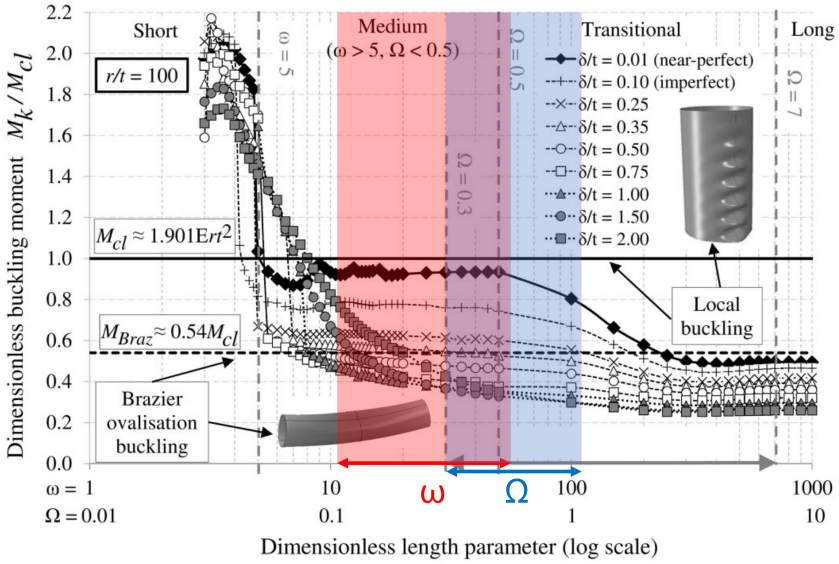

Figure 5.18: Ranges of non-dimensional length parameters ω and Ω from (Wang & Sadowski, 2020)

- 0.0125 [s]
- 0.00625 [s]

These end times ensure that the simulations are such that the dynamic effects are captured and present.

5.3.3. Imperfections

Imperfections have a significant influence on the buckling capacity of cylindrical shells. The way in which these imperfections are measured and applied is discussed in subsection 5.1.6. For this research, imperfection class C as depicted in Table 5.2 is applied to the geometry of the cylinders. The largest imperfection class is chosen in order for the effects to be most evident.

6

Results

This chapter will discuss the results from the FEA as described in chapter 5.

6.1. Analysis of results

First, the process of selecting the critical buckling point is discussed. Then the choice of dimensionless parameters is clarified. These parameters are used later on to compare different geometries and results. First, perfect shells with no imperfections are reviewed. Then, the imperfect shells will be shown to investigate the influence of imperfections.

6.1.1. Critical buckling point

The critical buckling point of each analysis is determined by analysing both the moment measured at either the top or the bottom of the cylinder and the deformation of the cylinder over time. As briefly discussed in subsection 5.1.4, the load profile is adjusted in order to minimise extremes due to infinite accelerations. However, the load profile has still been discretised and thus high values during the ramp up of the loading rate still occur in some cases. To make sure that these maxima are not depicting the critical buckling moment, a visual inspection of the cylinder deformation for each analysis has been carried out as well. The resulting graphs with the buckling point indicated are shown in Appendix A.

6.1.2. Dimensionless parameters

Dimensionless length parameters are used to compare the different geometries to each other. Based on Wang and Sadowski (2020), it is expected for the different cylinders to react differently based on their dimensionless lengths ω and Ω, as discussed in chapter 2. Their paper discussed that based on the dimensionless length of a cylindrical shell, the shell would buckle in a different shape and have a different sensitivity to imperfections. Since this thesis varies geometrical parameters including imperfections, a comparison can be made based on these dimensionless parameters. Also, the relative thickness, R/h, is used to compare the cylindrical shells. By looking back at Equation 2.5, it is clear that the critical buckling stress for a cylindrical shell only depends on the ratio h/R, when material properties are omitted (in this research, they are kept constant and so no comparison based thereon is possible). At last, the dimensionless parameter $\bar{F}$ is used to compare the different geometries as well in terms of dynamic load factor.

6.2. Influence of geometrical properties

This section discusses the influence of the geometrical ratio R/h, and the dimensionless length parameters Ω and ω on the dynamic buckling capacity of cylindrical shells.

6.2.1. Influence of dimensionless radius and thickness

The influence of the radius and thickness on the dynamic bending buckling capacity is discussed in this section. For this, the ratios L/R and R/h are examined in this section. As discussed in subsection 5.3.1

the geometric ratios have been varied according to Table 5.6. Figure 6.1 shows the resulting K_d-graphs according to these variations for cylinders with no imperfections (Impf = 0) The range in loading rate per L/R varies significantly. This can be explained by looking at Equation 4.23, since the loading rate is only dependent on the moment of inertia I because the length L and the Young's modulus E are kept constant in this research. The radius R (and therefore ratio L/R) has significant influence on the order of the moment of inertia and therefore on the order of the loading rate.

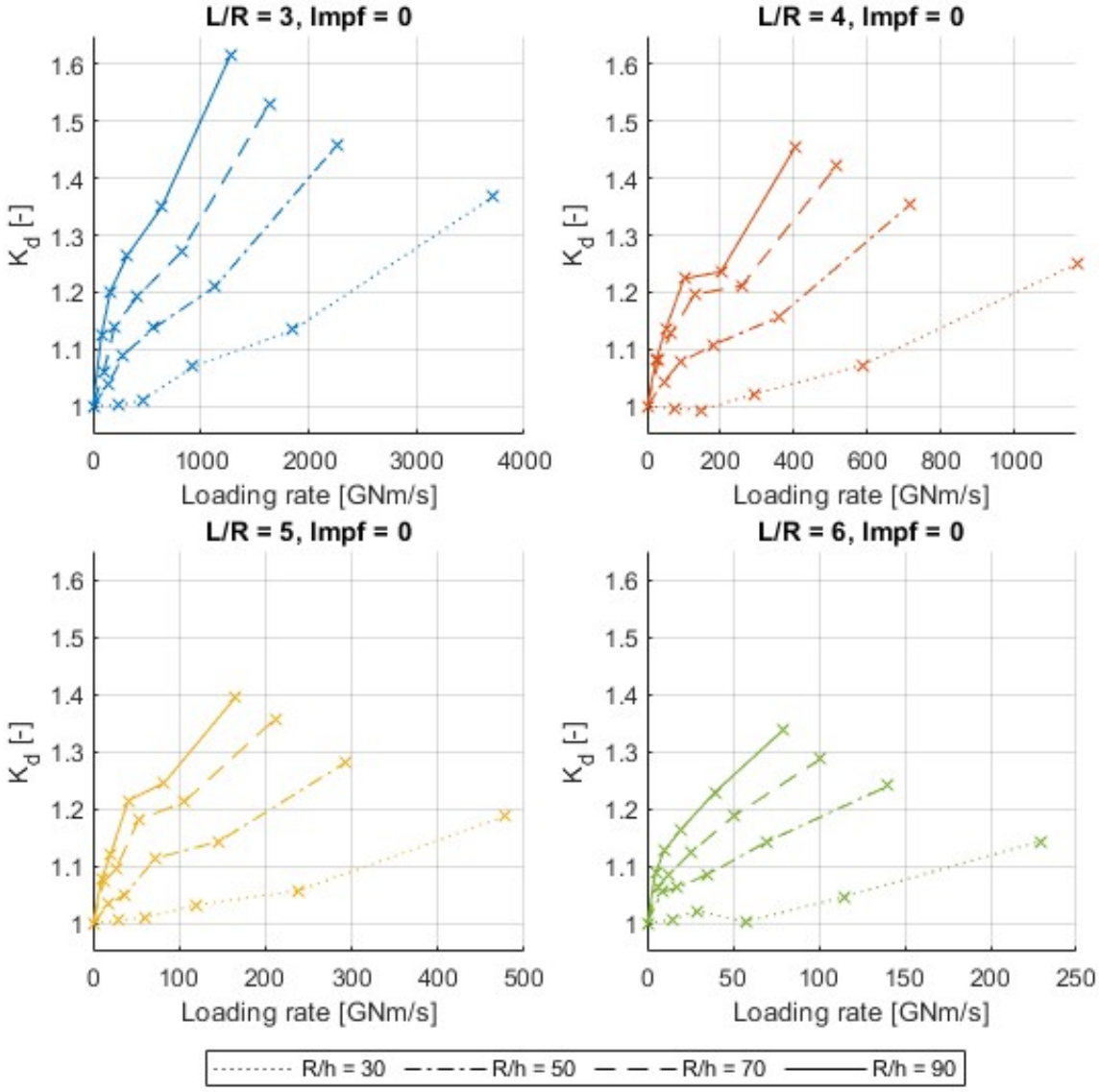

Figure 6.1: K_d-graphs for different L/R and R/h ratios

For a comparison between the different L/R ratios, the loading rate is normalised by dividing it by the moment of inertia for each cylinder. The results are shown in Figure 6.2

Two things can be observed by looking at the graphs in Figure 6.2. A decrease in L/R correlates to an increase in K_d, and an increase in R/h correlates to an increase in K_d. This is also in line with the parametric study regarding the model of Sofiyev for axial dynamic buckling conducted in section 4.2.

Table 6.1 shows the relative plasticity for each R/h value. Relative plasticity is here defined as the quasi-static critical buckling moment M_{QS} divided by the full plastic moment M_p. It basically shows for how much the plastic moment has been reached in the cylinder. It is evident that there is correlation between the ratio R/h and the amount of plasticity occurring in the cylinders, which makes sense

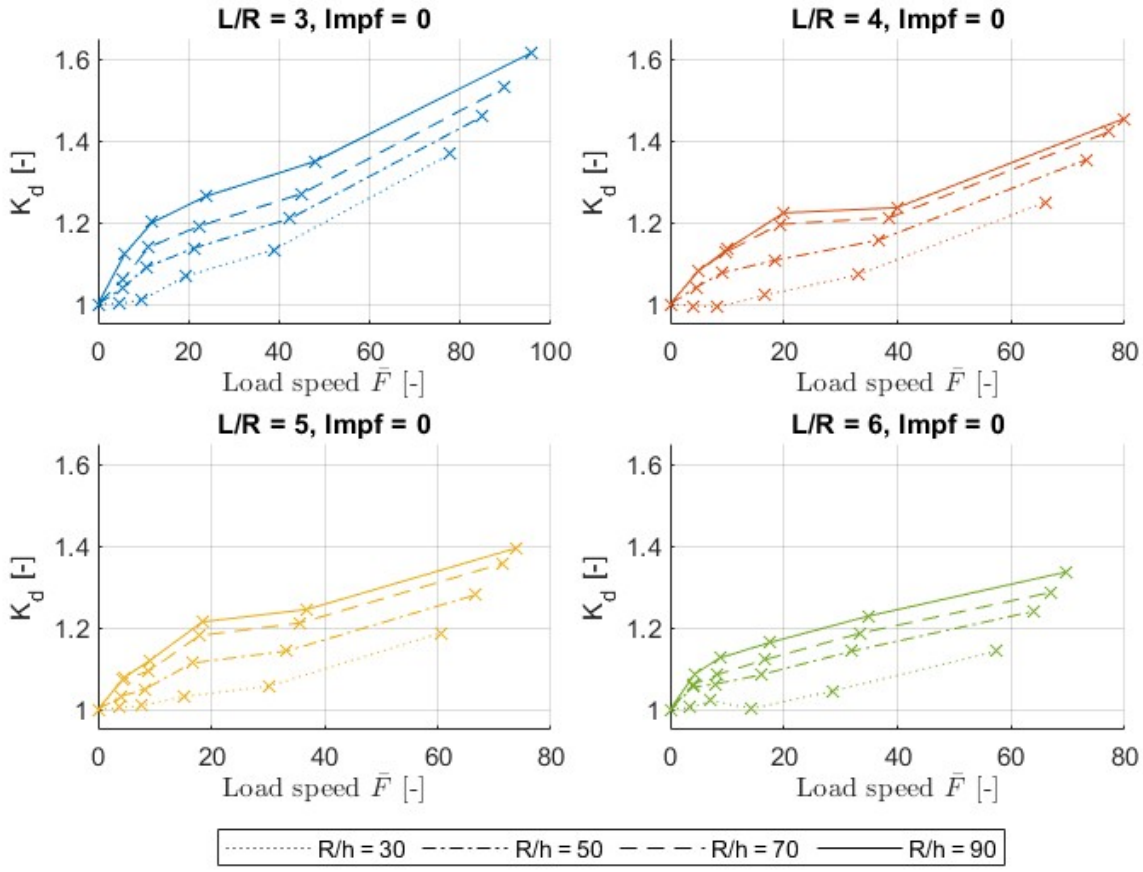

Figure 6.2: Normalised K_d-graphs for different R/h ratios per L/R

looking back at Equation 2.9. It seems that lower R/h-values correspond to a higher degree of plasticity during the loading process. This is supported by looking at the buckling moment vs time graphs of the cylinders, see for example Figure 6.3. There is a clear plateau leading up to the critical buckling moment which is typical for plasticity. Reference is made to Appendix A for a complete overview of all load graphs.

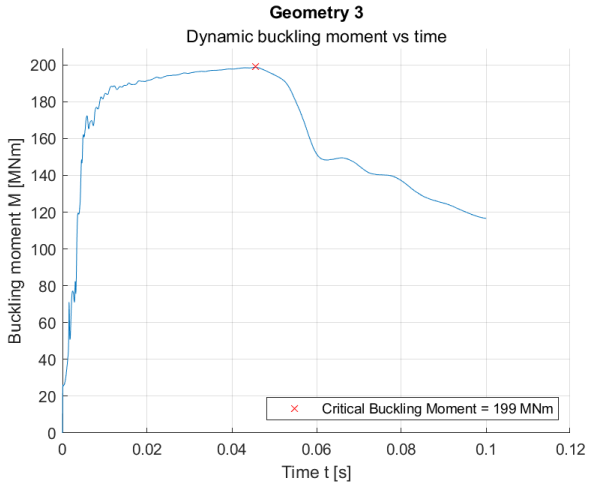

Figure 6.3: Dynamic buckling moment vs time - geometry 3

Table 6.1: Relative plasticity per R/h-value for all geometries

# [-]	R [m]	h [m]	R/h [-]	M_{QS}/M_p [-]
1	2.67	0.0889	30	1.04
2	2.00	0.0667	30	1.05
3	1.60	0.0533	30	1.05
4	1.33	0.0444	30	1.04
5	2.67	0.0533	50	0.98
6	2.00	0.0400	50	0.97
7	1.60	0.0320	50	0.97
8	1.33	0.0267	50	0.95
9	2.67	0.0381	70	0.93
10	2.00	0.0286	70	0.92
11	1.60	0.0229	70	0.91
12	1.33	0.0190	70	0.92
13	2.67	0.0296	90	0.88
14	2.00	0.0222	90	0.90
15	1.60	0.0178	90	0.89
16	1.33	0.0148	90	0.89

6.2.2. Influence of dimensionless length on dynamic load factor

The dimensionless length of the cylinder influences the buckling shape and sensitivity to imperfections as Wang and Sadowski concluded for static buckling (2020). The influence of the dimensionless length on the dynamic load factor will be discussed in this section.

The dimensionless length parameter Ω is used to categorise cylinders according to their length. The (elastic) buckling strength of short, stocky cylinders is relatively high in comparison to the classical buckling equation (Equation 2.6) and experiences greater influence of the boundary conditions; these cylinders have low ω-values. Long, slender cylinders have relatively low buckling strengths in comparison to the classical buckling strength due to less influence of boundary conditions and the ovalisation of the cylinder, these correspond to higher ω-values. Ω is calculated by multiplying ω by the ratio h/R, and so focuses more on the relative thickness. Next, as discussed in section 2.4, the slenderness of a cylinder determines whether the cylinder exhibits plastic behaviour before buckling. Stocky cylinders tend to exhibit plastic behaviour before buckling.

Figure 6.4 shows the K_d-values per cylinder sorted using the dimensionless length Ω. There is a clear downward trend towards higher Ω-values (with large L/R and small R/h values). It seems that there is a correlation on sensitivity to dynamic loading for relatively thick stocky versus slender cylinders. The clear trend in Figure 6.4a and Figure 6.4b can be explained by looking back at Equation 2.14 and Figure 4.3. It was already concluded that for axial load cases, a smaller L/R ratio (and thus larger radii) corresponds to a larger K_d. Larger radii also correspond to a smaller Ω value. Therefore, it could be expected that smaller Ω correspond to larger K_d values, when the comparison is made between bending and axial load cases.

6.2.3. Influence of dimensionless length on buckling shape

The dimensionless length influences the buckling shape of cylindrical shell structures, as has been proved by Wang and Sadowski for both axial and bending buckling of cylindrical shells (2020). As mentioned in section 2.2, for axial buckling, dynamic loads cause buckliing to occur close to the ends of the specimen. This can also be seen for dynamic bending buckling. Figure 6.5 shows the side view for six simulations for the same geometry at increasing load speed. It is clear that the buckle moves to the outer ends of the specimen as the load speed increases.

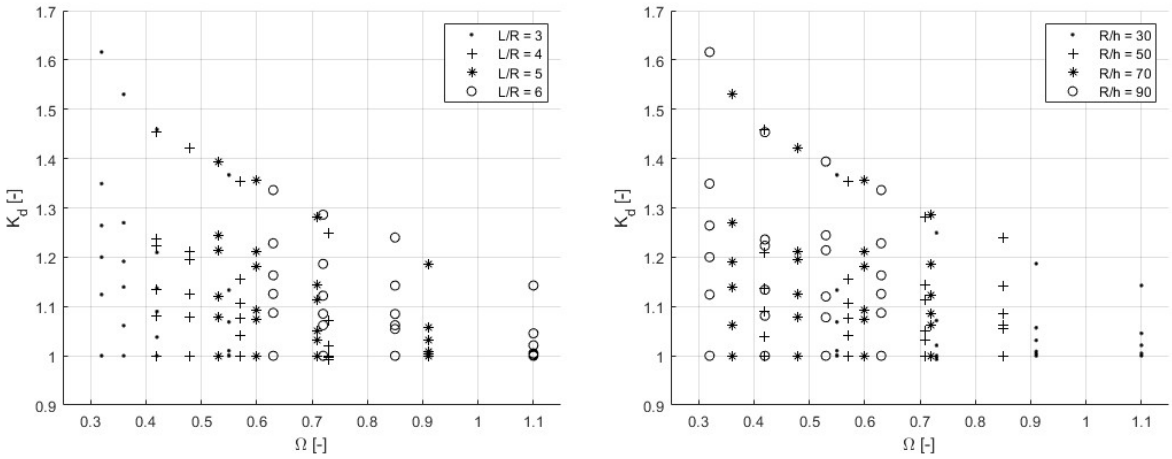

(a) Grouped per L/R ratio

(b) Grouped per R/h ratio

Figure 6.4: Influence of dimensionless length Ω vs K_d

6.3. Influence of imperfections

The influence of imperfections on static buckling can be significant. However, shells are more sensitive to imperfections for static loads than for dynamic loads as described in section 2.5. For static loads, it was also noted in section 2.5 that higher dimensionless lengths of cylindrical shells correlate to less imperfection sensitivity. Next, imperfections could influence the shape in which a specimen buckles since it is likely that the buckling starts at imperfections and grows from there on.

The above mentioned points will be discussed briefly in this section.

6.3.1. Imperfection sensitivity on DLF

Figure 6.6 shows the K_d-graphs for imperfect shells for different geometrical ratios, just as in Figure 6.2. The graphs for the perfect shells are indicated in grey for comparison. It is noticeable that the difference between the two sets of data (imperfect vs. perfect) decreases as the loading becomes more dynamic. This is in line with dynamic axial loading of cylindrical shells.

6.3.2. Influence of dimensionless length

The influence of imperfections on the dynamic load factor for varying dimensionless lengths is investigated in this section. Figure 6.7 shows a table of the relative difference between the dynamic load factors of perfect cylindrical shells versus imperfect cylindrical shells. The table is ordered regarding the dimensionless length parameter Ω.

It is clear that for higher values of Ω, the influence of imperfections decreases since the difference between the dynamic load factors decreases. Also, for increasingly dynamic loads (shorter simulation end times) the influence of imperfections decrease as well.

Both observations are in line with existing research on (static) buckling of cylindrical shells. According to Wang and Sadowski, there is a lower imperfection sensitivity for (dimensionless) longer shells (2020). Zaczynska et al. concluded that shells with larger imperfections are less sensitive to dynamic loading (2020).

6.3.3. Influence on buckling shape

The influence of imperfections on the buckled shape of cylindrical shells is quite obvious for static buckling. As discussed in chapter 2, the imperfections are eccentricities from which buckles will start to grow. This is also the case for dynamic loading.

Figure 6.8 shows the side views for the buckled cylindrical shells for a (somewhat) dynamic load. It clearly shows a diamond-shaped pattern on the side of the imperfect shell that is in compression. In

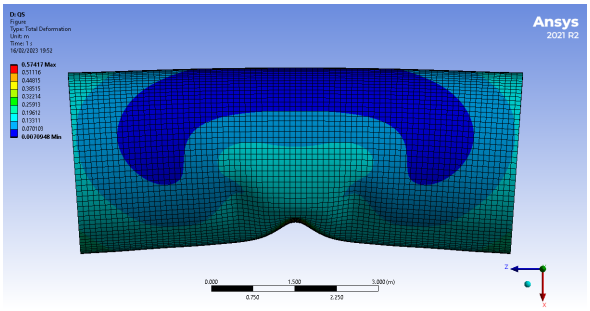

(a) Quasi static buckling

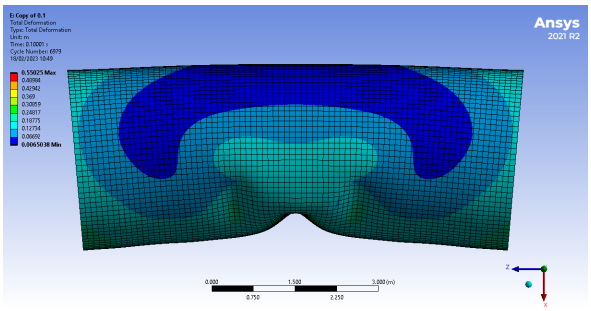

(b) Dynamic buckling $t_{end} = 0.1s$

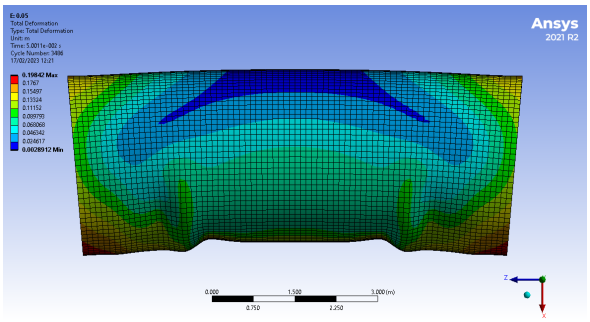

(c) Dynamic buckling $t_{end} = 0.05s$

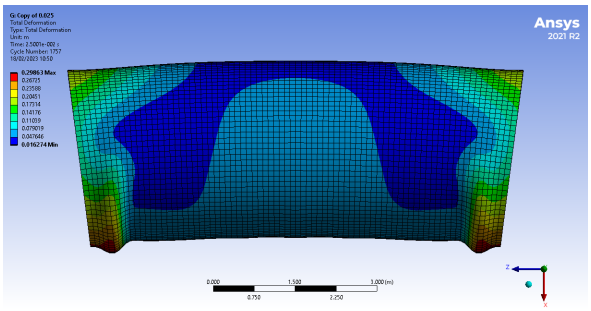

(d) Dynamic buckling $t_{end} = 0.025s$

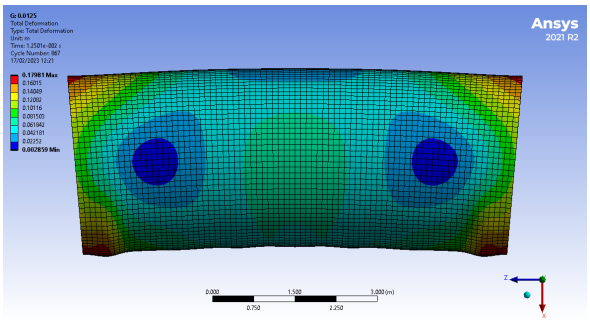

(e) Dynamic buckling $t_{end} = 0.0125s$

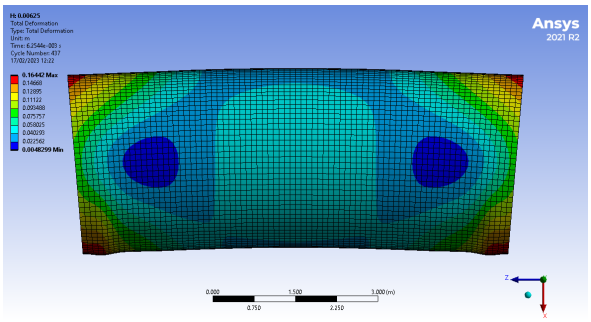

(f) Dynamic buckling $t_{end} = 0.00625s$

Figure 6.5: Side view of buckled cylindrical shells at different load speeds

comparison to the shape of the perfect cylinder, the imperfect shell has not buckled near the ends of the shell.

As the load becomes more dynamic, it seems that the influence of imperfections starts to fade. Figure 6.9 shows a side view of the same cylindrical shell subjected to a higher loading rate. The buckles on the compressed side of the shell are less defined compared to the buckles of the imperfect shell in Figure 6.8. The dimples are also spread out more evenly over the length of the cylinder. Two clear buckles have formed near both ends of the shell, ensuring a greater resemblance to the perfect shell. It looks like the influence of the imperfections at higher loading rates becomes less, as was also seen in the dynamic load factors as discussed in subsection 6.3.1.

The decreasing influence of imperfections continues for higher loading rates as shown in Figure 6.10. The perfect and imperfect post-buckling shapes of two different cylinders are shown. It is clear that the imperfect and perfect cylinders start to resemble each other more for increasing loading rates. However, the level of resemblance depends on the type of cylinder. The stocky cylinders in Figure 6.10a and Figure 6.10b show greater differences to each other than the slender cylinders in Figure 6.10c and Figure 6.10d.

It seems that the level of influence of imperfections on the post-buckling shape of cylindrical shells

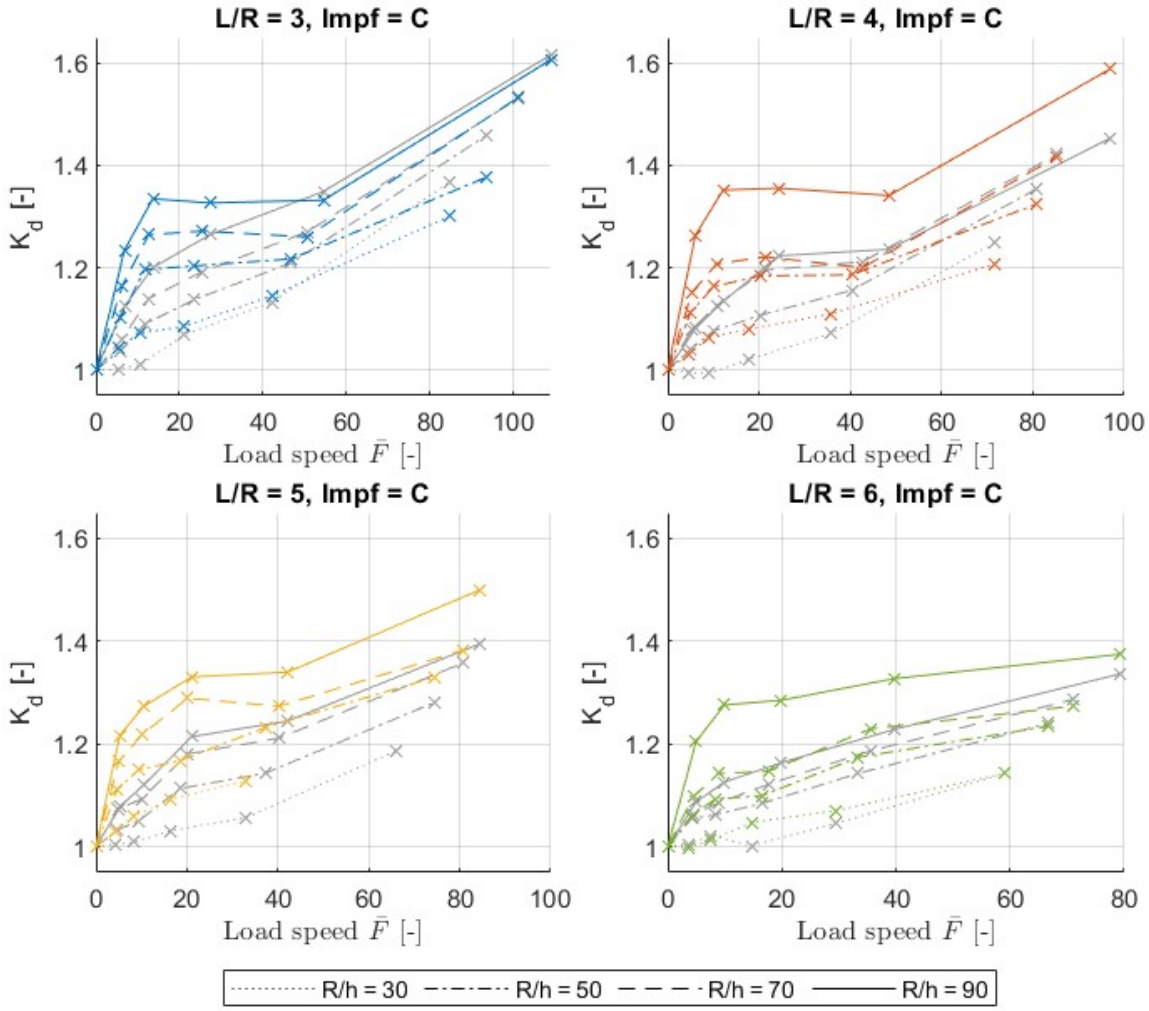

Figure 6.6: Normalised K_d-graphs for different R/h ratios per L/R for imperfect shells, the K_D-graphs for perfect shells are shown in grey.

depends on the dimensionless length of the cylinder and the magnitude of the loading rate. The influence of imperfections becomes less for higher loading rates and more slender cylindrical shells.

Ω	0.1	0.05	0.025	0.0125	0.00625
0.316228	9.79%	11.22%	4.95%	1.26%	0.60%
0.358569	9.78%	10.96%	6.73%	0.75%	0.13%
0.421637	16.86%	19.23%	10.81%	8.52%	9.32%
0.424264	6.29%	9.78%	5.85%	0.63%	5.61%
0.478091	6.71%	7.20%	2.16%	0.94%	0.33%
0.527046	12.89%	13.68%	9.58%	7.64%	7.54%
0.547723	4.14%	6.12%	1.56%	1.08%	4.87%
0.565685	6.93%	8.04%	6.99%	2.59%	2.16%
0.597614	8.57%	11.40%	9.18%	5.12%	1.83%
0.632456	10.77%	13.35%	10.46%	8.05%	2.87%
0.707107	7.58%	9.51%	4.87%	7.79%	3.84%
0.717137	3.25%	5.26%	2.23%	3.60%	0.99%
0.730297	3.45%	7.18%	5.74%	3.60%	3.38%
0.848528	0.57%	2.87%	1.38%	2.75%	0.44%
0.912871	2.46%	5.02%	5.90%	6.76%	
1.095445	0.60%	0.93%	4.51%	2.39%	0.03%

Figure 6.7: Table showing the absolute difference between the dynamic load factor of perfect and imperfect cylindrical shells. Green background indicates low values, red background indicated high values.

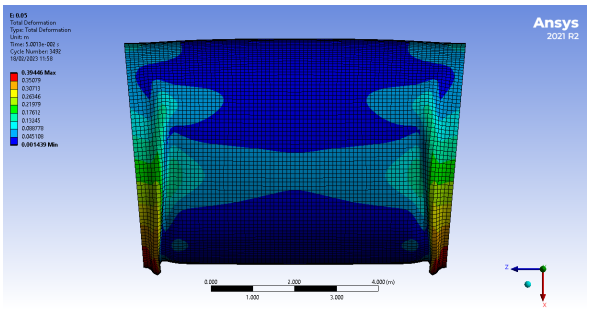

(a) Post-buckling shape of *perfect* cylindrical shell

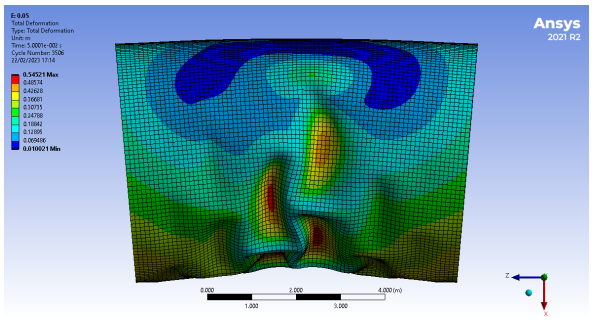

(b) Post-buckling shape of *imperfect* cylindrical shell

Figure 6.8: Side view of buckled cylindrical shells with $t_{end} = 0.05s$ (geometry 13)

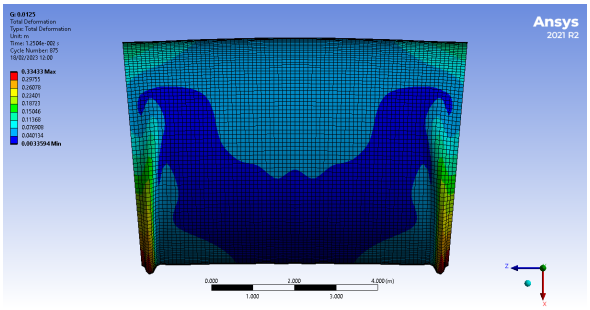

(a) Post-buckling shape of *perfect* cylindrical shell

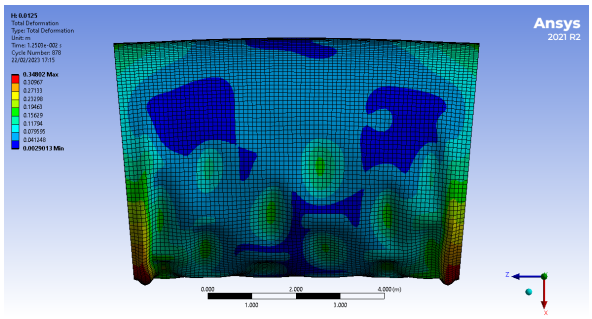

(b) Post-buckling shape of *imperfect* cylindrical shell

Figure 6.9: Side view of buckled cylindrical shells with $t_{end} = 0.0125s$ (geometry 13)

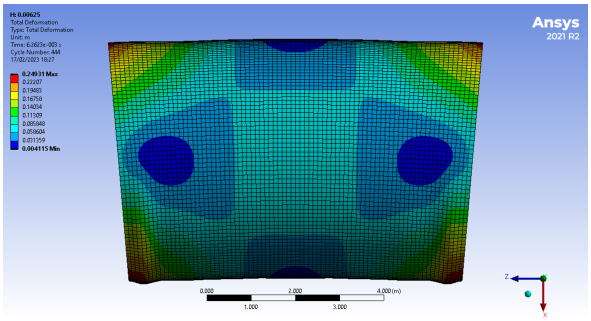

(a) Post-buckling shape of *perfect* cylindrical shell (geometry 5)

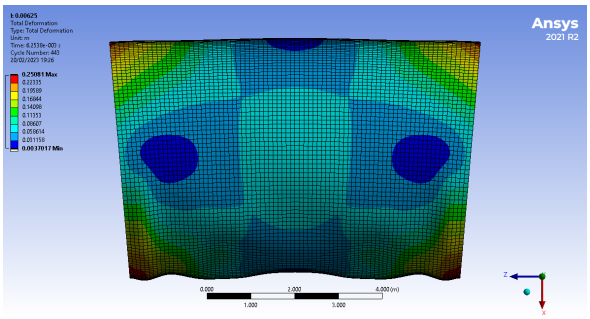

(b) Post-buckling shape of *imperfect* cylindrical shell (geometry 5)

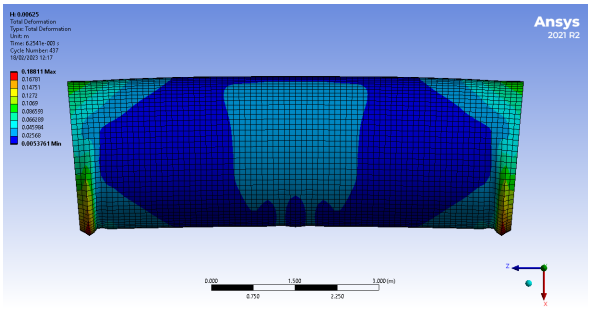

(c) Post-buckling shape of *perfect* cylindrical shell (geometry 16)

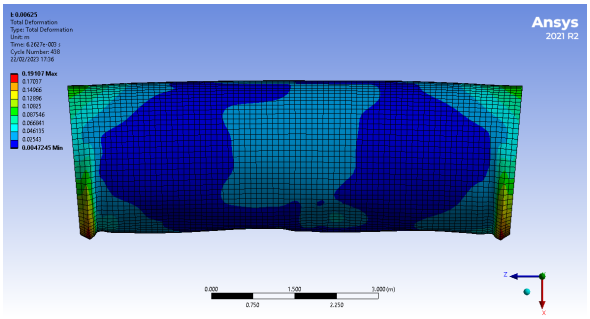

(d) Post-buckling shape of *imperfect* cylindrical shell (geometry 16)

Figure 6.10: Side view of buckled cylindrical shells with $t_{end} = 0.00625s$

7

Conclusion, Discussion and Recommendations

This chapter reviews the obtained results to give a conclusion. Furthermore, parts of this research are discussed briefly and recommendations for further research are made.

7.1. Conclusion

This section will answer the research main question using its sub questions as defined in chapter 1. The results from chapter 4 and chapter 6 will be summarised and looked back upon.

Which parameters influence the dynamic buckling capacity of cylindrical shells?
Looking back at the model of Sofiyev for dynamic axial buckling, the parameters that influence the dynamic buckling capacity of cylindrical shells are geometric, material, and load parameters (2005). The geometric parameters radius R and wall thickness h play an important role, larger R/h ratios correspond to larger K_d ratios. For dynamic bending buckling, the same principle applies. Larger R/h ratios correspond to larger dynamic load factors as was shown in subsection 6.2.1. The natural frequency, f_n, might have some influence on the buckling capacity as well. However, since the natural frequencies of the analysed geometries are correlate heavily with the L/R ratio, it is still uncertain what influence the natural frequency or the radius of the cylinder exactly has.

The length of a cylinder also affects the dynamic bending buckling capacity of cylindrical shells, as was shown in subsection 6.2.2. Stocky cylinders with low dimensionless length parameters Ω are more sensitive to dynamic loading and will have higher K_d values for the same loading rate as slender cylinders with high values of Ω.

In general, imperfections have a large influence on the buckling capacity of shell structures as well. This is also true for cylindrical shell structures subjected to dynamic bending buckling, as shown in section 6.3. Larger imperfections will result in a decreasing buckling capacity of cylindrical shells. However, for higher loading rates, this effect will decrease. This is also evident in the post-buckling shape of cylinders as shown in subsection 6.3.3, since for higher loading rates the effect of initial imperfections seems to decrease as the resemblance to perfect shells increases.

Material parameters also affect the buckling capacity of shell structures. The elastic model of Sofiyev showed that the Young's modules E, Poisson's ratio ν, and the density ρ play part in the final capacity of a cylinder. This thesis took plasticity into account as well and even though the yield stress σ_y was not varied, it is clear that this affects the capacity. subsection 6.2.1 showed that short, stocky cylinders have a tendency to reach their plastic moment and fail through yielding of the material. This is also true for higher loading rates.

What is the dynamic buckling capacity of a cylindrical shell subjected to bending, resembling the characteristics of a monopile?
The dynamic buckling capacity of cylindrical shells has been investigated and graphs for dynamic load factors versus loading rate are shown throughout chapter 6 for both perfect and imperfect shells. Although an exact model to describe this and estimate the effect of the dynamic plastic buckling capacity has not been developed, it can be concluded that the same parameters influence the buckling capacity of axial and bending dynamic buckling. The influences of these parameters are the same, as in that an increasing R/h corresponds to increasing K_d. However, the (dimensionless) length of a cylinder has a greater influence on the dynamic buckling capacity for bending buckling compared to axial buckling. Shorter, stocky cylinders have the tendency to reach higher dynamic load factors and thus are more capable of resisting dynamic loads.

The main research question can be answered based on the above.

What is the influence of loading rate on the dynamic buckling capacity of monopiles subjected to bending moments?

- Higher loading rates correspond to higher dynamic load factors K_d;
- Larger R/h ratios correspond to higher dynamic load factors K_d;
- Cylinders with larger dimensionless lengths Ω correspond to lower dynamic load factors K_d;
- Imperfections decrease the buckling capacity of cylindrical shells; however this effect decreases for increasing loading rates;
- Stocky cylinders are prone to yielding failure, also when subjected to dynamic loads.

Current technology improves increasingly fast and so does the design and size of monopiles. Above (qualitative) conclusion might help in the design of monopiles in the future.

7.2. Discussion

Some discussion of the results is necessary since certain aspects were neglected or results could be improved.

First of all, the strain rate as discussed in section 2.4 has been neglected in this study. Essentially, this means that the yield stress increases for higher loading rates. Therefore, it is expected that the dynamic load factors K_d would increase even more for increasing loading rates.

Secondly, a bi-linear material model has been adopted in this research. This was done in order to estimate the loading rate throughout the simulation. This estimated loading rate was considered as homogeneous over the cylinder. The stress-strain curves of S-grade steel, as used often in offshore structures, have a Lüders plateau. This means that already at low strains, the tangent modulus is relative flat. In this research a tangent modulus of E/100 is adopted, which can be seen as approximately flat. Although these assumptions were considered fair, the model has some discrepancies with the reality. More experience and expertise regarding the use of finite element software could decrease these discrepancies.

Next, this research implemented the imperfection shape by imposing the LBA mode from the axial case onto the cylindrical model. Other imperfection models, such as a LBA mode of a bending case or multiple modes imposed simultaneously, might give different results and an improved representation of reality.

Finally, even though efforts were made to minimise the effects of the acceleration of the rotation of the ends of the cylinders, some effect was still noticeable. As for the above, more experience and expertise regarding FEM could prove valuable for more accurate results.

7.3. Recommendations

In this thesis, a couple of obvious parameters or situations are neglected due to various reasons. Further research into the below is still recommended.

- Investigate the effects of different material properties such as yield stress.
- Investigate monopile-like characteristics like conical sections and (stepwise) variable thickness.
- Look at surrounding material for monopiles such as fluids and/or solids. Since monopiles are mostly submerged and embedded into the seabed, this has a great influence on the capacity.
- Investigate interaction between all of the above using a comprehensive model.
- Investigate more load cases that pure bending. This thesis disregarded other load factors due to various reasons. In reality, environmental conditions will load monopiles in various ways and not just pure bending. It is recommended that the interaction between these different forces is investigated.

Bibliography

Aksogan, O., & Sofiyev, A. (2002). Dynamic buckling of a cylindrical shell with variable thickness subject to a time-dependent external pressure varying as a power function of time. *Journal of Sound and Vibration*, *254*(4), 693–702. https://doi.org/10.1006/jsvi.2001.4115

ANSYS, I. (2021). *Ansys workbench* (Version R2.1) [Computer software].

ANSYS, Inc. (2011). *Ansys mechanical apdl element reference*.

ANSYS, Inc. (2021). *Ansys mechanical user's guide*.

Axelrad, E. (1985). On local buckling of thin shells. *International Journal of Non-Linear Mechanics*, *20*(4), 249–259. https://doi.org/https://doi.org/10.1016/0020-7462(85)90033-2

Chen, L., Peng, Y., & Wan, L. (2012). Nonlinear buckling behaviour of imperfect cylindrical shells under global bending in the elastic-plastic range. *Applied Mechanics and Materials*, *204-208*, 1045–1052. https://doi.org/10.4028/www.scientific.net/AMM.204-208.1045

Chen, Z., Yang, L., Cao, G., & Guo, W. (2012). Buckling of the axially compressed cylindrical shells with arbitrary axisymmetric thickness variation. *Thin-Walled Structures*, *60*, 38–45. https://doi.org/https://doi.org/10.1016/j.tws.2012.07.015

DNV. (2010). Buckling strength of shells [DNV-RP-C202].

DNV. (2013a). Design of offshore wind turbine structures [DNV-OS-J101].

DNV. (2013b). Determination of structural capacity by non-linear fe analysis methods [DNV-RP-C208].

DNVGL. (2016). Support structures for wind turbines [DNVGL-ST-0126].

Ellinas, C. P., Supple, W. J., Walker, A. C., & J.P. Kenny and Partners Ltd. (1984). *Buckling of offshore structures: A state of the art-review of the buckling of offshore structures* (1st). Granada Publishing.

European Commission. (2020). *Communication from the commission to the european parliament, the council, the european economic and social committee and the committee of the regions: Stepping up europe's 2030 climate ambition* [Investing in a climate-neutral future for the benefit of our people]. EUR-Lex.

Evkin, A., Krasovsky, V., Lykhachova, O., & Marchenko, V. (2019). Local buckling of axially compressed cylindrical shells with different boundary conditions. *Thin-Walled Structures*, *141*, 374–388. https://doi.org/10.1016/j.tws.2019.04.039

Fajuyitan, O., & Sadowski, A. (2018). Imperfection sensitivity in cylindrical shells under uniform bending. *Advances in Structural Engineering*, *21*(16), 2433–2453.

Fajuyitan, O., Sadowski, A., Wadee, M., & Rotter, M. (2018). Nonlinear behaviour of short elastic cylindrical shells under global bending. *Thin-Walled Structures*, *1777*(1). https://doi.org/https://doi.org/10.1016/j.tws.2017.12.018

Fan, H., Chen, Z., Cheng, J., Huang, S., Feng, W., & Liu, L. (2016). Analytical research on dynamic buckling of thin cylindrical shells with thickness variation under axial pressure. *Thin-Walled Structures*, *101*, 213–221. https://doi.org/10.1016/j.tws.2016.01.009

Ho, H., Xiao, T., Chen, C., & Chung, K. (2021). Determination of true stress strain characteristics of structural steels using instantaneous area method. *Journal of Physics: Conference Series*, *1777*(1). https://doi.org/10.1088/1742-6596/1777/1/012070

Intergovernmental Panel on Climate Change. (1992). *IPCC First Assessment Report Overview and Policymaker Summaries and 1992 IPPC Supplement*. https://www.ipcc.ch/report/climate-change-the-ipcc-1990-and-1992-assessments/

International Energy Agency. (2021). Clean energy technology guide. *Energy Technology Perspectives*. https://www.iea.org/articles/etp-clean-energy-technology-guide

International Renewable Energy Agency. (2016). Innovation outlook: Offshore wind. https://irena.org/publications/2016/Oct/Innovation-Outlook-Offshore-Wind

International Renewable Energy Agency. (2019). Future of wind: Deployment, investment, technology, grid integration and socio-economic aspects [A global energy transformation paper]. https://www.irena.org/publications/2019/Oct/Future-of-wind

International Renewable Energy Agency. (2021). Tracking the impacts of innovation: Offshore wind as a case study. https://www.irena.org/publications/2021/Jun/Impact-of-Innovation-Offshore-wind-case-study

Iwicki, P., Tejchman, J., & Chróścielewski, J. (2014). Dynamic fe simulations of buckling process in thin-walled cylindrical metal silos. *Thin-Walled Structures*, *84*, 344–359. https://doi.org/10.1016/j.tws.2014.07.011

Jabareen, M., & Sheinman, I. (2007). Buckling and Sensitivity to Imperfection of Conical Shells Under Dynamic Step-Loading. *Journal of Applied Mechanics*, *74*(1), 74–80. https://doi.org/10.1115/1.2178836

Kim, B.-s., Jin, J.-w., Bitkina, O., & Kang, K.-w. (2015). Ultimate load characteristics of nrel 5-mw offshore wind turbines with different substructures. *International Journal of Energy Research*, *40*(5), 639–650. https://doi.org/10.1002/er.3430

Kouchakzadeh, M., & Shakouri, M. (2014). Analytical solution for axisymmetric buckling of joined conical shells under axial compression. *Structural Engineering and Mechanics*, *54*(4), 649–664. https://doi.org/10.12989/sem.2015.54.4.649

Kweon, H. D., Kim, J. W., Son, O., & Oh, D. (2020). Determination of true stress-strain curve of type 304 and 316 stainless steels using a typical tensile test and finite element analysis. *Nuclear Engineering and Technology*, *53*(2), 647–656. https://doi.org/10.1016/j.net.2020.07.014

Li, S., & Kim, D. K. (2022). Ultimate strength characteristics of unstiffened cylindrical shell in axial compression. *Ocean Engineering*, *243*. https://doi.org/10.1016/j.oceaneng.2021.110253

Liang, K., & Li, Z. (2022). A novel and higly efficient strategy to determine the 'worst' imperfection shape for buckling of cylindrical shell panels. *Applied Mathematical Modelling*, *105*, 631–647. https://doi.org/https://doi.org/10.1016/j.apm.2022.01.012

Lourens, E.-M. (2021). Support structure design [Lecture notes of the course Offshore Wind Farms Design at TU Delft].

Mulazzani, D. (2021). *Evolution of offshore foundations*. offshoreWIND. https://www.offshorewind.biz/2021/02/02/evolution-of-offshore-foundations/

NEN. (2007). Eurocode 3: Design of steel structures - part 1-6: General - strength and stability of shell structures [NEN-EN 1993-1-6].

Rotter, J. M., Sadowski, A. J., & Chen, L. (2014). Nonlinear stability of thin elastic cylinders of different length under global bending. *International Journal of Solids and Structures*, *51*(15-16), 2826–2839. https://doi.org/10.1016/j.ijsolstr.2014.04.002

Rotter, J., & Al-Lawati, H. (2016). Length effects in the buckling of imperfect axially compressed cylinders. *Proceedings of the International Colloquium on Stability and Ductility of Steel Structures, SDSS 2016*, 631–638.

Shames, I. H., & Dym, C. L. (2013). *Solid mechanics: A variational approach* (Augmented). Springer.

Sofiyev, A. H. (2005). The stability of compositionally graded ceramic-metal cylindrical shells under aperiodic axial impulsive loading. *Composite Structures*, *69*(2), 247–257. https://doi.org/10.1016/j.compstruct.2004.07.004

Sofiyev, A. H., & Aksogan, O. (2004). Buckling of a conical thin shell with variable thickness under a dynamic loading. *Journal of Sound and Vibration*, *270*(4-5), 903–915. https://doi.org/10.1016/S0022-460X(03)00638-2

Sun, W., Zhu, T., Chen, P., & Lin, G. (2022). Dynamic implosion of submerged cylindrical shell under the combined hydrostatic and shock loading. *Thin-Walled Structures*, *170*. https://doi.org/https://doi.org/10.1016/j.jfluidstructs.2019.06.001

Timoshenko, S. P., & Gere, J. M. (1961). *Theory of elastic stability* (1st). Dover Publications.

TNO DIANA BV. (2011). *Diana finite element analysis user's manual: Analysis procedures*.

United Nations. (1992). *United nations conference on environment and development, rio de janeiro, brazil, 3-14 june 1992*. https://www.un.org/en/conferences/environment/rio1992

United Nations. (2015). *The paris agreement*. https://www.un.org/en/climatechange/paris-agreement

United Nations. (2021). *Cop26 - the glasgow climate pact*. https://unfccc.int/process-and-meetings/the-paris-agreement/the-glasgow-climate-pact-key-outcomes-from-cop26

Wang, J., & Sadowski, A. J. (2020). Elastic imperfect cylindrical shells of varying length under combined axial compression and bending. *Journal of Structural Engineering*, *146*(4). https://doi.org/https://doi.org/10.1061/(ASCE)ST.1943-541X.0002560

Warburton, G. (1969). Natural frequencies of thin cantilever cylindrical shells. *Journal of Sound and Vibration*, *11*(3), 335–338. https://doi.org/10.1016/S0022-460X(70)80037-2

Wojtaszek, M., Sleboda, T., Czulak, A., Weber, G., & Hufenbach, W. (2013). Quasi-static and dynamic tensile properties of ti-6al-4v alloy. *Archives of Metallurgy and Materials*, *58*(4), 1261–1265. https://doi.org/10.2478/amm-20134145

Xu, X., Ma, J., Lim, C. W., & Chu, H. (2009). Dynamic local and global buckling of cylindrical shells under axial impact. *Engineering Structures*, *31*(5), 1132–1140. https://doi.org/10.1016/j.engstruct.2009.01.009

Xu, X., Ma, Y., Lim, C. W., & Chu, H. (2005). Dynamic buckling of cylindrical shells subject to an axial impact in a symplectic system. *International Journal of Solids and Structures*, *43*(13), 3905–3919. https://doi.org/10.1016/j.ijsolstr.2005.03.005

Zaczynska, M., Abramovich, H., & Bisagni, C. (2020). Parametric studies on the dynamic buckling phenomenon of a composite cylindrical shell under impulsive axial compression. *Journal of Sound and Vibration*, *482*. https://doi.org/10.1016/j.jsv.2020.115462

Zhou, M., Zheng, S., & Zhang, W. (1991). Study on elephant-foot buckling of broad liquid storage tanks by nonlinear theory of shells. *Computers and Structures*, *44*(4), 783–788. https://doi.org/10.1016/0045-7949(92)90462-9

A

Moment vs time graphs

In this attachment, all moment vs time graphs are shown, with the critical buckling moment indicated by a red marker.

A.1. Perfect cylinders

A.1.1. Geometry 1

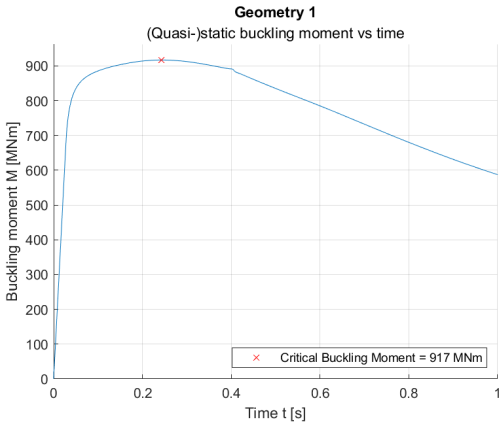

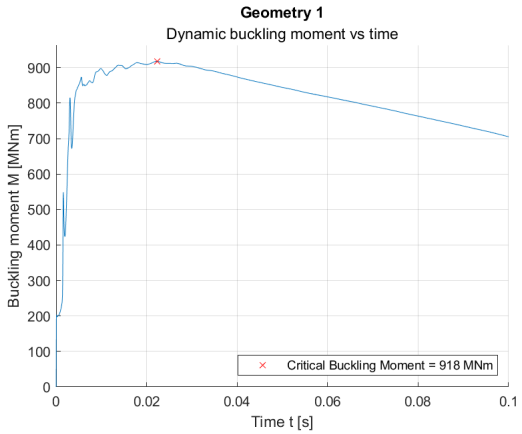

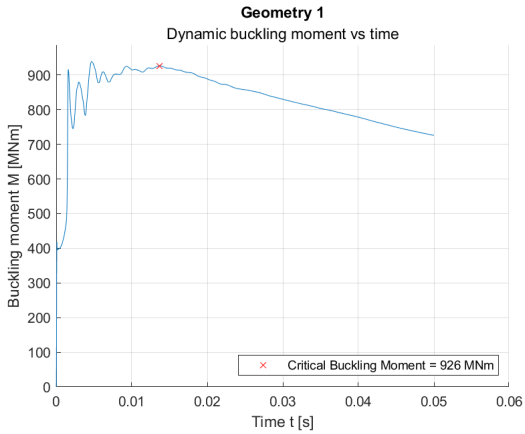

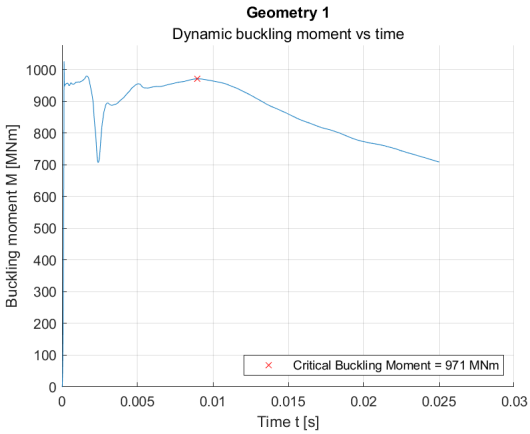

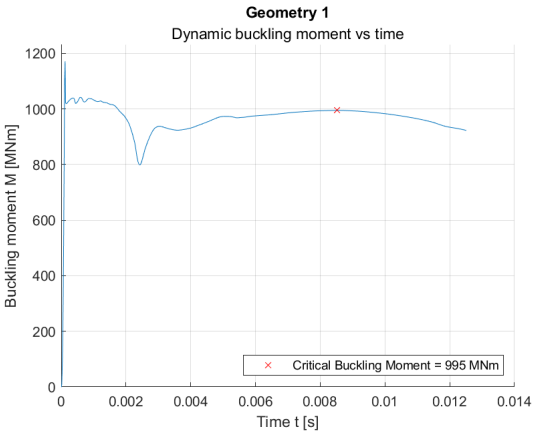

A.1.2. Geometry 2

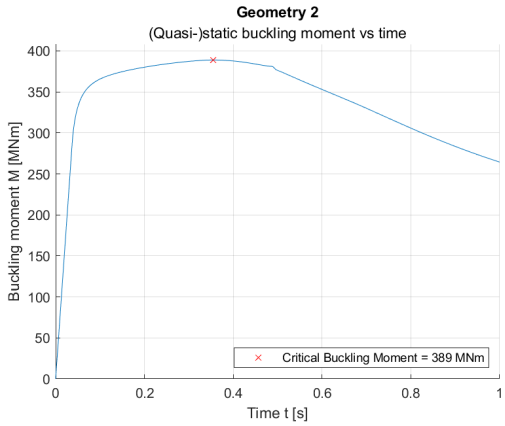

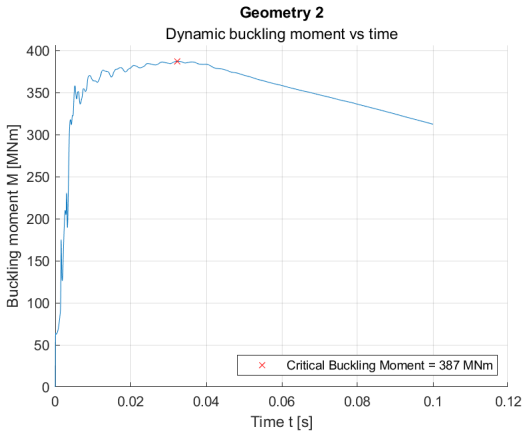

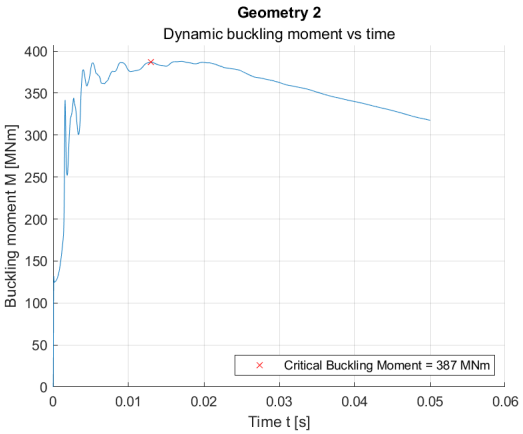

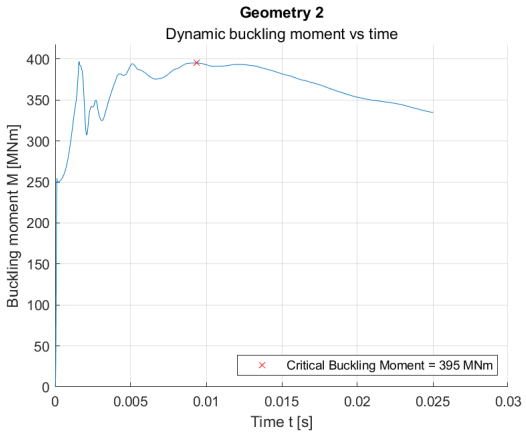

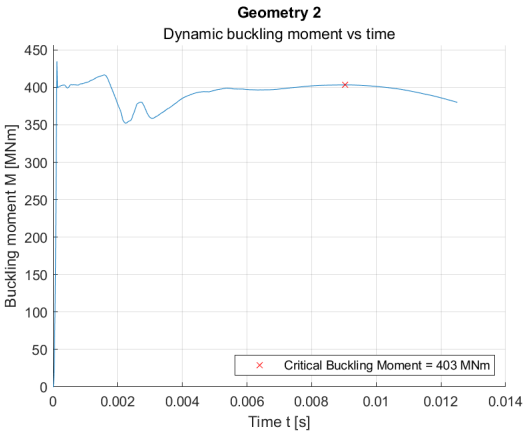

A.1.3. Geometry 3

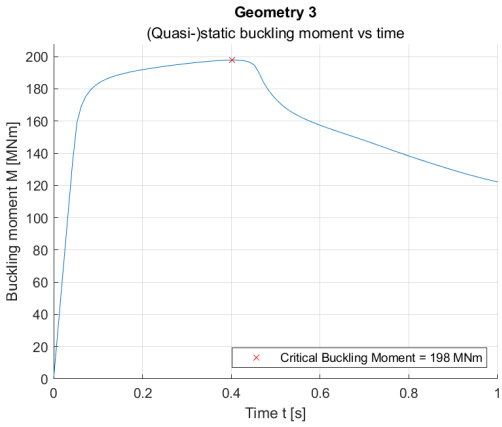

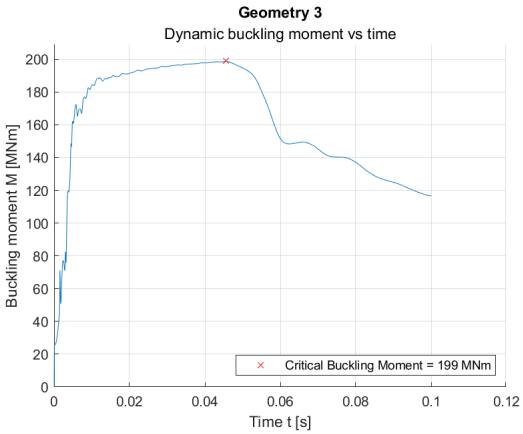

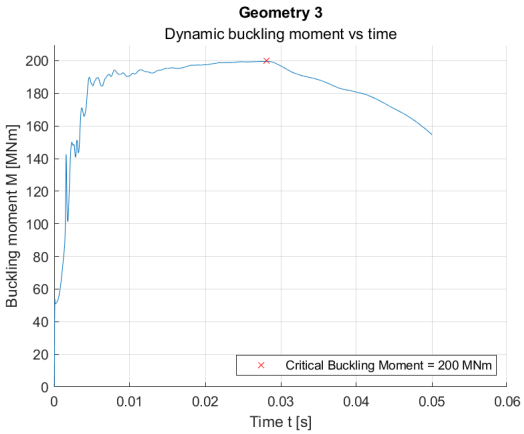

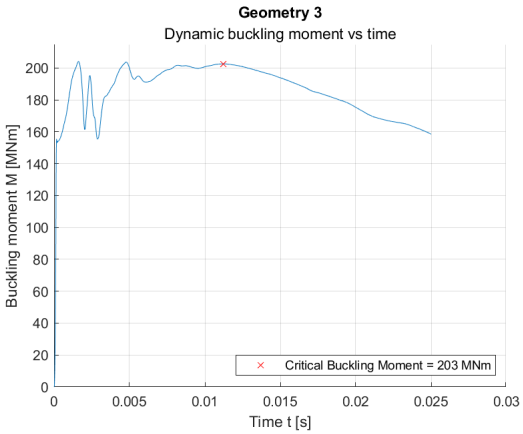

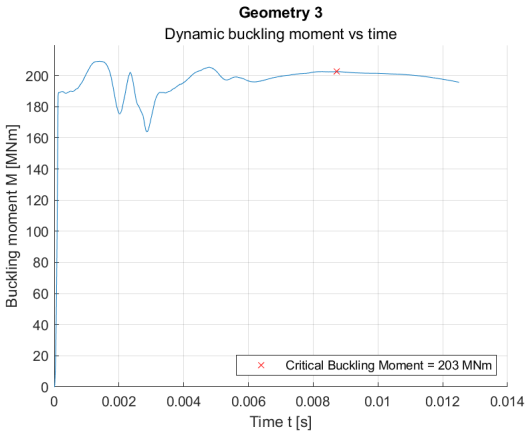

A.1.4. Geometry 4

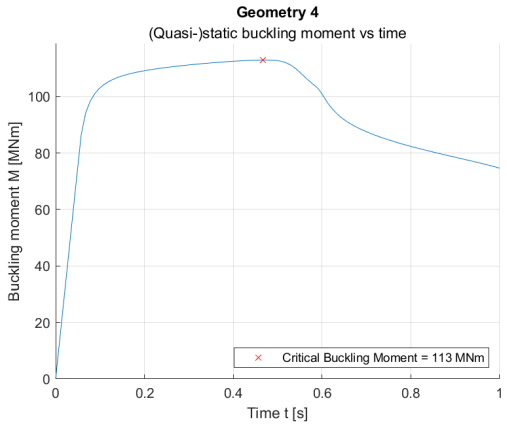

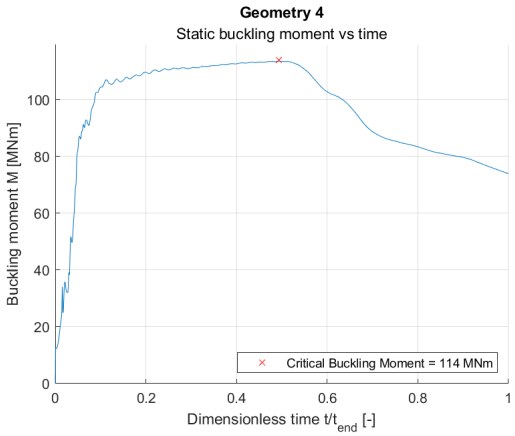

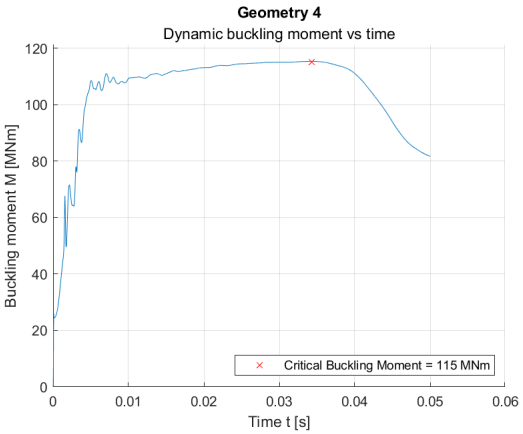

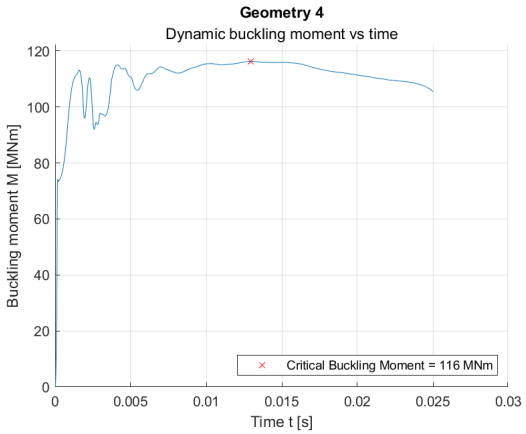

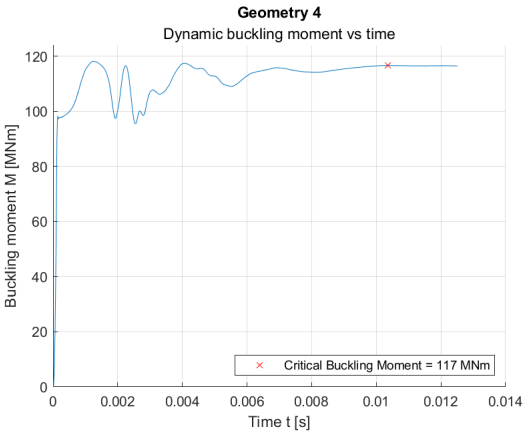

A.1.5. Geometry 5

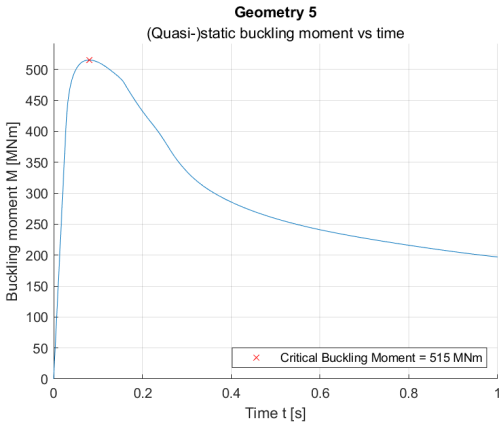

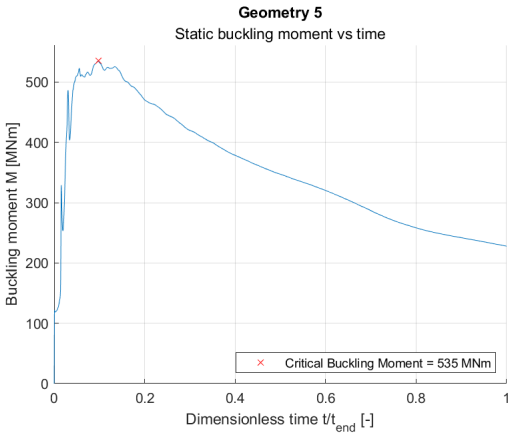

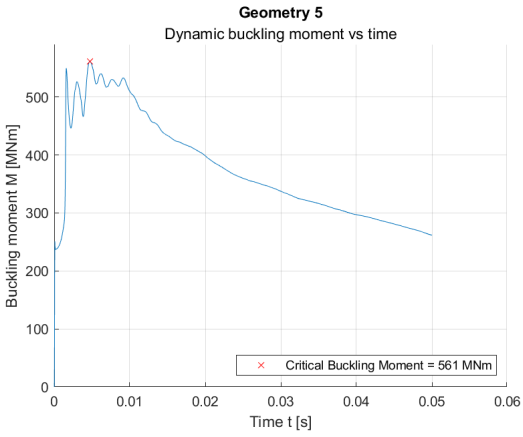

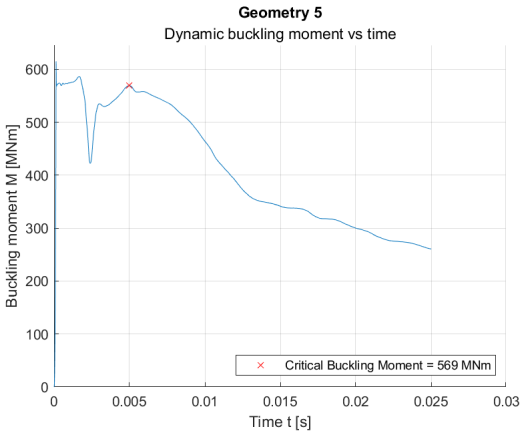

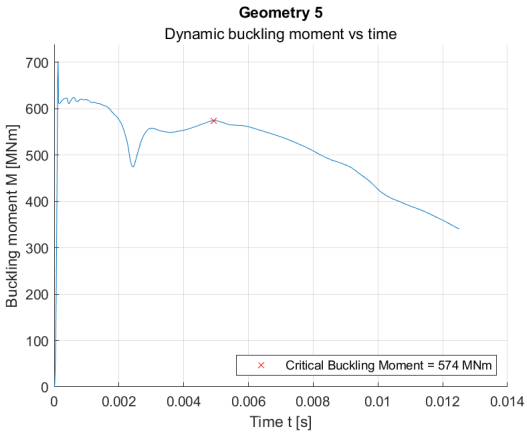

A.1.6. Geometry 6

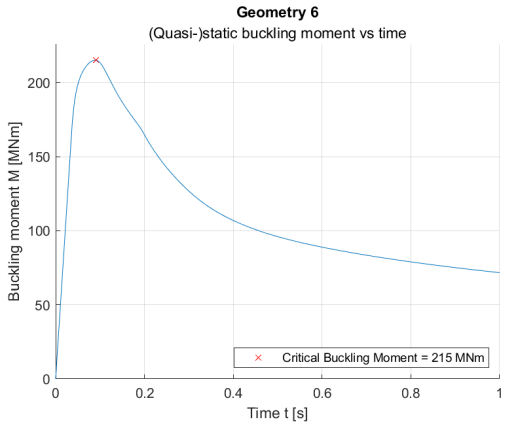

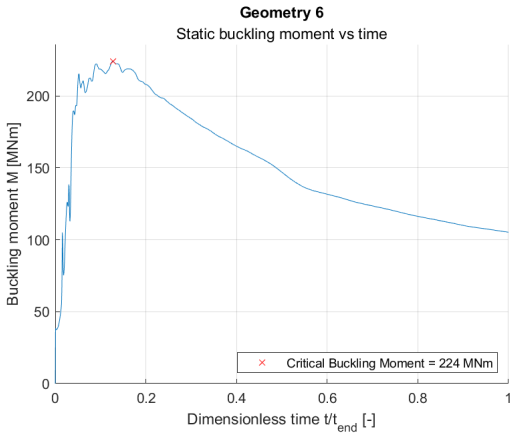

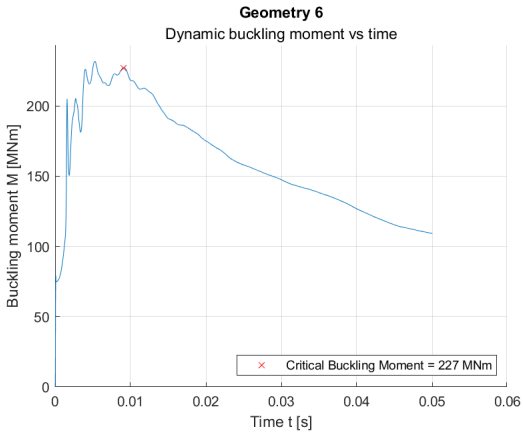

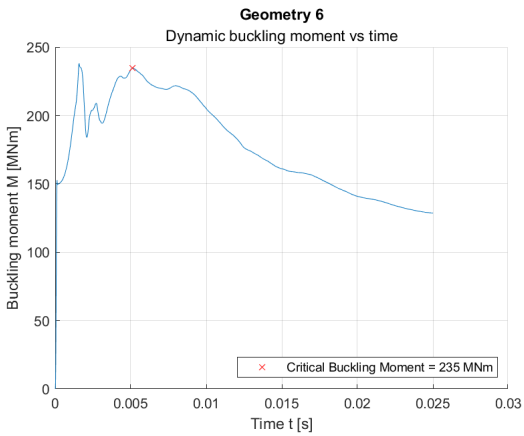

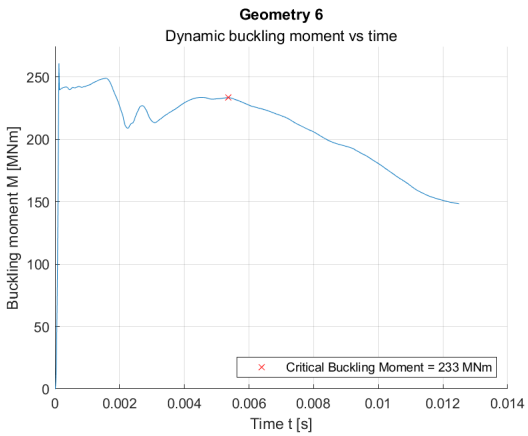

A.1.7. Geometry 7

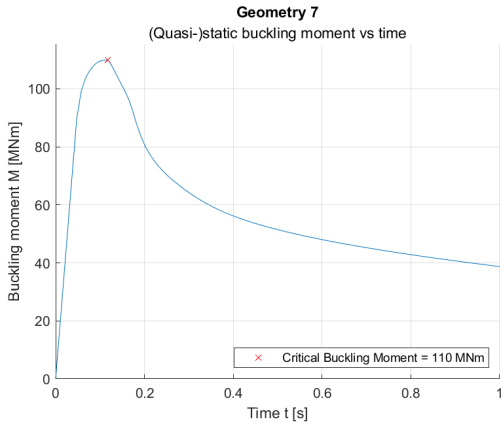

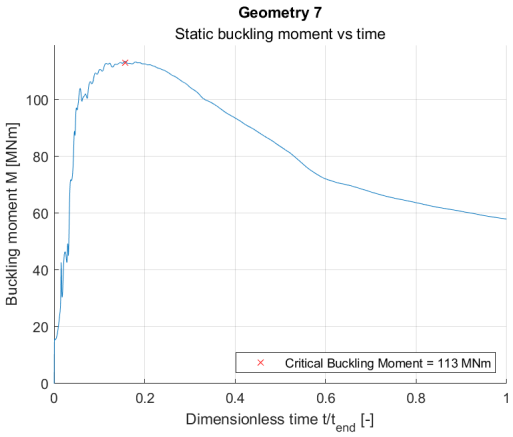

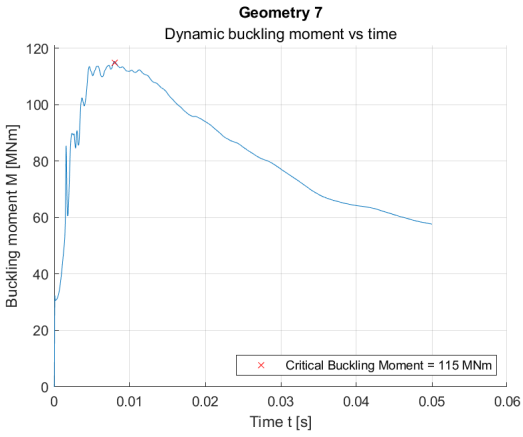

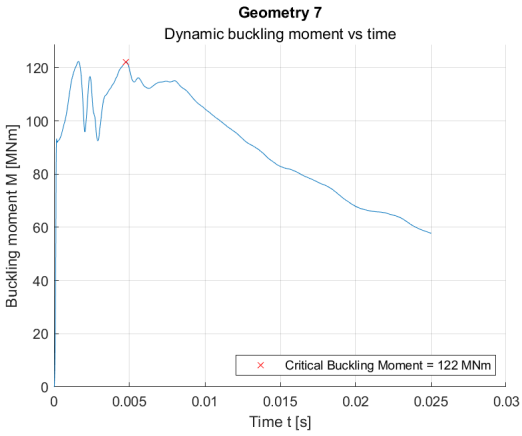

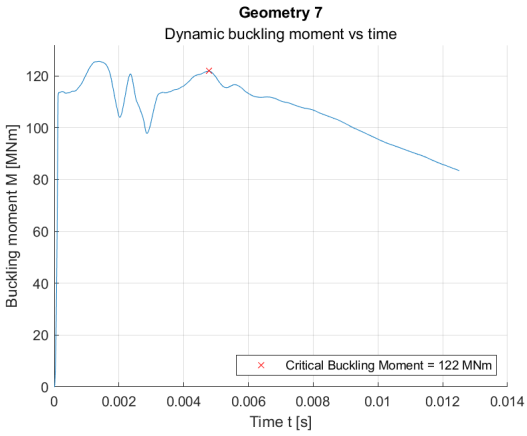

A.1.8. Geometry 8

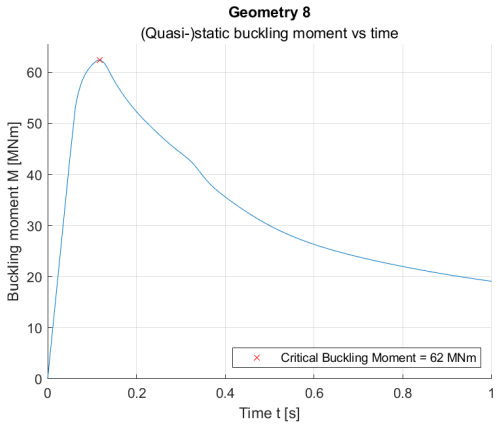

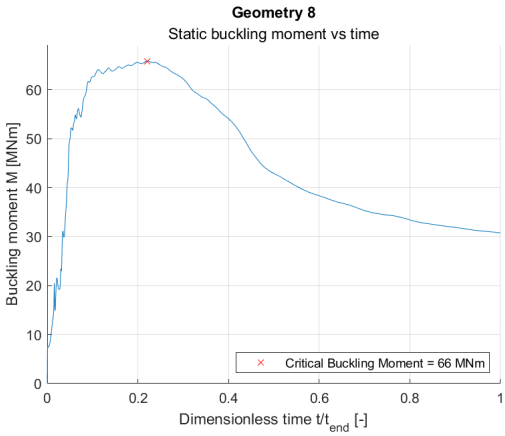

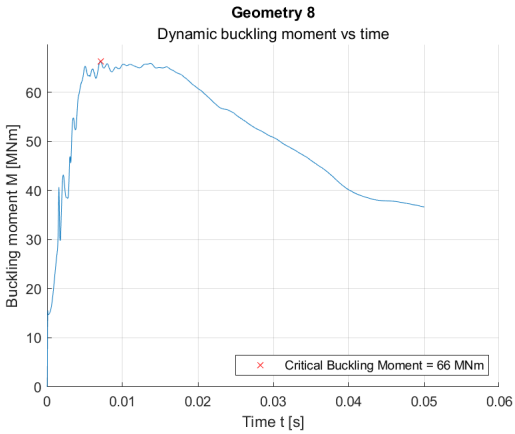

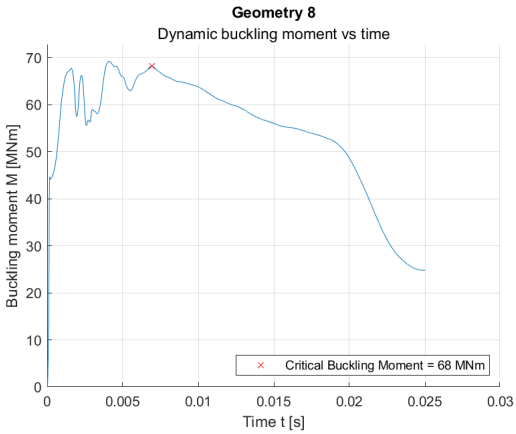

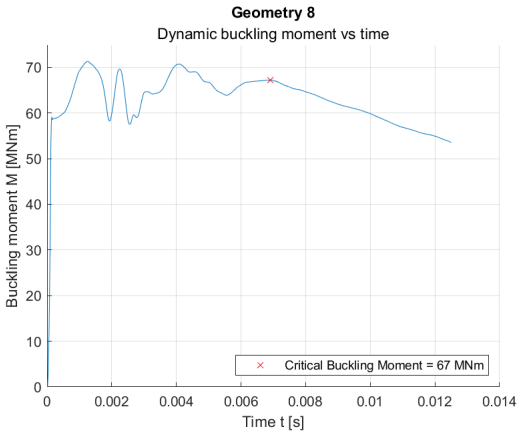

A.1.9. Geometry 9

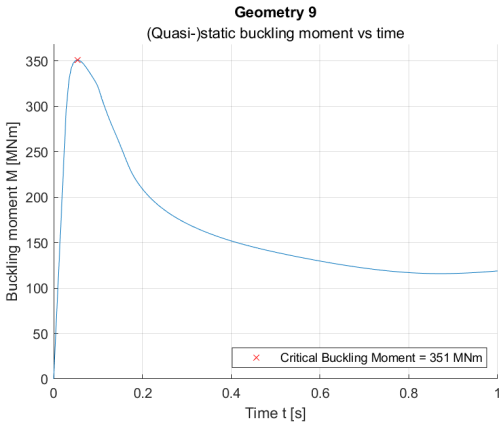

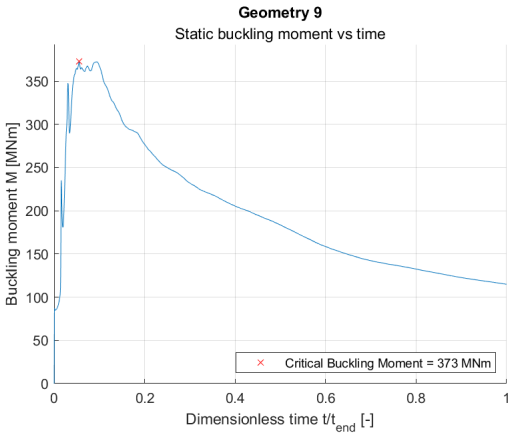

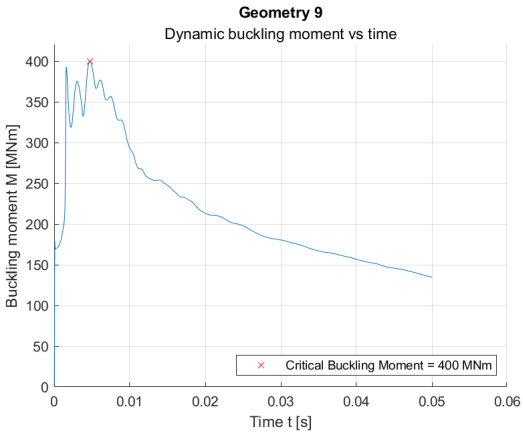

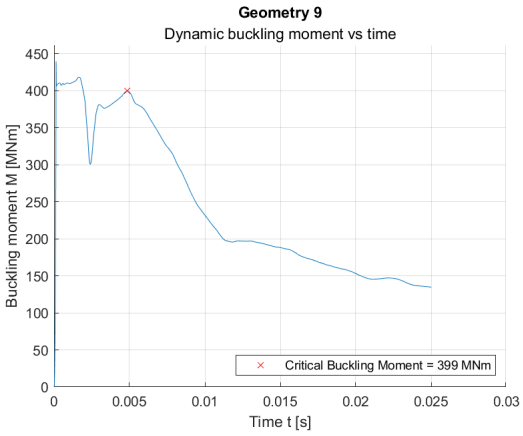

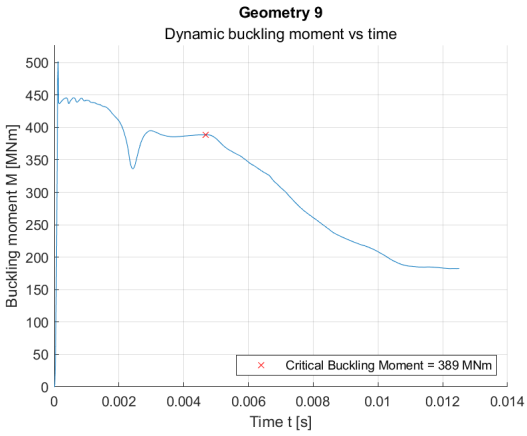

A.1.10. Geometry 10

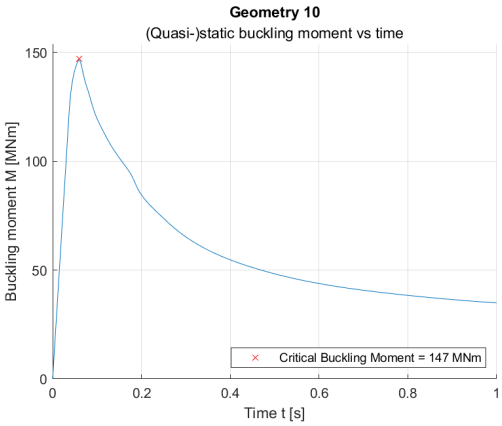

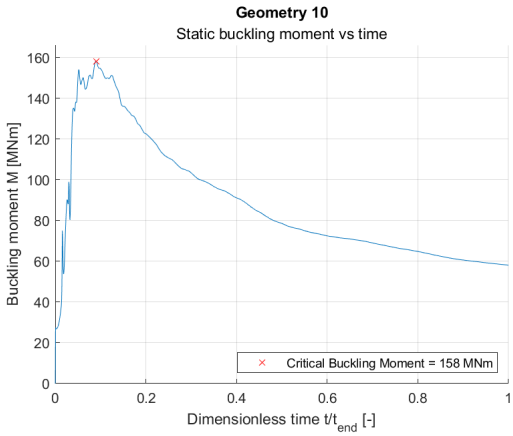

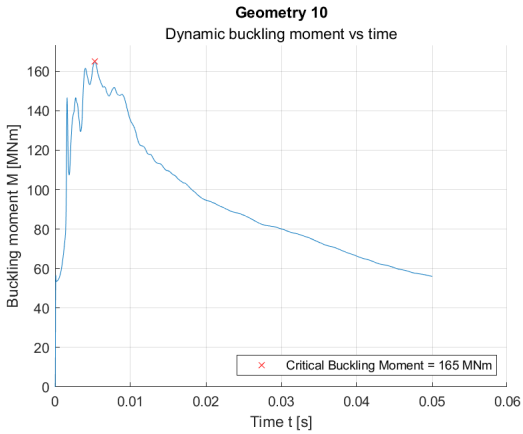

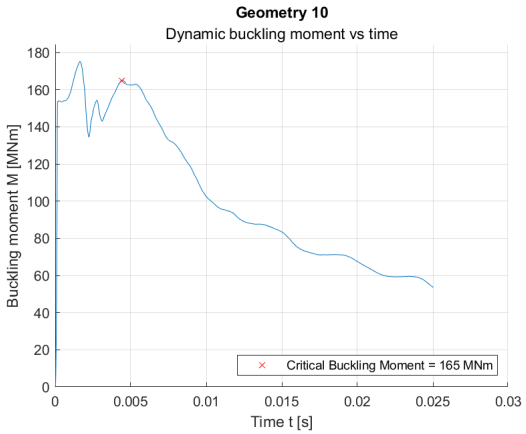

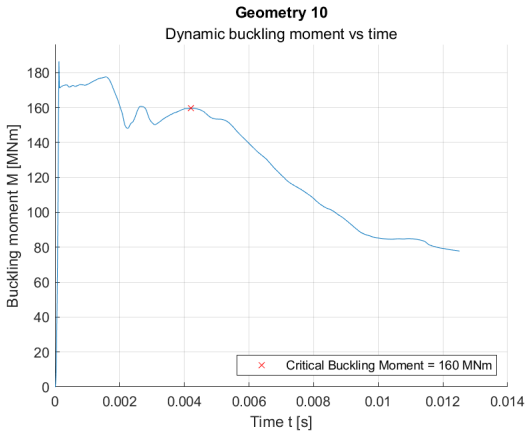

A.1.11. Geometry 11

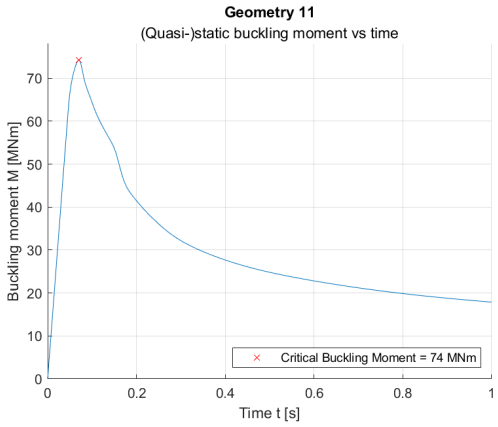

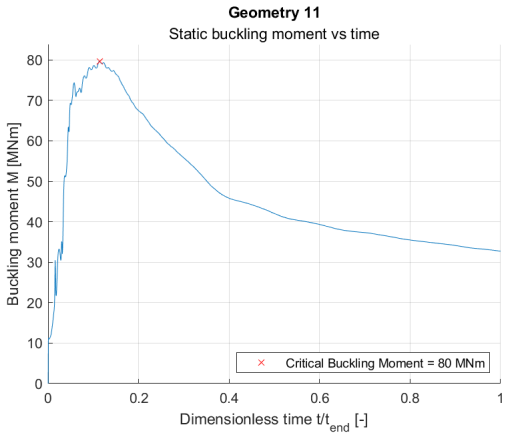

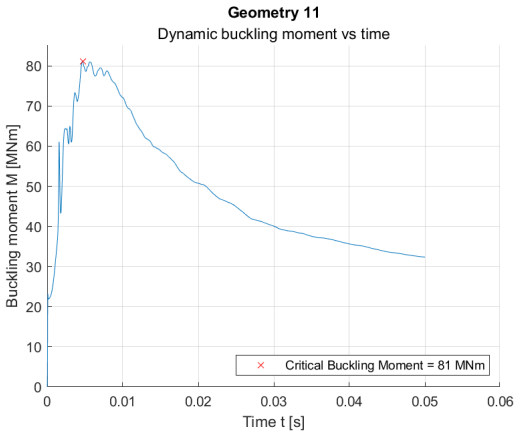

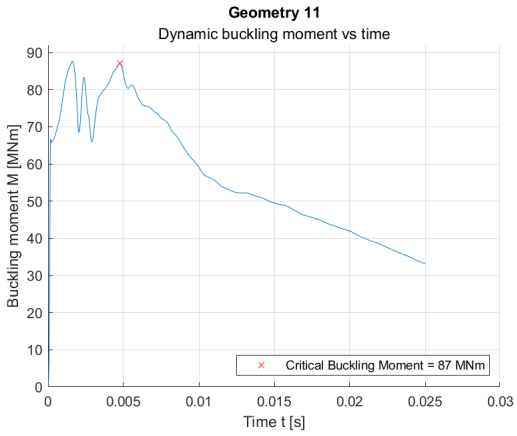

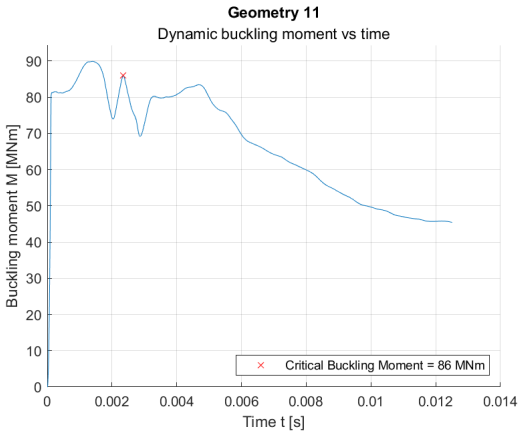

A.1.12. Geometry 12

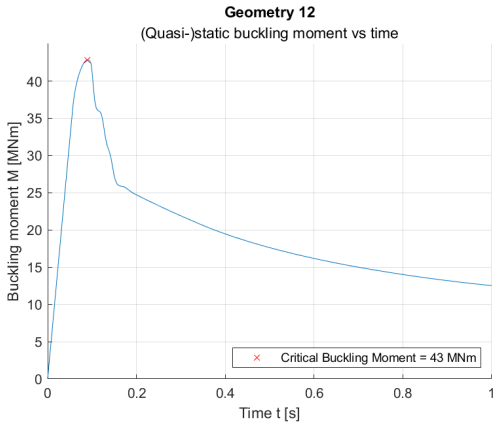

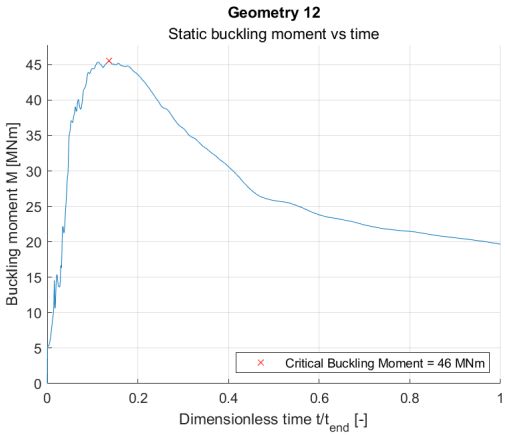

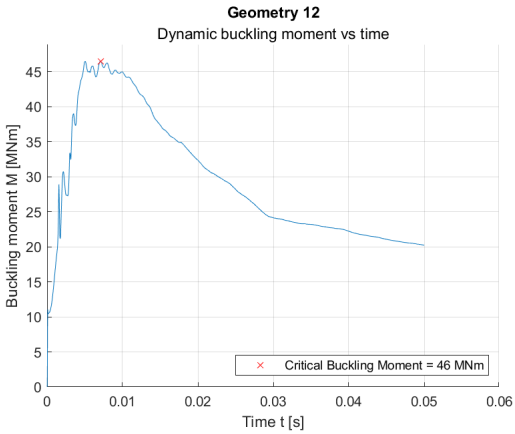

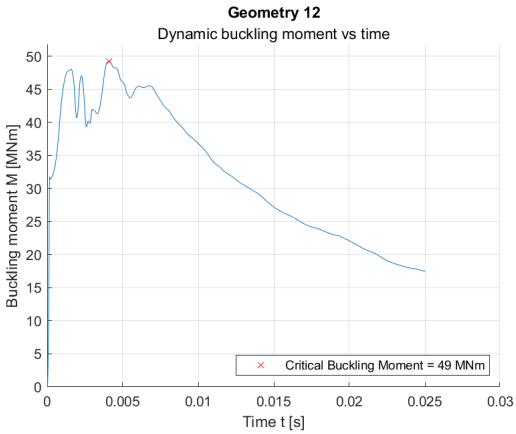

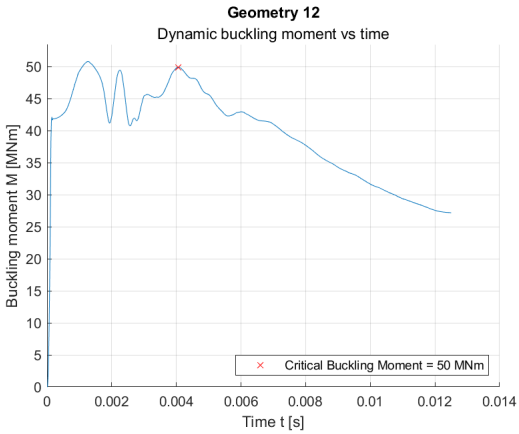

A.1.13. Geometry 13

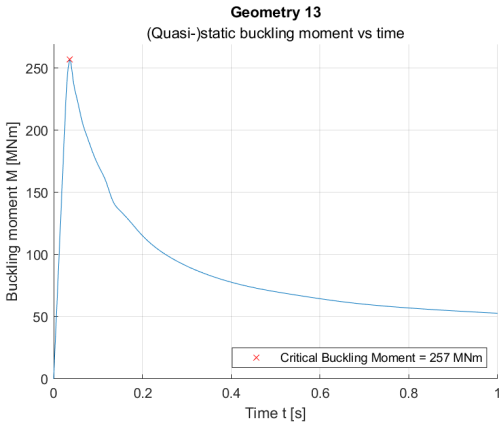

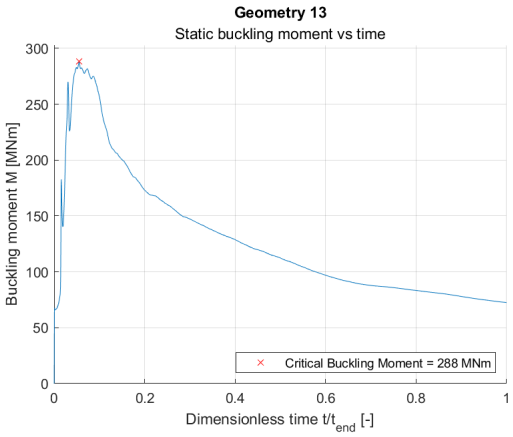

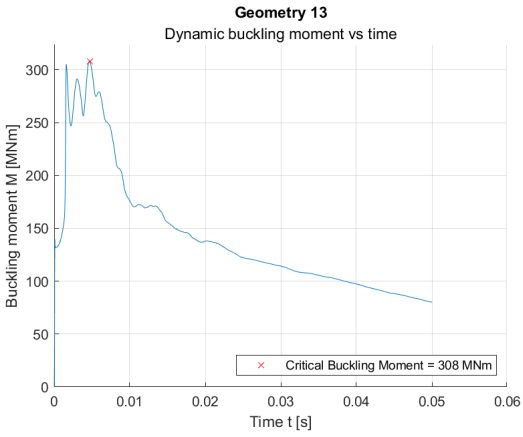

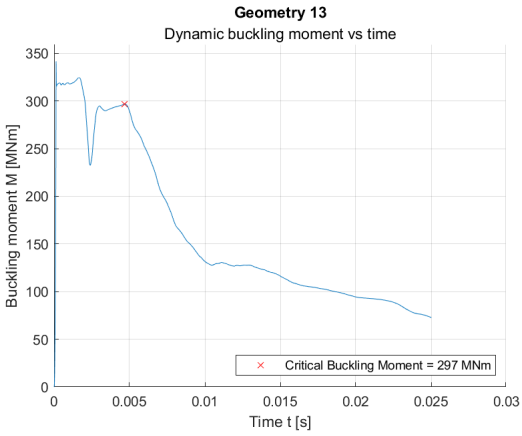

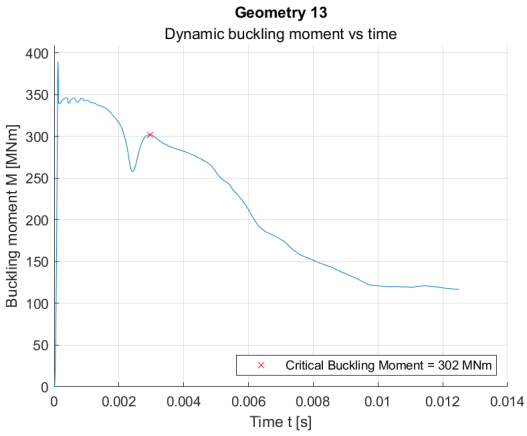

A.1.14. Geometry 14

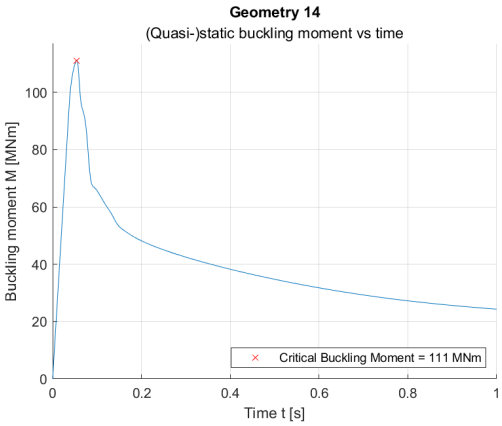

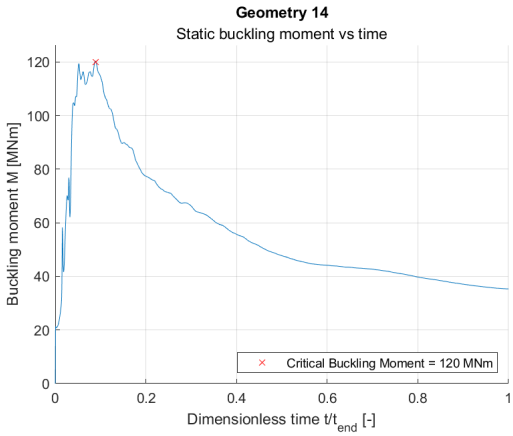

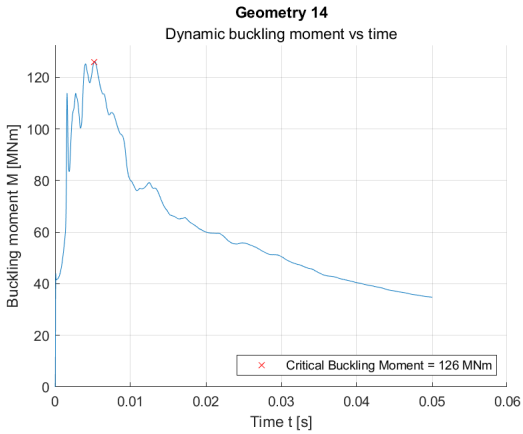

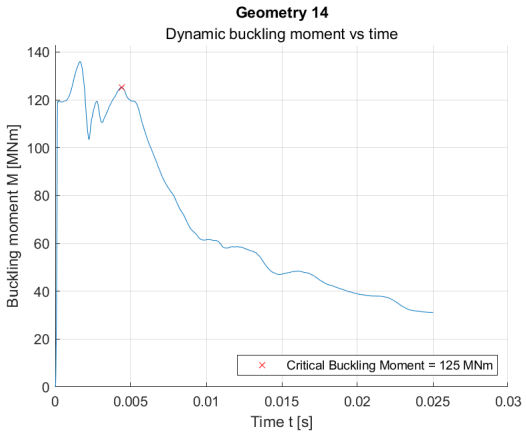

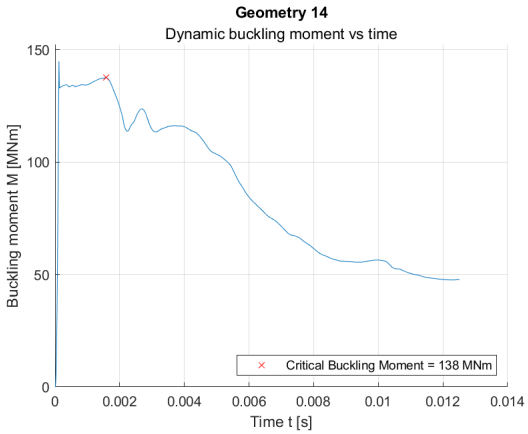

A.1.15. Geometry 15

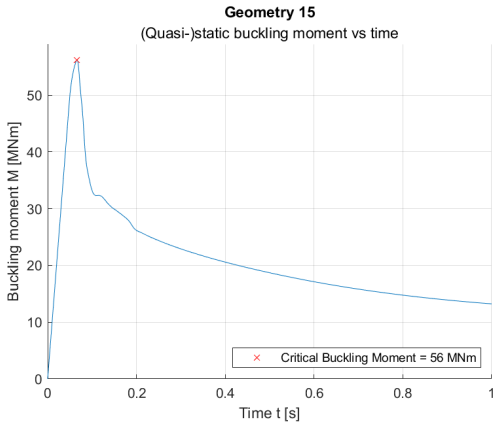

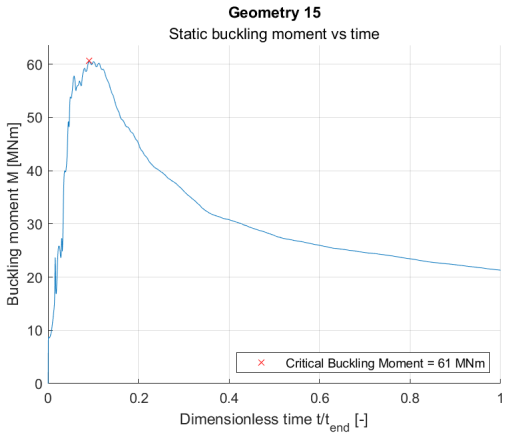

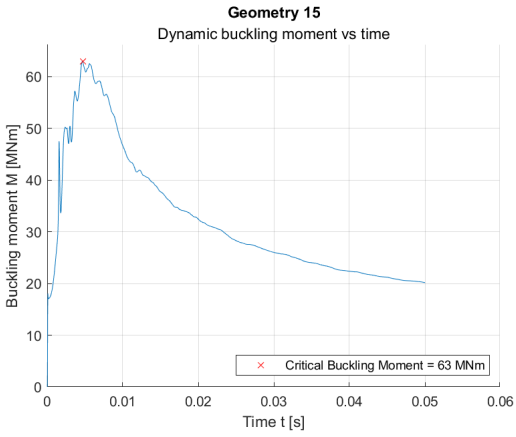

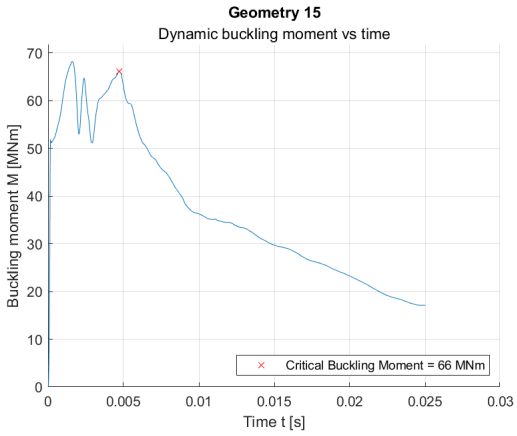

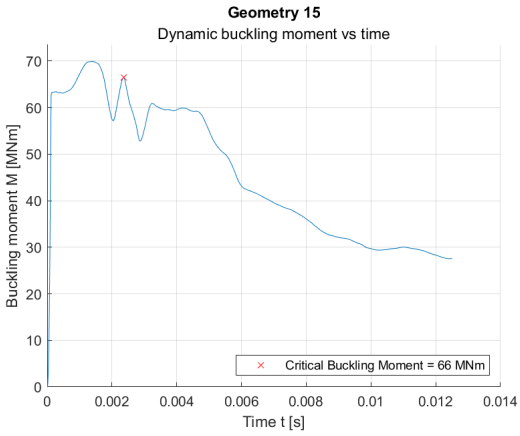

A.1.16. Geometry 16

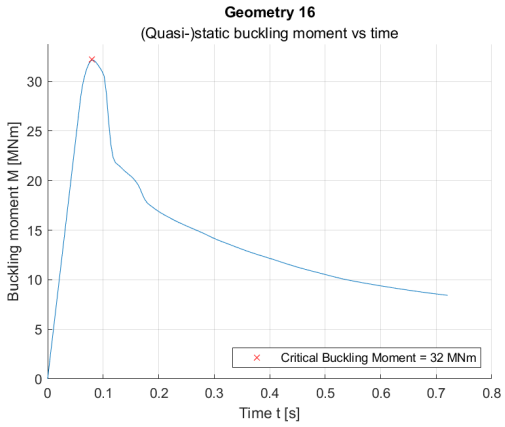

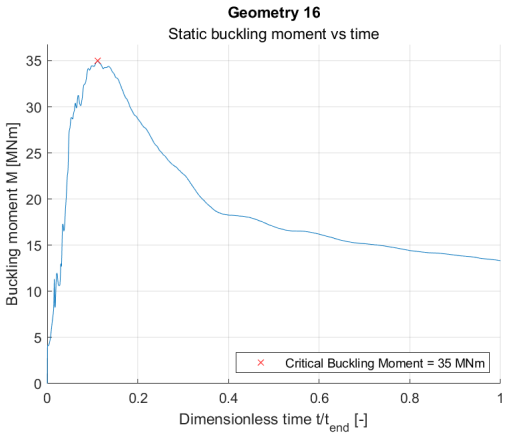

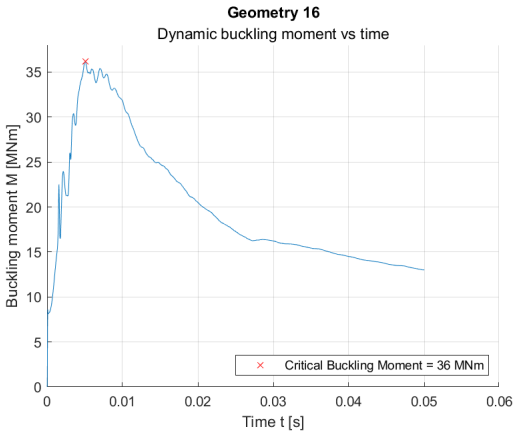

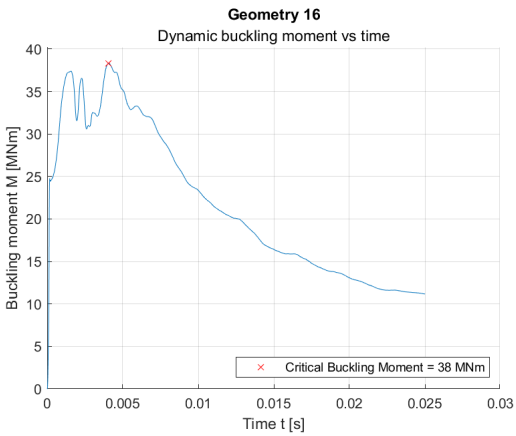

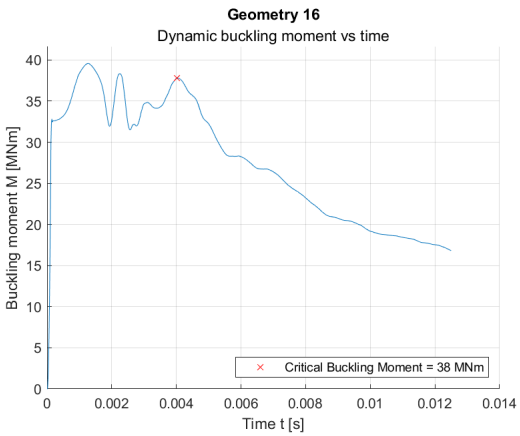

A.2. Imperfect cylinders

A.2.1. Geometry 1

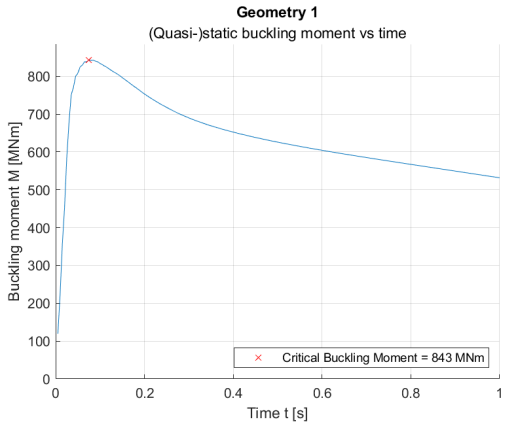

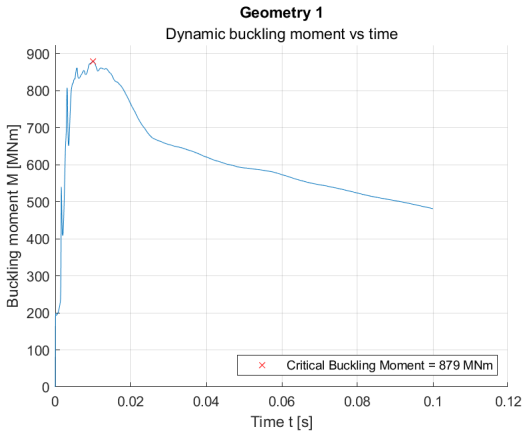

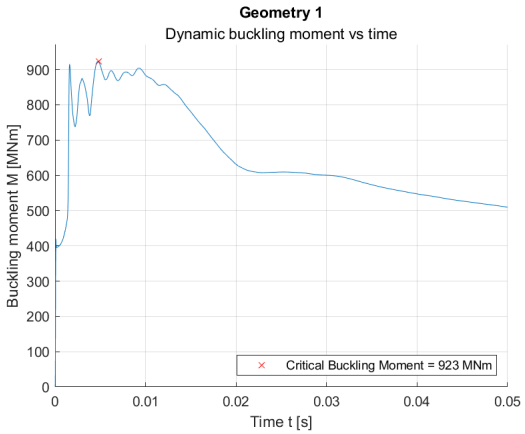

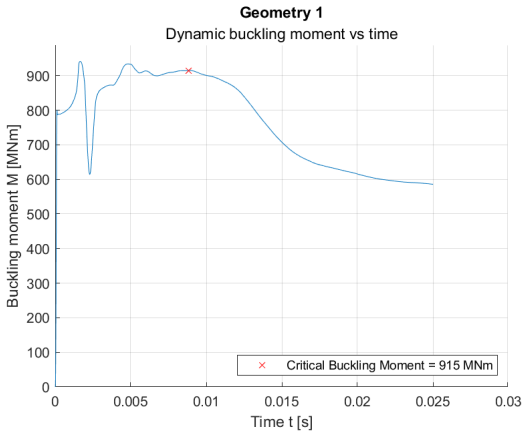

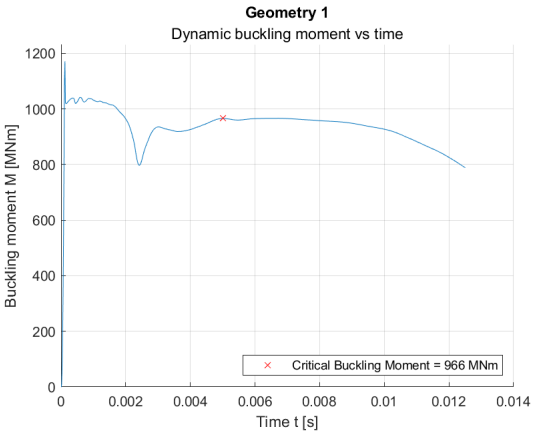

A.2.2. Geometry 2

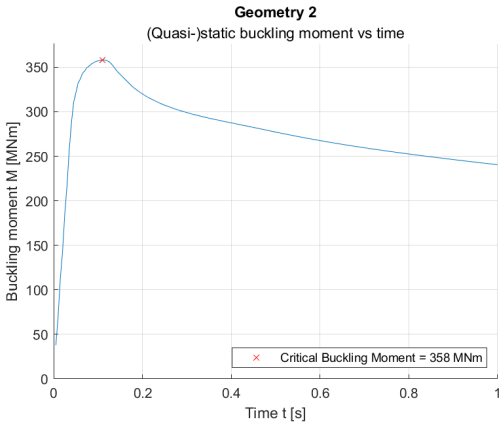

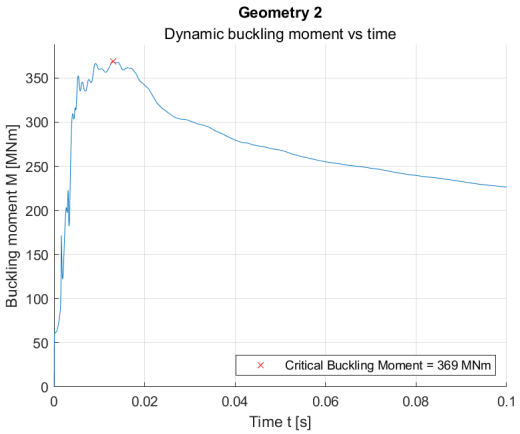

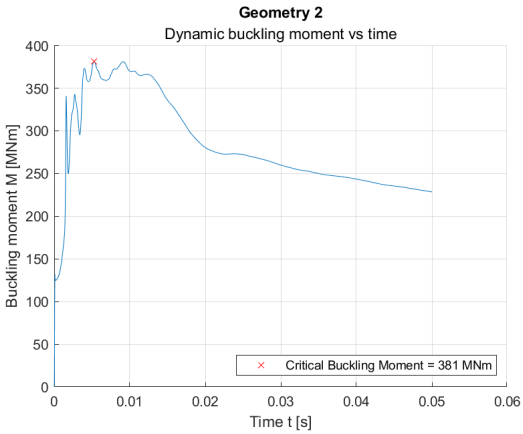

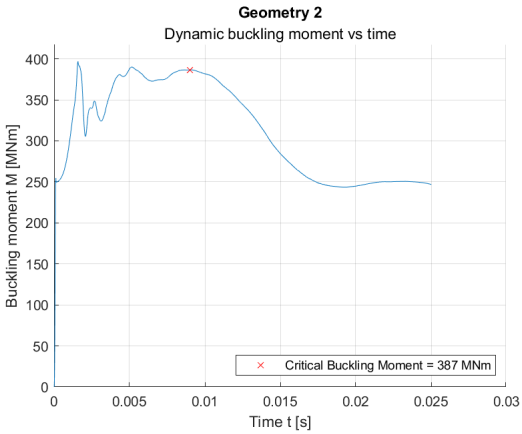

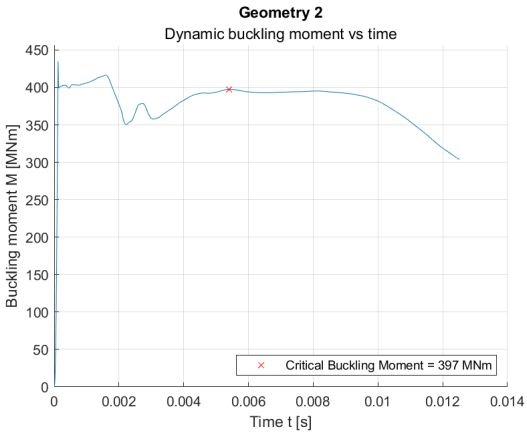

A.2.3. Geometry 3

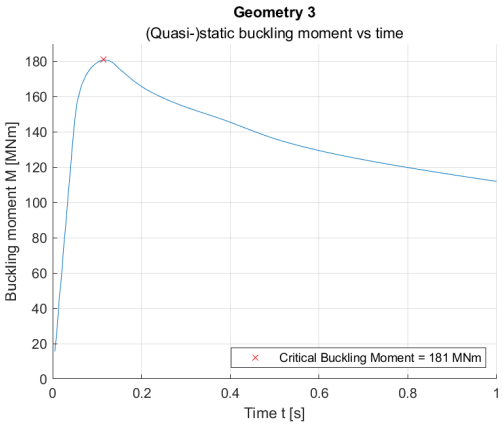

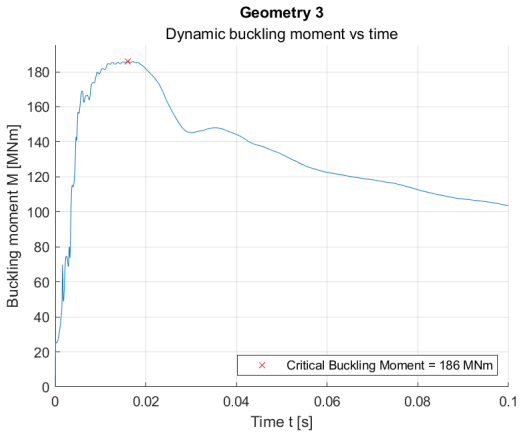

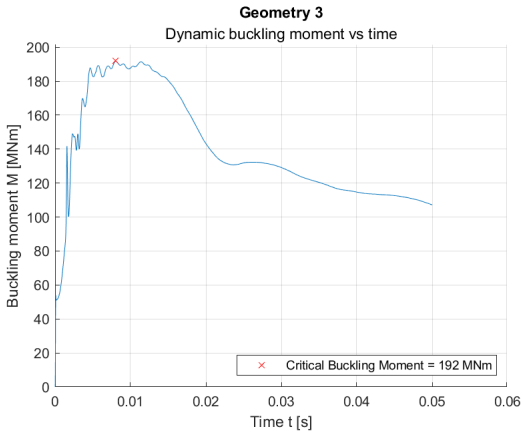

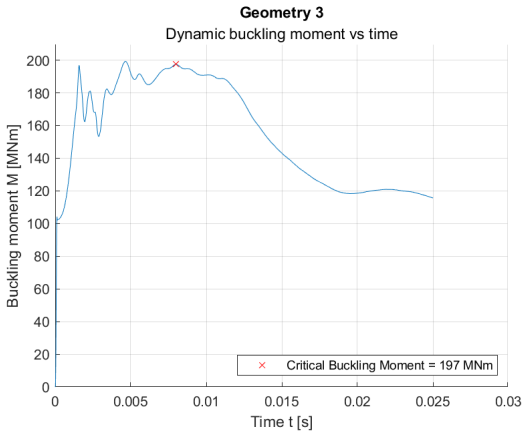

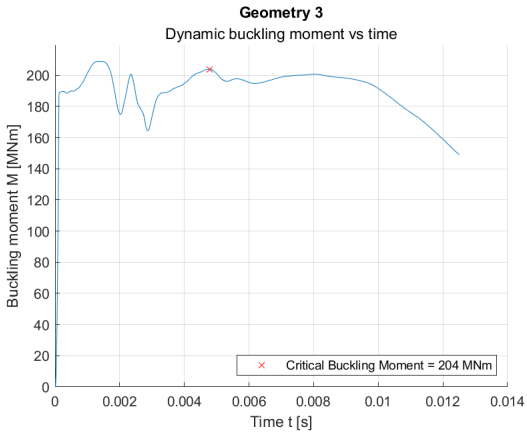

A.2.4. Geometry 4

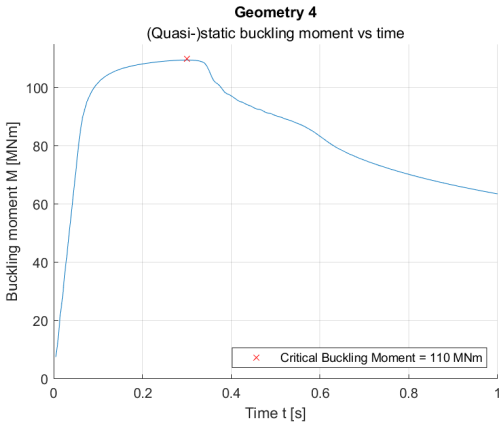

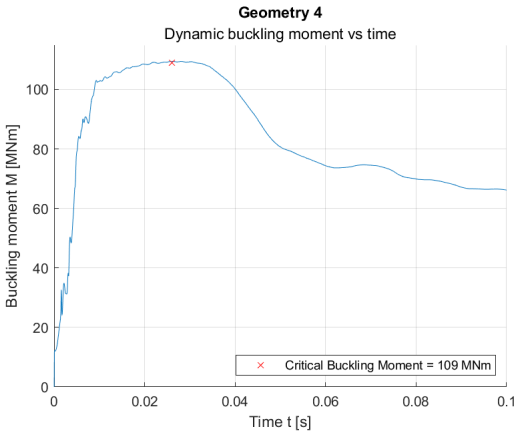

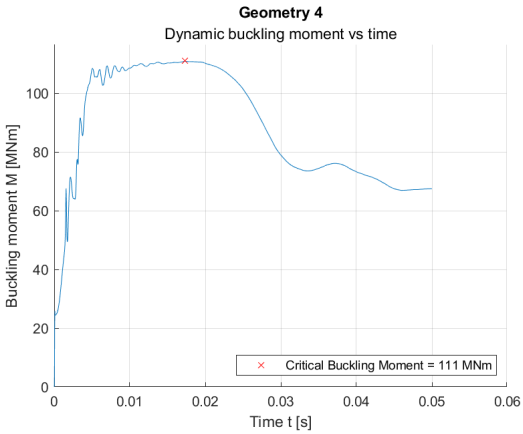

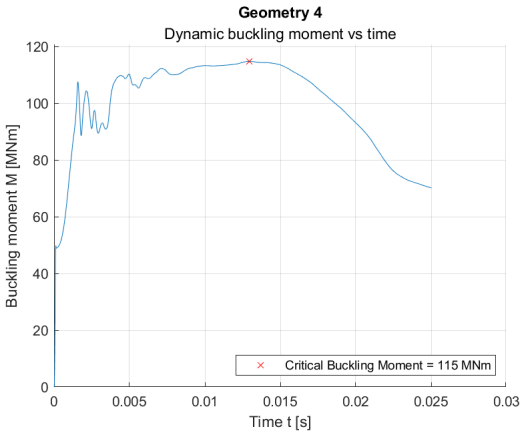

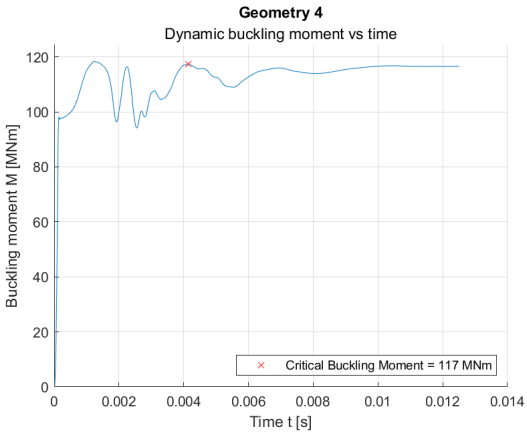

A.2.5. Geometry 5

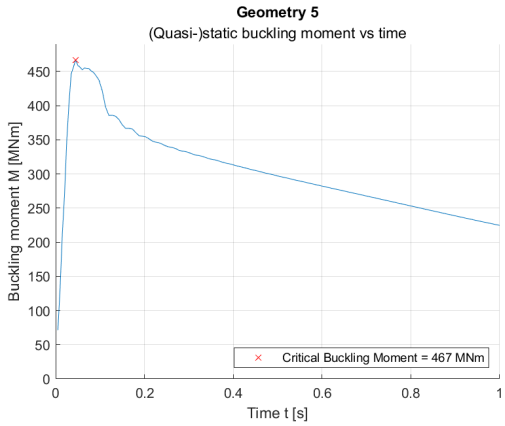

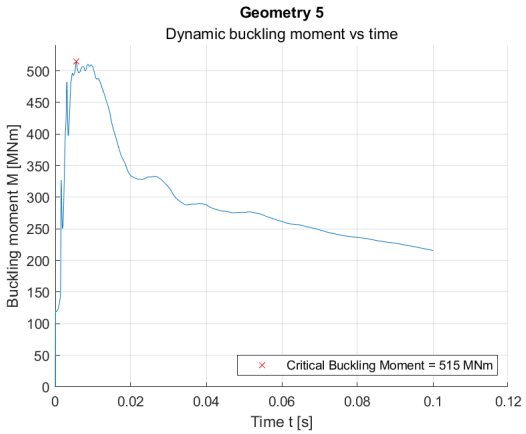

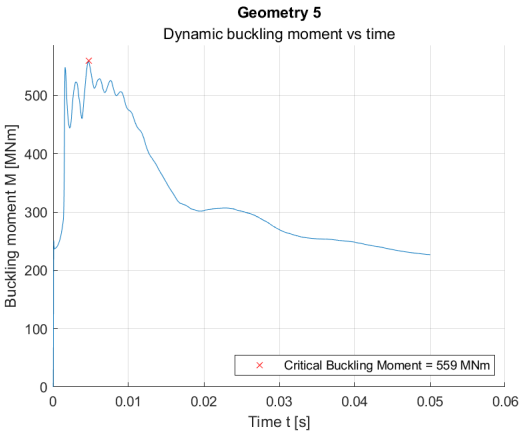

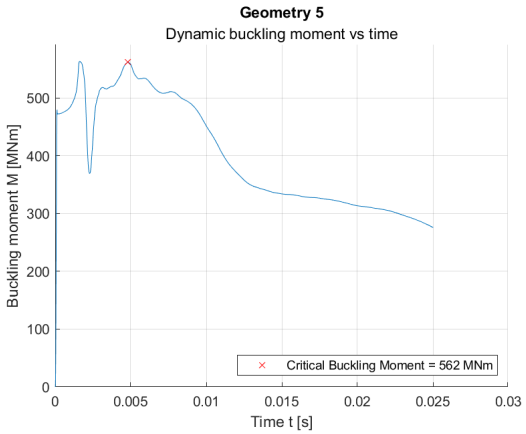

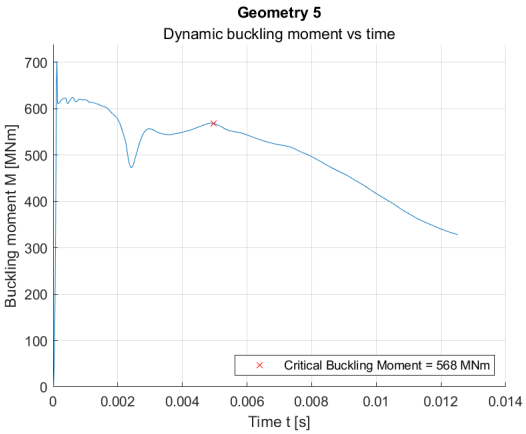

A.2.6. Geometry 6

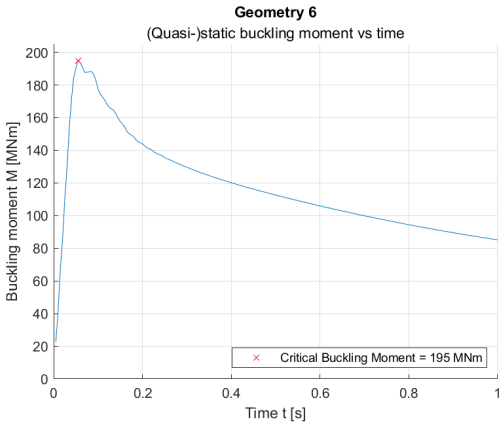

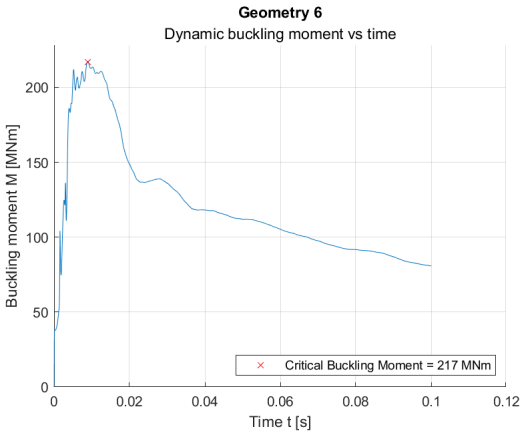

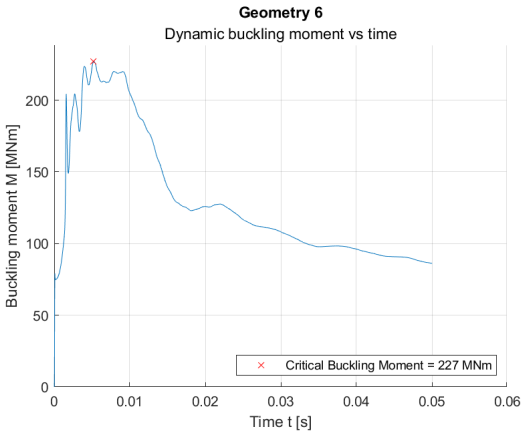

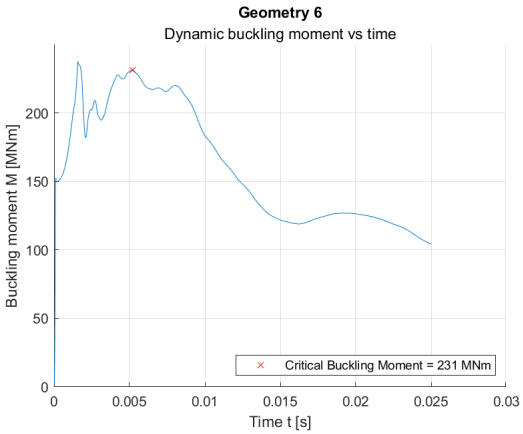

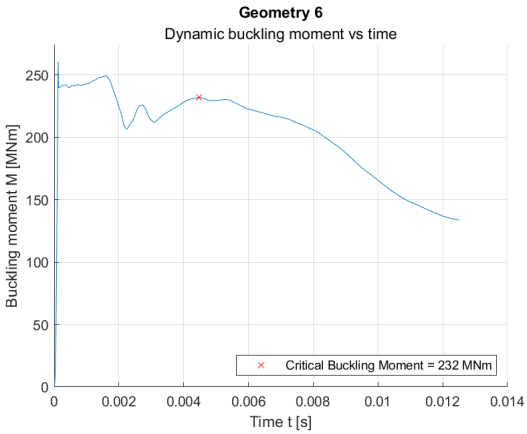

A.2.7. Geometry 7

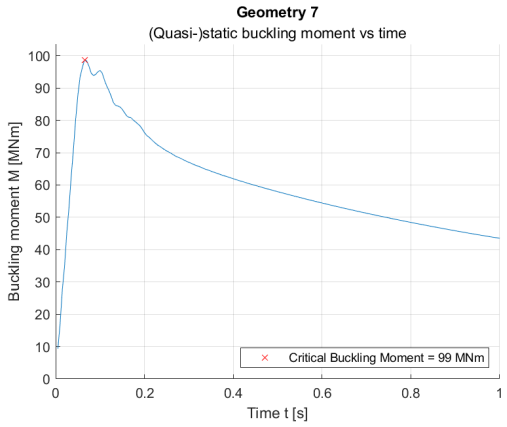

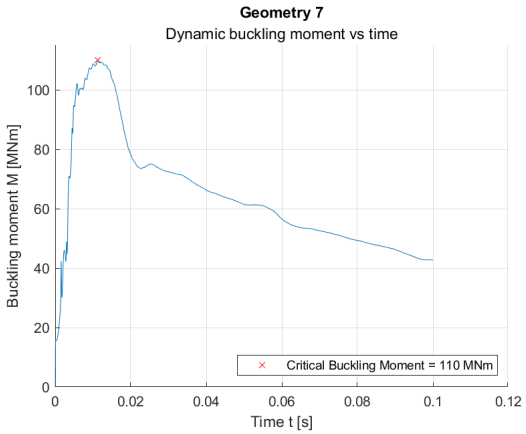

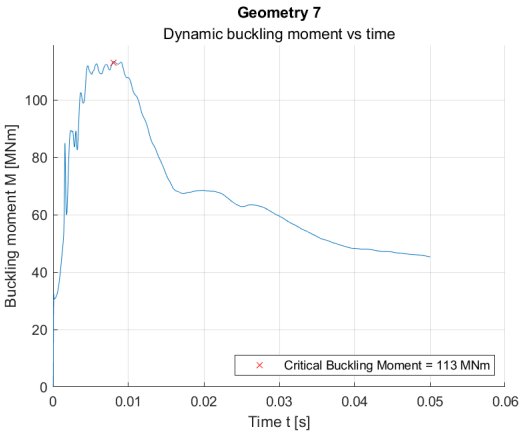

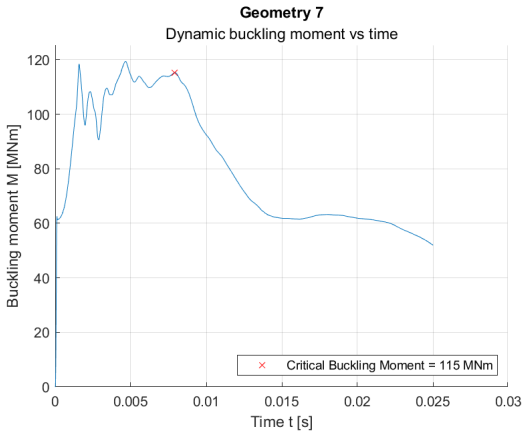

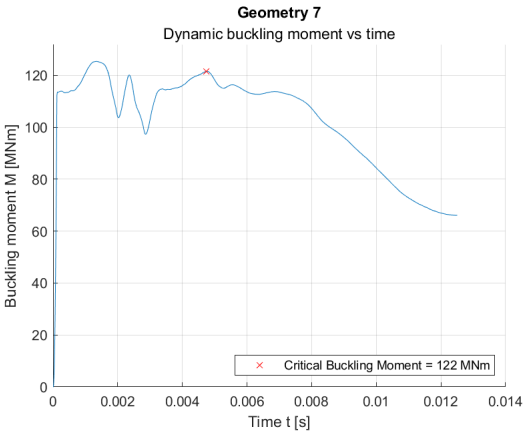

A.2.8. Geometry 8

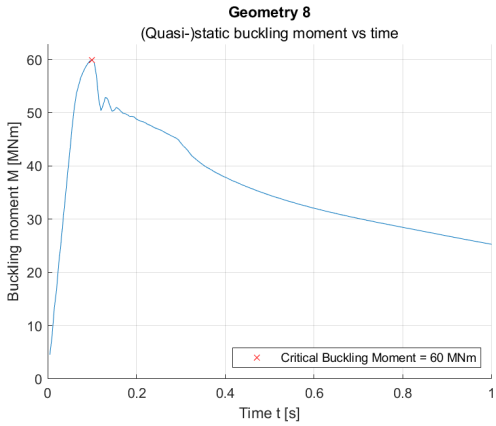

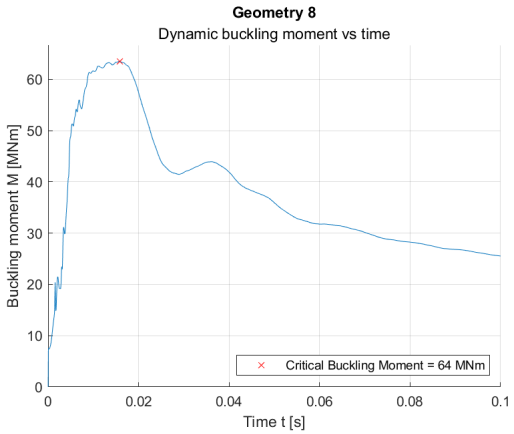

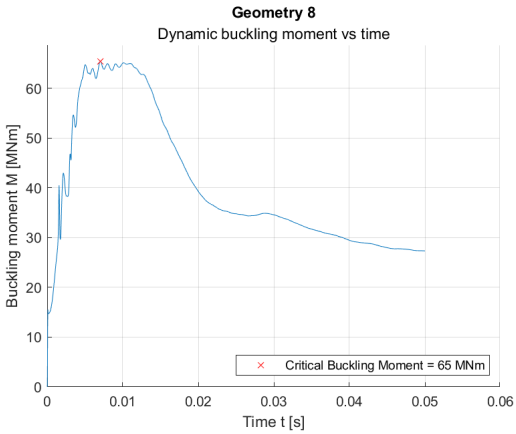

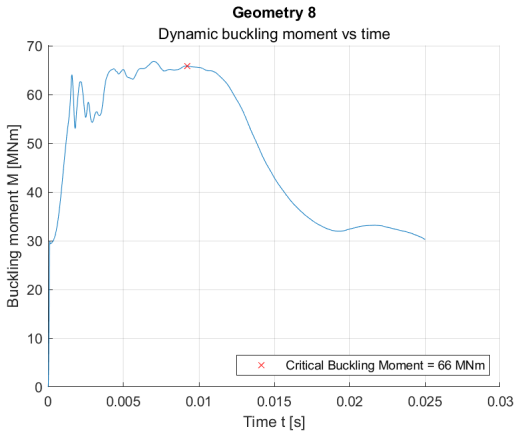

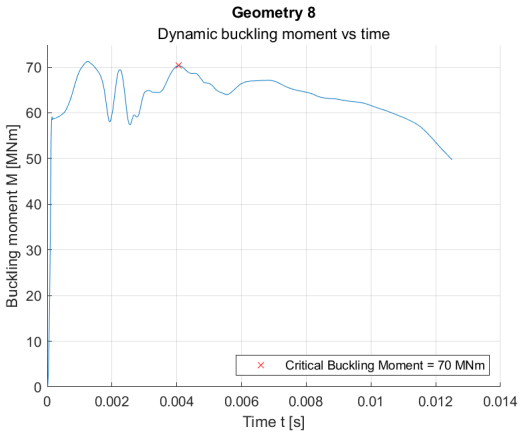

A.2.9. Geometry 9

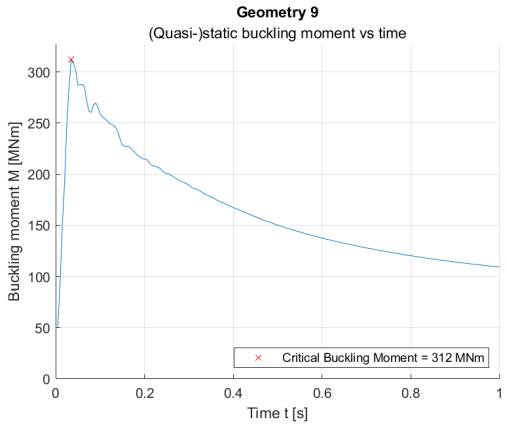

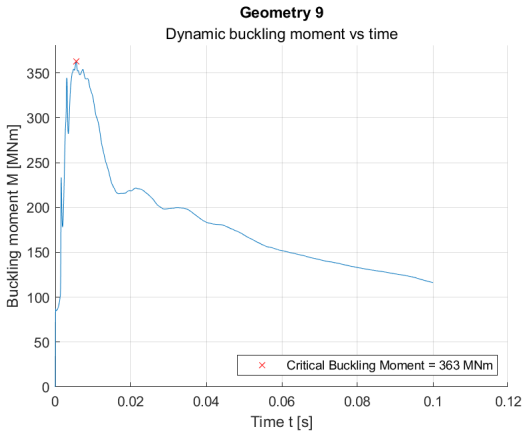

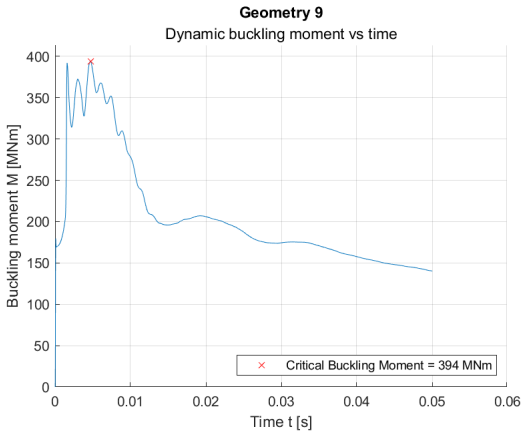

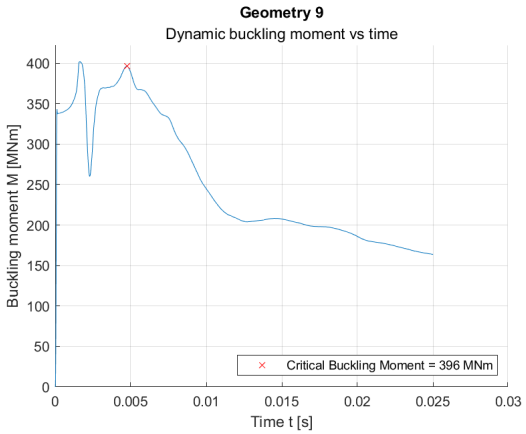

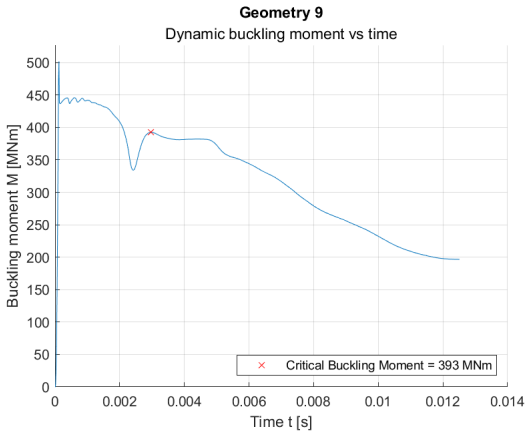

A.2.10. Geometry 10

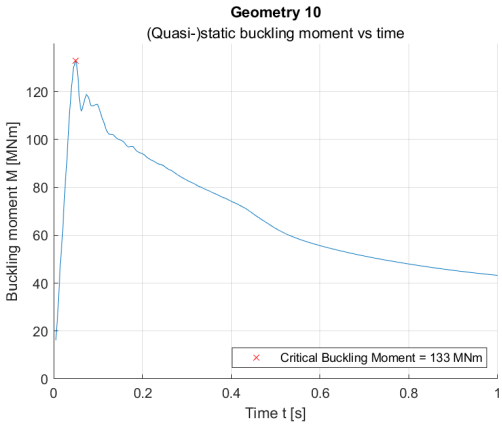

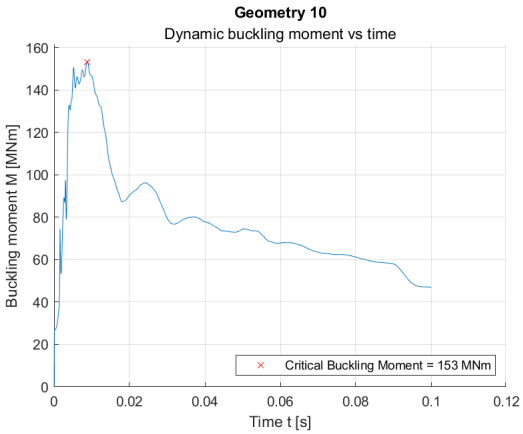

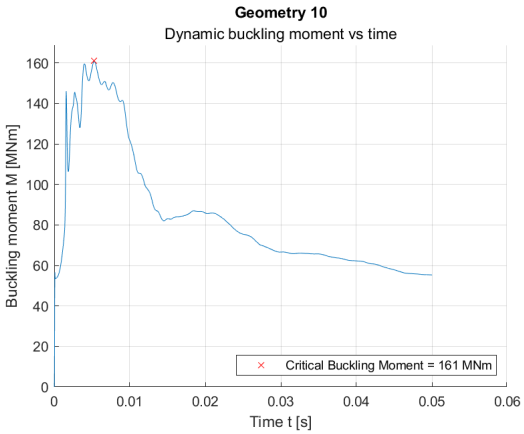

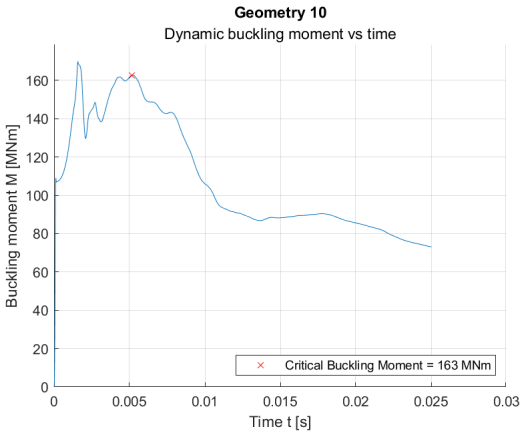

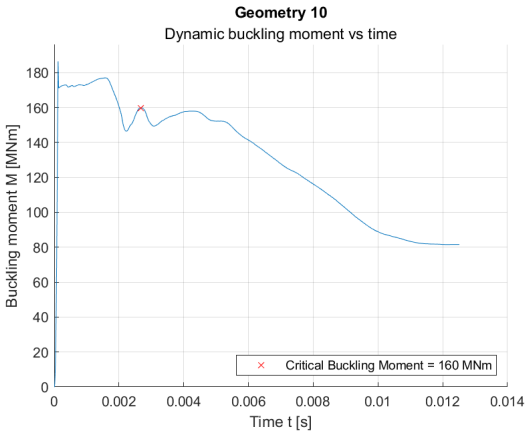

A.2.11. Geometry 11

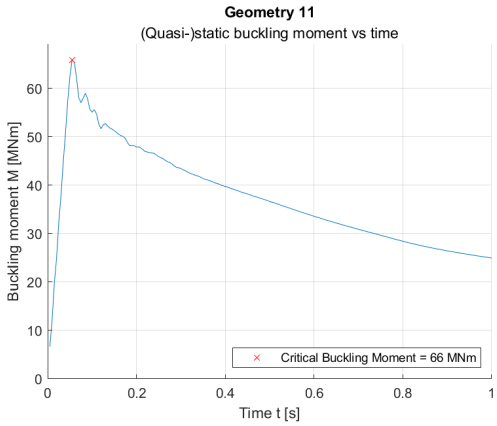

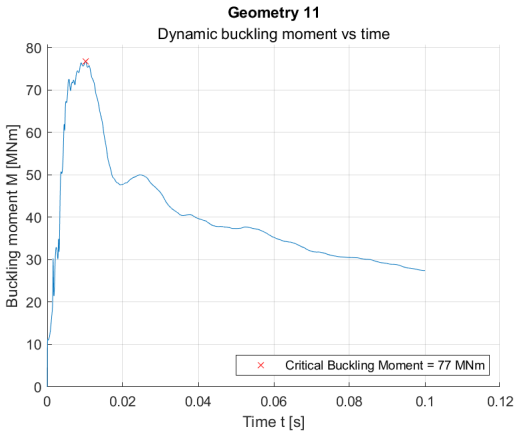

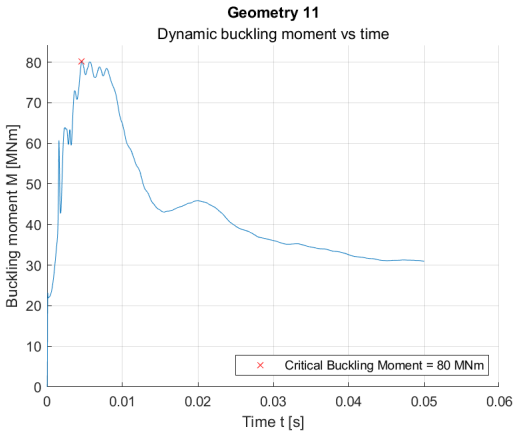

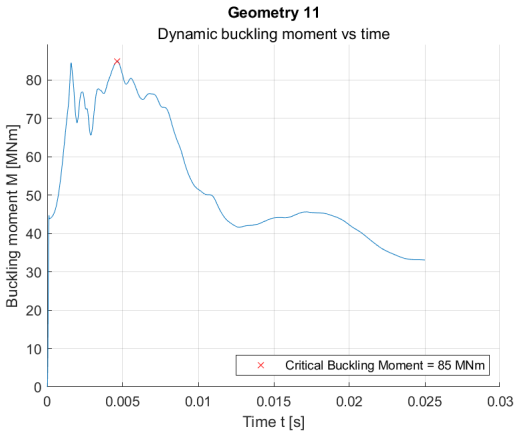

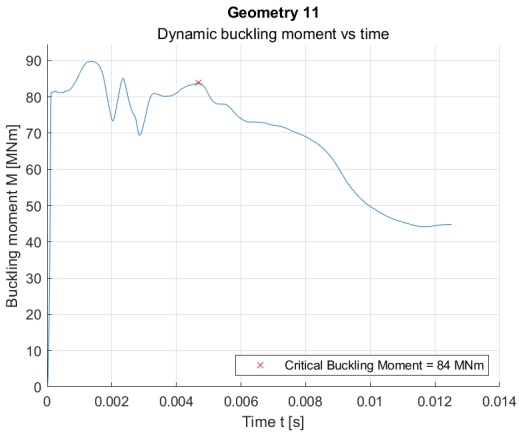

A.2.12. Geometry 12

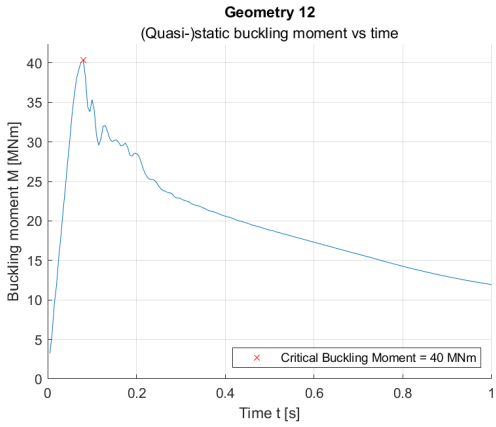

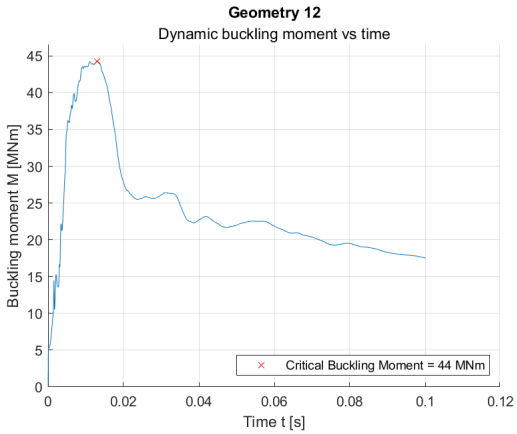

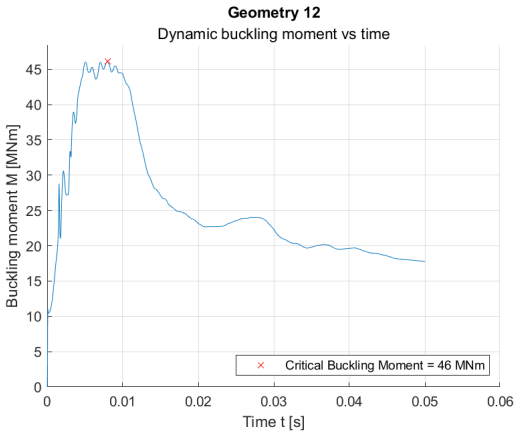

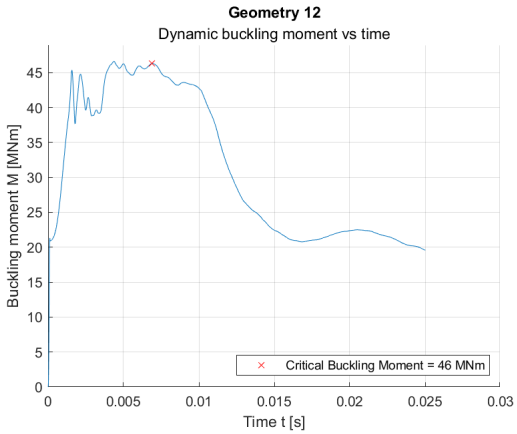

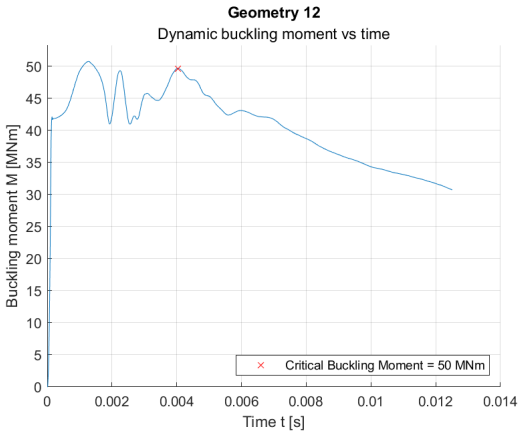

A.2.13. Geometry 13

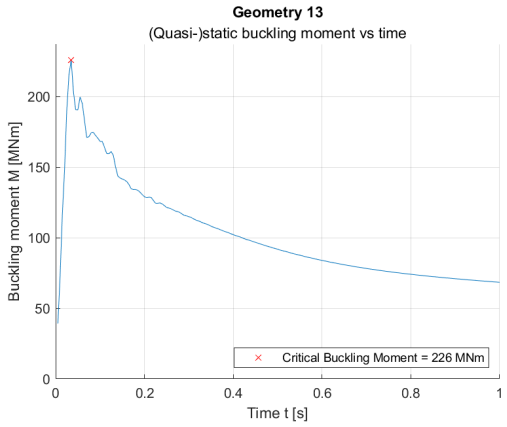

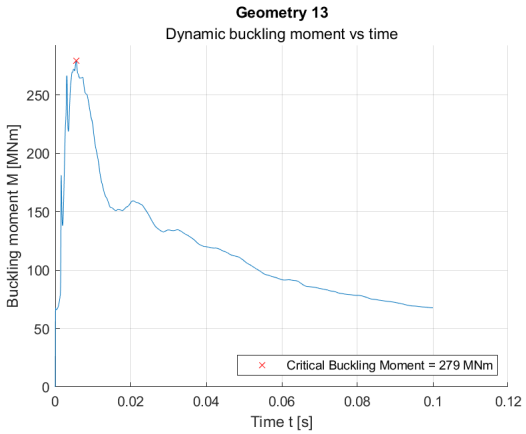

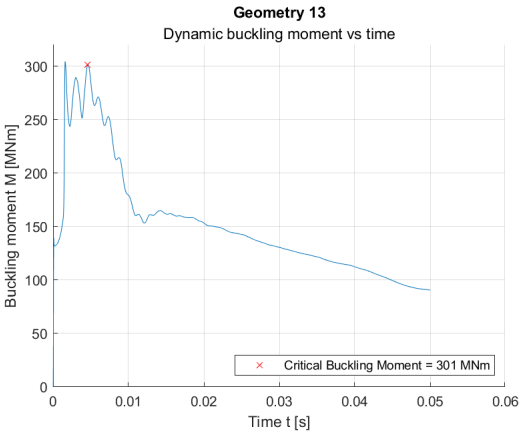

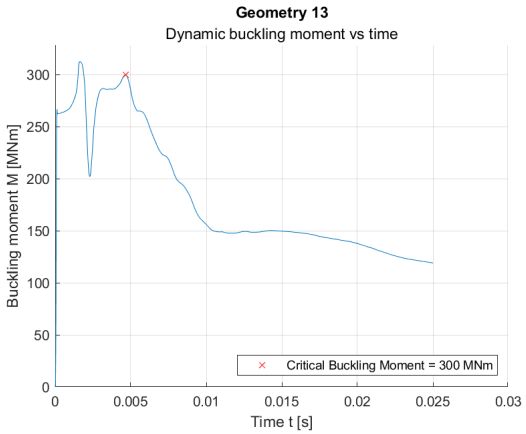

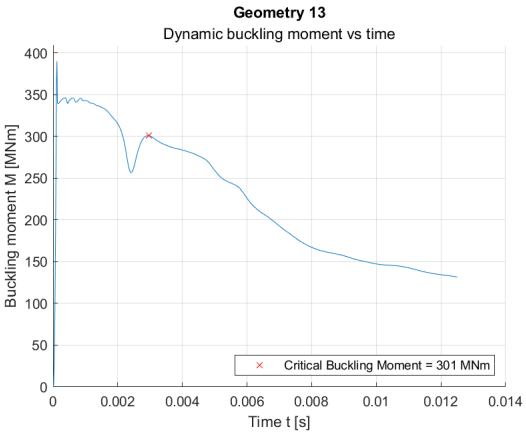

A.2.14. Geometry 14

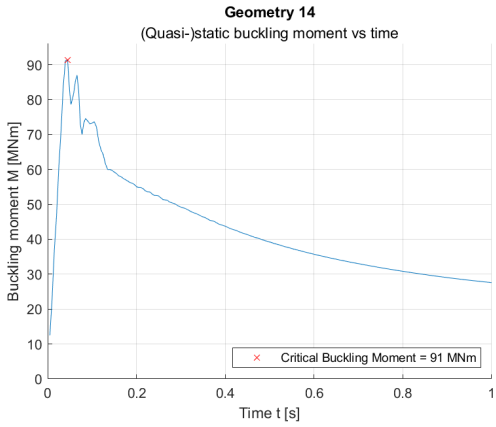

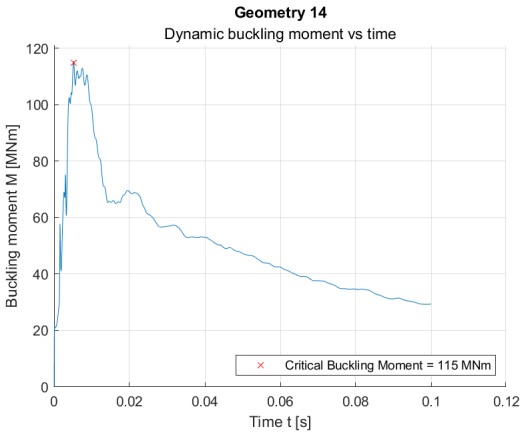

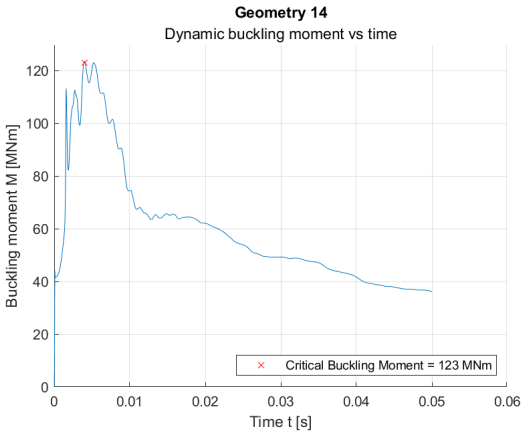

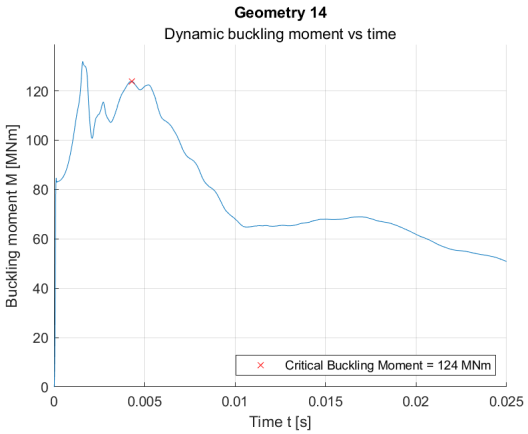

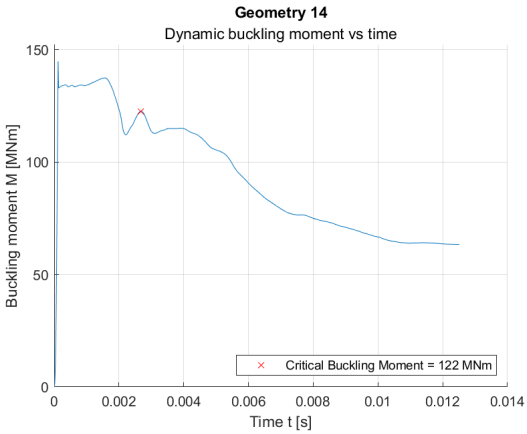

A.2.15. Geometry 15

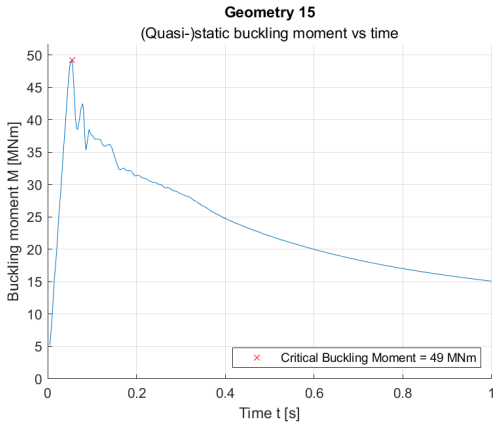

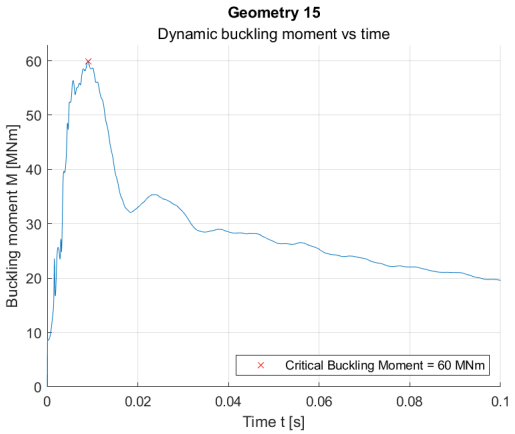

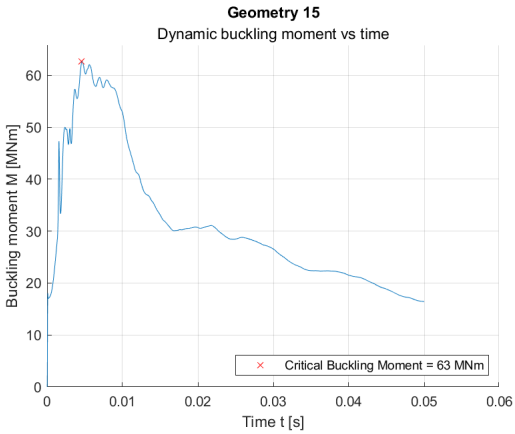

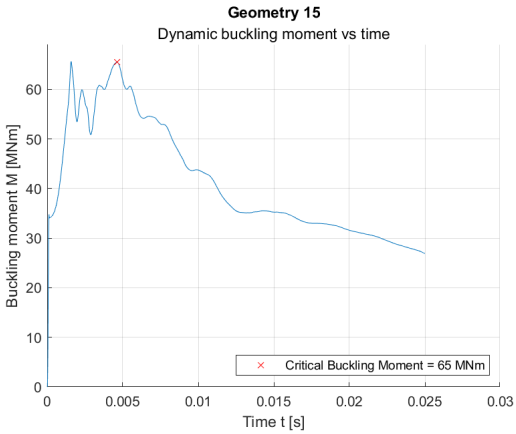

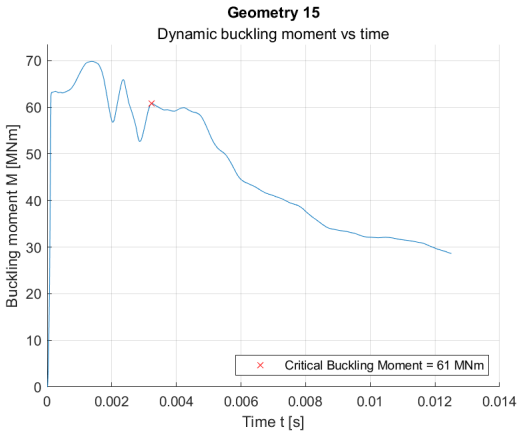

A.2.16. Geometry 16